Structure and Dynamics in Disordered Systems - Porous Flow and Fracture Propagation

Ken Tore Tallakstad

© Ken Tore Tallakstad, 2010

Series of dissertations submitted to the
Faculty of Mathematics and Natural Sciences, University of Oslo
No. 1014

ISSN 1501-7710

Acknowledgements

> *"Man skal tåle fedmekritikk og artigheter på ens egen bekostning. Der er kun en selv som er skyld i hvorledes man ser ut."*
>
> *- Andreas Lie, TSR guidelines*

Oslo, August 2010
Ken Tore Tallakstad

Preface

This thesis concludes the research undertaken by the present author as a PhD student at the group for Advanced Materials and Complex Systems, Department of Physics, University of Oslo, during the last three years (September 2007 – August 2010).

The work has been divided between two fields of research. The first part deals with experiments on simultaneous fluid flow in porous media. In short, we simultaneously inject a high viscous and a non viscous fluid at the same time into a porous model. This study was first initiated in 2006 by a series of experiments performed by the present author [1]. However at that time, no clear interpretation of the results could be obtained. Flexibility in the present PhD project have permitted us to follow up this study with supplementing experiments, data analysis, and finally a satisfactory understanding of the results.

The concept of simultaneous two-phase flow has existed for some time, and is commonly used in the petroleum industry to measure relative permeabilities, e.g the Penn-state method [2]. However, non-transparent core samples are normally used, and it is generally not possible to address the dynamics of the complex structures inside. This particular flow scenario is representative for some of the processes taking place in the bulk of an oil reservoir. Thus, in addition to scientific interest, increased knowledge could also be important for the oil industry. The first to do a pore-scale study of simultaneous two-phase flow, was Payatakes (1995) *et al.* [3, 4], categorizing the different flow patterns according to variation of the flow parameters. In our experiments we seek to answer how pressure and fluid flow relate to the structure observed during simultaneous two phase flow in a large transparent quasi two-dimensional model, consisting of $\sim 10^5$ pores. In particular we address how statistical properties such as cluster size distributions and morphology relates to the measured pressure and imposed flow-rates.

The second part of the present study considers experiments on fracture propagation in heterogeneous materials. Specifically, we observe a crack front propagating in a low-toughness plane between two weakly sintered Plexiglas

plates. Despite the obvious differences, the two topics have many similarities. Both systems are disordered in the form of local pinning centers of fluctuating strength, and a wide distribution of pore voids in the heterogeneous material and the porous medium respectively. This quenched disorder affects the dynamics in a similar manner, and particularly the existence of long range correlations. In fracture this is seen in the the elastic stress field ahead of the crack front, and in porous flow through the velocity field of the viscous fluid. In both systems, scale invariant fluctuating behaviour is the main characteristic of the dynamics. Such intermittency is best described through a statistical approach. To this end we found that many of the analysis methods developed for the flow experiments could be applied to the fracture experiments with only minor adaptive changes.

In fracture experiments it is in general hard to directly observe the dynamics during propagation, simply because most materails are non-transparent. For this purpose, Schmittbuhl and Måløy [5] introduced a transparent Plexiglas model to follow an in-plane Mode I fracture, allowing for direct visual observation. Further, the high velocity avalanche dynamics of the crack front were studied using this model [6]. Creep relaxation of the fracture, with a duration of several days, was later observed and has in part motivated the present study. Considering both forced and creep relaxation of the fracture, we have in the present work studied how toughness fluctuations influence the dynamics in high and low velocity regimes.

This thesis is organized as follows: *Part I - Introduction* and *Part II - Papers*. Part II contains the papers in which our experimental results are presented and discussed in detail. Part I aims to put these papers in a proper context, with an introduction to the underlaying research fields. Herein, Chapter I comprises the subject of porous flow, relevant for Paper I and II, whereas in-plane fracture is the subject of Chapter II relevant for Paper III.

List of papers

Paper I: Ken Tore Tallakstad, Henning Arendt Knudsen, Thomas Ramstad, Grunde Løvoll, Knut Jørgen Måløy, Renaud Toussaint, and Eirik Grude Flekkøy:
Steady-State Two-Phase Flow in Porous Media: Statistics and Transport Properties,
Phys. Rev. Lett. **102**, 074502 (2009)

Paper II: Ken Tore Tallakstad, Grunde Løvoll, Henning Arendt Knudsen, Thomas Ramstad, Eirik Grude Flekkøy, and Knut Jørgen Måløy:
Steady-state, simultaneous two-phase flow in porous media: An experimental study,
Phys. Rev. E **80**, 036308 (2009)

Paper III: Ken Tore Tallakstad, Renaud Toussaint, Stephane Santucci, Jean Schmittbuhl, and Knut Jørgen Måløy:
Local Dynamics of a Randomly Pinned Crack Front during Creep and Forced Propagation: An Experimental Study,
Submitted to Phys. Rev. E

Contents

Part I

Introduction

Chapter 1

Two-phase flow in porous media

This chapter is meant as a brief introduction to multi-phase flow in porous media, with main focus on steady-state flow as it encompasses a major part of the present work. Sections 1.1-1.3 should be readable for students working in other fields of physics, whereas parts of Sec. 1.4 may require some prior knowledge of porous flow physics. Section 1.4 gives an overview of the experimental setup, the procedure used in order to analyse images, and a brief description of simultaneous two-phase flow as background for Paper I and II.

1.1   Introduction

Porous flow shows interesting applications not only in physics, but includes also petroleum engineering, applied mathematics, hydrology, soil sciences, and biomedical and agricultural engineering. This very rich and broad field has puzzled and intrigued scientists for more than a century, and is still a hot topic of research. This is mainly due to the complex dynamics and structures observed, resulting from the interplay between one or more phases and a disordered porous medium [7, 8, 9]. Moreover in areas such as the petroleum industry, the chemical industry, food production, and agriculture, there are potentially huge economical benefits to be gained from increased knowledge in this field.

Ever since Henry Darcy introduced his famous equation [2] in 1856, much valuable insight on flow in porous media has been gained. This includes among other things the introduction of global flow equations [8], a good theoretical pore scale understanding of basic flow structures and their dependence on the flow parameters [10], and also various simulation techniques

based on pure statistical algorithms [11, 12], network modeling of capillary flow in tubes [13], lattice Boltzmann modeling [14] and so on.

However, many questions still remain unanswered. From an industrial point of view, the perhaps most important one being the upscaling problem [15]. It is often highly non trivial how the behavior observed at microscopic scale manifests itself on the laboratory scale. Even more so, how the physical description obtained at laboratory scale can be used to obtain a physical understanding at an even larger industrial scale. Additionally, new flow structures are discovered as more complex boundary conditions are introduced in experiments and simulations, motivated by new industrial applications and also pure scientific interest. Examples are; seismic stimulation of oil reservoirs to enhance oil recovery [16, 17], and the topic of the present work: simultaneous porous flow of two phases.

The volume of literature in this field is overwhelming, and to place the present study in a full context of all available literature is challenging. Below is given a general introduction of the basic parameters used to describe flow in porous media, followed by a more specific and selective inclusion of the most relevant background material, motivating the present work. Together with the references provided along the way, it should at least serve as a starting point for the eager reader.

1.2   Basic concepts and parameters

We will throughout this chapter restrict the discussion to two-dimensional porous media, for simplicity and illustrative purposes. Additionally the experiments carried out in the present work concerns so called quasi two-dimensional systems, as defined in Sec. 1.4.1. However the concepts introduced below apply also to the three-dimensional case.

1.2.1   Porous media and fluid properties

A porous medium is in general any solid containing voids. Of special interest are permeable porous media, i.e. the existence an interconnected path of voids throughout the bulk of the solid, enabling one or more fluids to flow from one end to the other. The voids are referred to as *pores*, and the random pore network constitutes what is called the *pore space*. Examples of porous media are: sandstone, limestone, cement, sponge and so on. A characteristic property of a porous medium is the *porosity* ϕ_0, defined as:

$$\phi_0 = \frac{V_p}{V}, \quad \text{where} \quad \phi \in [0, 1] , \tag{1.1}$$

and V is the total sample volume whereas V_p is the pore space volume.

The *permeability* κ_0 is another geometrical property, describing a fluids ability to flow through the porous medium. The permeability is fluid independent and analog to the conductance in electrical circuits. A high value makes it easier to flow and vice versa. A commonly used unit of permeability is *darcy*, after Henry Darcy, where 1 darcy $= 9.87 \cdot 10^{-9}$ cm$^2 \simeq 1(\mu$m$)^2$. When dealing with multi-phase flow, i.e. more than one fluid or phase present in the porous medium, κ_0 is referred to as the *absolute* - or *one-phase permeability*. The permeability can be measured through Darcy's law as discussed in Sec. 1.2.2.

Both the porosity and the permeability are average global quantities, and they do not give any information of the local properties of the porous medium. One such property is the quenched disorder of the pores. Quenched disorder means irregularities "frozen" into the system independent of time. Generally the pores have various sizes, which in turn has important implications for fluid flow. Figure 1.1 shows a two-dimensional model porous medium consisting of randomly placed discs confined by a rectangular box. It is customary to divide the pore space into pores and pore throats. The region confined by d_1, d_2, and d_3 constitutes a *pore*, whereas the narrower channels characterized by the lengths d_1, d_2 and d_3 are referred to as *pore-throats.* In real porous media it is not always a clear cut case to define pores and pore throats. Assuming however that it is possible to measure the different pores and pore throats, in terms of either volume or some suitable length scale, their distributions will provide valuable information on the system disorder. The disc diameter may be used as a length scale of the disorder in the present example. As will become apparent in Sec. 1.2.2 the morphological randomness in the porous medium will in turn transfer to the local pressures in fluid flow, and in this way play an important role for the dynamics.

Having introduced the embedding geometry in which different flow processes can take place, it is also necessary to describe the most important fluid properties. The *dynamic* viscosity μ is given by

$$\mu = \rho \nu \ , \tag{1.2}$$

where ρ is the fluid mass density and ν the *kinematic* viscosity. The viscosity can be interpreted as the ability of a fluid to sustain shear stresses, or more loosely speaking the resistance to flow.

When two immiscible phases (fluid-fluid or gas-fluid) are present in a porous medium, there will be a so called *surface tension* over the interfaces between the two phases due to molecular interactions. In the bulk of each phase there are cohesive forces between identical molecules, whereas weaker
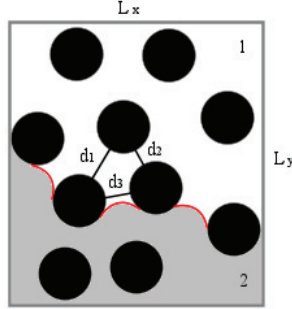
Figure 1.1: Porous medium consisting of discs with system size is $L_x \times L_y$. Two fluids are present, denoted 1 and 2, separated at the invasion front consisting of the three menisci (red). A pore is the region confined by the nearest neighbour distances d_1, d_2 and d_3. These individual lengths also give a characteristic size measure of the pore throats connected to the pore.

adhesive forces exist between different molecules on the interface between the two phases. A fundamental principle of any physical system is to reduce the free energy while maximizing the entropy. Adhesive forces contribute less to reducing the potential energy, thus it is favorable to minimize the interface area between the two phases and maximize the bulk volume. Due to the minimizing of adhesive forces, surface tension gives rise to curvature on the interface. As an example, the surface of a droplet of fluid in a gas is spherical, since this gives the largest volume pr. surface ratio and thus the lowest free energy configuration.

In equilibrium, surface tension is defined as the work needed to increase the surface area by one unit and can be viewed as a force pr. unit length or an energy pr. unit area. The mechanical equilibrium condition due to surface tension and the pressure difference over the curved interface can be formulated as [8]

$$\Delta p = \gamma \left(\frac{1}{R_1} + \frac{1}{R_2} \right) \ . \tag{1.3}$$

Equation (1.3) is the Young-Laplace law, where Δp is the pressure difference, γ is the surface tension, and R_1 and R_2 are the principal radii of curvature of the interface.

In addition to the interactions across the fluid-fluid interface, there are also molecular interactions at the contact line between the two phases and

the porous medium. This introduces yet another fluid property, namely the wettability. The wetting conditions of a fluid describe its ability to maintain contact with a solid. This is specified by the *contact angle* θ_w as shown in Fig. 1.2. It is measured as the inside angle between the tangential crossing at some contact point between the solid and the fluid in question. A fluid with contact angle $\theta_w < 90°$ is said to be *wetting* and for $\theta_w > 90°$ the fluid is *non-wetting*. For $\theta_w \approx 90°$, the fluid-fluid-solid system is said to have mixed wetting conditions. If we return to the example in Fig. 1.1, surface tension results in a curved interface between the two phases as seen in the three menisci and fluid 1 wets the porous medium.

Figure 1.2: Two droplets of different fluids are deposited on a solid surface, surrounded by a gas. The left droplet has a contact angle $\theta_w > 90°$ and is non-wetting, whereas the droplet to the right has a contact angle $\theta_w < 90°$ and is wetting the solid surface.

A more intricate situation arises when fluids are in motion. So called contact angle hysteresis [8] can occur, meaning that one measures a different contact angle upon advancing and receding fluid displacement. However in most cases, it is customary when local wetting are not of primary interest to give only the static wetting properties of the phases.

Having introduced the wettability of fluids, we define two more properties, namely the *viscosity ratio* and the fluid *saturation*, as they are important for fluid displacement in porous media. The viscosity ratio M is given as

$$M = \frac{\mu_{nw}}{\mu_w} \ , \tag{1.4}$$

where μ_{nw} and μ_w are the dynamic viscosities of the non-wetting and wetting fluids respectively. The non-wetting S_{nw} and wetting S_w saturations are the volume fractions of each fluid, and are defined as

$$S_{nw} = \frac{V_{nw}}{V_p} \ , \tag{1.5}$$

$$S_w = \frac{V_w}{V_p} \ , \tag{1.6}$$

$$S_{nw} + S_w = 1 \ , \tag{1.7}$$

where $V_p = \phi V$ is the pore space volume, V_{nw} and V_w are the volumes of the non-wetting and wetting fluids respectively.

1.2.2   Flow dynamics

Considering two immiscible phases displacing each other in a porous medium, their flows are governed by the equation of continuity and the Navier-Stokes equations [18]. However, due to the complex geometry of the porous medium, these equations can in general not be solved analytically. Quantitative descriptions are instead obtained by a combination of simplified effective equations, valid on large scale, and considerations of the flow at the scale of a single pore.

In 1856 Henry Darcy found an empirical relation between the fluid velocity and pressure gradient during one-phase flow through porous media. This was later known as the Darcy equation:

$$\mathbf{u}_D = -\frac{\kappa_0}{\mu} \left(\nabla p - \mathbf{F} \right), \tag{1.8}$$

where the volume flux $u_D = Q/A$ is called the *filtration-* or *Darcy*-velocity, Q is the volumetric flow-rate through the porous medium, and has units of $[m^3/s]$. The cross section of the porous medium orthogonal to the flow is denoted A, κ_0 is the permeability, μ is the viscosity, ∇p is the global pressure gradient, and $\mathbf{F} = \rho \mathbf{g}$ is some body force, e.g gravity. Note that the actual fluid velocity through the porous medium is $u = u_D/\phi$.

The Darcy equation has been generalized for multi-phase flow, although the applicability in this case is limited. The generalized Darcy equations assume that the flow of both phases is hydrodynamically independent, i.e. the flow of the wetting phase is uncoupled with that of the non-wetting. The non-wetting fluid appears as a "solid" to the wetting fluid and vice versa, and so called relative permeabilities are introduced to describe the resistance to flow for both phases. Since the relative permeabilities depend on parameters of both phases, it is no longer a pure geometrical property. For a thorough discussion of the generalized Darcy law, see [8, 2, 19].

While Darcy's law describes the average properties of the flow on a large scale, it is also necessary to consider local behavior at the pore scale. The *capillary* pressure over a fixed[1] meniscus is defined as

$$p_{\text{cap}} = p_{nw} - p_w \ , \tag{1.9}$$

---

[1]A viscous stress term must be included in the general case of a moving meniscus.

where p_{nw} and p_w is the non-wetting and wetting fluid pressure respectively. The capillary pressure thus gives the pressure difference over the non-wetting/wetting fluid interface. When neglecting gravity forces, the condition for mechanical equilibrium is given by the Young-Laplace equation [Eq. (1.3)], i.e. the capillary pressure is proportional to the curvature of the interface.

Returning once more to the example of fluid displacement in the model porous medium in Fig. 1.1, we can define two flow situations. When a non-wetting fluid (1) displaces a wetting fluid (2) the process is referred to as *drainage*. The opposite situation is called *imbibition*, i.e. when a wetting fluid displaces a non-wetting fluid. In a drainage situation, to move a meniscus into a narrower part of a pore-throat, one can either increase the non-wetting pressure or decrease the wetting pressure in Eq. (1.9). In equilibrium it then follows from Eq. (1.3) that the increase in capillary pressure must be accompanied by an increase in curvature. In this manner, the curvature of the interface is linked to its position in the pore-throat. A threshold or critical value of the capillary pressure p_c^d is associated with the narrowest part of the pore throat. Whenever p_{cap} exceeds p_c^d the meniscus becomes unstable, because the geometry of the pore-throat can no longer uphold mechanical equilibrium at this point. The instability causes spontaneous invasion of the pore in front. This is the mechanism of drainage at the pore scale, and it is important to note that the geometrical disorder in the porous medium (distribution of pore throats) is reflected in the capillary pressure. Reflected in the sense that each pore throat has a limit or critical value of the capillary pressure it can sustain. In the case of imbibition it is the widest part of a pore, associated with the lowest capillary pressure, that is of importance for advancement of the fluid interface. The wetting fluid will stand in the pore throats and invade the pore in front when the capillary pressure is below the critical capillary pressure for imbibition p_c^i.

The distributions of capillary pressure thresholds for drainage and imbibition play a significant role when considering two phase flow in porous media. This will be discussed further in Secs. 1.3 and 1.4.

The introduction to physics of flow in porous media in the present and previous subsection has been brief and somewhat superficial. The interested reader should look to the references [8, 9, 2, 18, 19, 20] for more comprehensive treatments of the topics presented.

1.2.3   Dimensionless numbers

Due to the complexity of flow in porous media, a vast number of displacement structures are observed. Some forces may dominate in the system, and are thus responsible for the structure observed. The most important are grav-

itational, capillary, and viscous forces. It is common practice to introduce
dimensionless numbers describing the ratio between these forces, as they can
be helpful in describing the dynamics as well as assist in the comparison
between different systems, e.g experiment and simulation.

For non-horizontal flow, gravity is important. The dimensionless ratio
between gravitational and capillary pressure over a characteristic pore is
called the *Bond*-number,

$$\text{Bo} = \frac{\Delta p_{\text{grav}}}{\Delta p_{\text{cap}}} = \frac{\Delta \rho g a^2}{\gamma} \ . \tag{1.10}$$

Here, $\Delta p_{\text{grav}} = \Delta \rho g a$ is the gravitational or hydrostatic pressure drop over a
pore of characteristic size a, $\Delta \rho = \rho_w - \rho_{nw}$ is the density difference between
the wetting and non-wetting fluid respectively and g is the component of
gravity in the direction of flow. The capillary pressure drop over a typical
pore-throat is approximated by $\Delta p_{\text{cap}} \approx \frac{\gamma}{a}$, and so Eq. (1.10) follows. Small
values of the Bond number means that capillary forces dominate over the
gravitational ones. Notice that when $\mathbf{g}$ is perpendicular to the flow, as in
two-dimensional horizontal models, Bo = 0.

If we look at the ratio of viscous to capillary forces, being the most im-
portant for the present work, we get the *Capillary*-number Ca. It is defined
here as:

$$\text{Ca} = \frac{\Delta p_{\text{visc}}}{\Delta p_{\text{cap}}} = \frac{\mu_w Q_w a^2}{\gamma \kappa_0 A} \ . \tag{1.11}$$

The viscous pressure drop follows from Darcy's law over a pore of size a;
$\Delta p_{\text{visc}} = \mu_w Q_w a / \kappa_0 A$, where Q_w is the flow-rate of the wetting fluid. It was
emphasized previously that Darcy's law was a macroscopic equation, however
it is used here as a rough approximation. Viscous forces dominate the flow
when $\text{Ca} \sim 1$, whereas capillary forces dominates when $\text{Ca} \ll 1$.

The definition of the capillary number often differs in the literature, even
though it always gives some measure of the viscous to capillary force ratio.
Thus care must be taken when comparing results for given Ca-numbers from
different studies. It is generally not sufficient with only the numerical value,
and it should always be made clear how the capillary number is defined.
Fortunately in this work the definition of the Ca-number is not crucial, as
it is merely a useful dimensionless number proportional to the important
tuning parameter Q_w, i.e. the flow-rate of wetting fluid.

1.3   Transient flow regimes

After having introduced the necessary concepts of flow in porous media in the previous section, an overview of the "classical" structures observed during either drainage or imbibition will be given in the following. Pore geometry, boundary conditions, and controlling parameters (M, Bo, and Ca) will govern the displacement. It is important to have some notion of the underlying physics of these processes.

Transient flow regimes mean that some of the flow parameters and the displacement structure are time dependent. Furthermore the duration of the process is between the onset of invasion and breakthrough, i.e. when the invading phase reaches the system perimeter, percolating[2] the porous medium.

1.3.1   Capillary fingering

Consider a drainage situation where Ca $\ll$ 1, i.e. the capillary forces completely dominate viscous forces. This means a very slow invasion rate of the non-wetting phase. The pressure inside each phase is everywhere the same and the pressure difference over the non-wetting-wetting fluid interface is given by the capillary pressure, Eq. (1.9). In a porous medium initially saturated with wetting fluid, the front (interface between the two fluids) is located along a line at the inlet, trying to overcome the capillary barriers presented by the pore-throats. When the flow is initiated, either p_w or p_{nw} will increase so that p_{cap} also increases. This is a stable situation as long as the capillary barriers can sustain the gradual increase in p_{cap}. The widest pore throat along the front will have the smallest capillary threshold, p_c^d. Whenever $p_{\text{cap}} > p_c^d$, the front becomes unstable and invades the pore in front of the widest pore-throat. The spontaneous invasion of pores are referred to as bursts and is one type of so called Haines jumps [21, 22], occurring over a much smaller time scale than the advancement of the front in the pore-throats. The number of pores invaded in a burst depends on the capillary pressure, because the front will not stabilize until it finds a new configuration in which all capillary thresholds are greater than the current capillary pressure. After a burst, equilibrium is obtained and p_{cap} must be increased once more to continue invasion. In this manner, the wetting fluid is displaced from the porous medium, until the non-wetting fluid percolates the model. Figure 1.3 a) and b) show for experiment and simulation respectively, the resultant structure from a displacement in the capillary fingering

---

[2]The existence of a connecting path from one end to the other.

regime at breakthrough. It is characterized by wetting clusters of all sizes
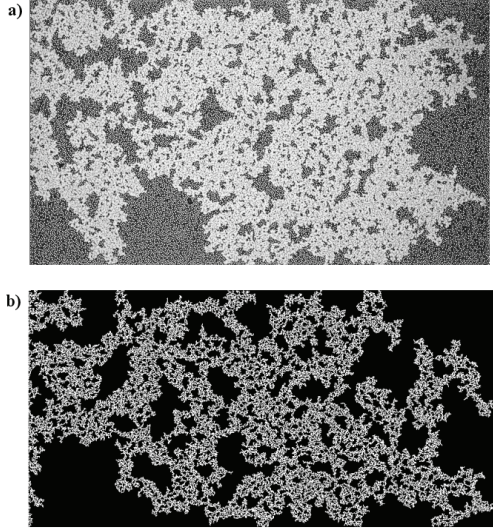
Figure 1.3: **a)** Air (white) displacing a water/glycerol mixture (black) in a porous cell consisting of a monolayer of glass beads randomly distributed between two plates [M. Jankov, Complex group, UiO, (2006)]. System size 10×20 cm, consisting of ~ 44100 pores, and Ca $\sim 10^{-4}$. **b)** IP-simulation [1] with trapping in a 400×800 lattice. The similarity between a) and b) is evident.

surrounded by an interconnecting network of non-wetting fluid, referred to as the percolating cluster.

Måløy *et al.* [23, 24] studied how the capillary pressure varied under slow drainage experiments. It was found that a sudden drop in capillary pressure accompanied every burst. They also observed that the volume of displaced defending fluid during a burst, did not leave the model, but was redistributed over the front making the menisci retract. This capacitive volume effect was found to be the reason for the sudden pressure drops.

The displacement structure in the capillary regime will depend on the wettability. The description above assumes favorable wetting conditions. That is, a contact angle of the invading fluid around $180°$. Robbins *et al.* [25, 26, 27], studied how ordinary capillary fingering structures changed with the wetting properties of the system. They found that below a critical

contact angle, dependent on the porosity, the invasion structure flooded the system. When the contact angle approaches the mixed wetting limit, the distribution of capillary thresholds will be drastically altered. Due to the wetting, equilibrium menisci can exist also outside of the pore-throat exit. This means that neighboring menisci can intersect and coalesce, thus altering the dynamics.

1.3.2   Viscous fingering

The viscous fingering regime characterizes a drainage process where a low-viscous fluid displaces a high-viscous fluid at a large flow rate. In this case the viscosity ratio $M \ll 1$, and Ca ~ 1. This regime, seen from experiment and simulation in Fig. 1.4 a) and b) respectively, is characterized by finger formation of the invading fluid, propagating faster through the medium than the rest of the front. The finger development causes the front to be unstable.

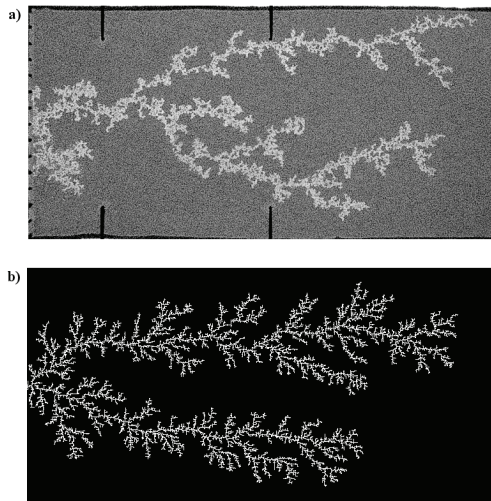Figure 1.4: **a)** Viscous fingering experiment in a porous cell consisting of a monolayer of glass beads randomly distributed between two plates, performed in the Complex lab (2007). Air displaces glycerol from a single inlet node at a high flow-rate from left to right. System size of $40 \times 80 \, \text{cm}$ containing ~ 213600 pores, $M \sim 10^{-4}$ and Ca $= 0.16$. **b)** DLA-simulation [1] on a 400×800 lattice.

In the initial stages of the displacement, some part of the front will get ahead of the rest. Due to the low-viscosity in the invading fluid, the pressure drop in the invading phase is negligible. It then follows from Darcy's law [Eq. (1.8)], that the parts of the front closest to the system outlet, will experience the highest pressure gradients in the high-viscous defending fluid. This means that the tips of the fingers will propagate at a higher velocity through the porous medium than the rest of the front. In linear models, one or two fingers usually dominate the growth. By dominate, we mean that the growth of these fingers suppress the growth of smaller fingers further behind. This screening effect has been studied by Løvoll *et al.* [28].

Viscous fingering was first studied by Saffmann & Taylor (1958) in Hele-Shaw cells[3] [29]. They found that if an initial flat fluid/fluid interface was perturbed above a critical wavelength, viscous fingers would develop. This is known as the Saffmann-Taylor instability.

1.3.3   Stable displacement

When a high-viscous fluid displaces a low-viscous fluid, opposite to that of viscous fingering, at a high flow-rate so that $Ca \sim 1$ and $M \ll 1$, the flow regime is referred to as stable displacement. The displacement front is in this case almost flat. A small roughness is observed due to the disorder of the porous medium. Since the front is flat, there are little trapping of defending fluid. Only small trapped clusters are observed for lower flow-rates, and the maximum cluster size is bound by the roughness of the front. The reason for stabilization in this case, is that advanced parts of the front will experience lower pressure gradients than parts further behind. Thus the pores closest to the inlet of the system will always be considered for invasion before any of the advanced pores. Figure 1.5 shows a cropped section from a stable displacement experiment.

Capillary fingering, viscous fingering, and stable displacement have been studied extensively over the years. The phase diagram of Lenormand *et al.* (1988) [10] sums up these regimes.

1.3.4   Other displacement structures

The previously considered displacement structures are all limiting cases of horizontal flow in terms of Ca and M. References to other studies are given below, exploring intermediate values of the parameter space, and also introducing new forces.

---

[3]So called quasi two dimensional flow model, consisting of two plates separated by a small distance compared to the dimensions of the plates.
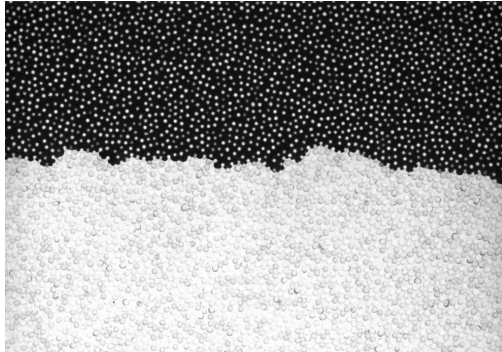
Figure 1.5: Stable displacement imbibition experiment in a porous Hele-Shaw cell [S. Santucci, Complex group, UiO (2006)]. A viscous water/glycerol mixture (black) displaces low-viscous air (white) at a flow-rate of $Q_{tot} \approx 69$ ml/min. The front is flat, without any trapping of air clusters. Size of cropped section: 85×59 mm.

When Bo $\neq 0$, gravity will either stabilize or destabilize the flow depending on the density difference between the phases and the directions of flow and gravity. Méheust *et al.* [30] studied the effect of tilting a porous Hele-Shaw cell out of the horizontal plane so as to consider the stabilizing effect of gravity during the displacement of a high-viscous, high-density fluid by a low-viscous, low-density fluid. For a constant capillary number, it was observed that the displacement changed from viscous fingering to capillary fingering to stable displacement like structures with increasing values of the bond number.

Viscosity matched experiments, i.e. $M = 1$, where performed by Frette *et al.* [31] for small Ca numbers. Stable displacement like structures with trapping of defending fluid clusters were observed. The roughness of the displacement front was shown to exhibit scale invariant behaviour with the capillary number.

The increasing interest in seismic stimulation during porous flow, has resulted in simulation studies by Aursjø *et al.* [16] where an oscillatory body force was introduced, and also experimental work by Jankov *et al.* [17] where either the invading phase or the porous medium itself was oscillated.

Finally it is worth mentioning the review article of Payatakes *et al.* [32] considering a number of different drainage and imbibition displacements.

1.4   Steady-state, simultaneous two-phase flow

This section is devoted to the simultaneous flow of two phases in a large model porous medium, shown in Fig. 1.6. Together with Paper I and II, it embodies one of two main parts of the work presented in this thesis.
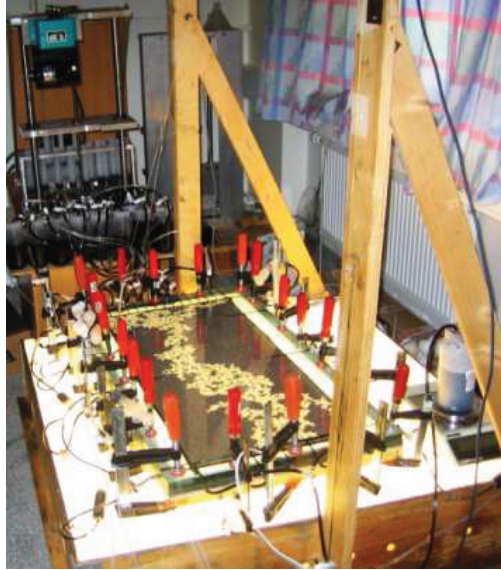
Figure 1.6: The experimental setup used for the flow experiments is depicted. The injection pump system is seen in the upper left corner, and the lightbox with the model on top is seen at the center.

1.4.1   Experimental setup

The experimental setup used in Papers I and II is shown in Figs. 1.7 and 1.8. We use a mono-layered porous medium consisting of glass beads of diameter a=1 mm, randomly spread between two contact papers [28, 31]. This is one realization of the porous Hele-Shaw cell, a so called quasi two dimensional system. The model is a transparent rectangular box of dimensions $L \times W$=850 $\times$ 420 mm^2 and thickness a. A detailed listing of the model parameters can be found in Table I in Paper II.
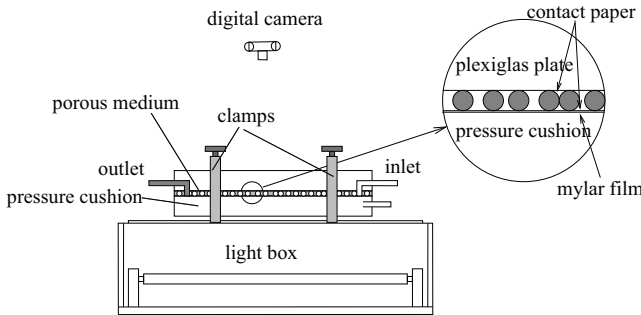
Figure 1.7: Sketch of the experimental setup with the light box, the porous model and the digital camera. The porous medium is sandwiched between two contact papers and kept together and temperature controlled with a water filled "pressure cushion".

A 2 cm thick Plexiglas plate is placed on top of the model. In order to squeeze the beads and the contact paper together with the upper plate, a Mylar membrane mounted on a 2.5 cm thick Plexiglas plate, below the model, is kept under water pressure as a "pressure cushion". The upper plate and the lower plate are kept together by clamps, and the side boundaries are sealed by a rectangular silicon rubber packing. The upper plate has 15 independent drilled inlets for fluid injection and a milled outlet channel (Fig. 1.8). The distance between the inlets and the outlet channel defines the length of the model.

Due to the small separation of the plates, our model is considered to be a quasi two-dimensional medium. Network models etched in glass [3, 4] are other examples of model porous media. The advantage of quasi two-dimensional models is that the flow can easily be visualized, and one is able to make measurements directly on the observed structures. However, the generalization of results obtained for two dimensional flow to three dimensions are in general not trivial.

The wetting fluid used in all our experiments is a *glycerol-water* solution dyed with Negrosine (black color), whereas *air* is used as the nonwetting fluid. This gives a black & white fluid pair with good visual contrast. The viscous ratio is $M=\mu_{nw}/\mu_w \sim 10^{-4}$, which is typical for a gas/liquid system. Other fluid parameters are found in Table I in Paper II. The model is kept at a constant temperature of 20°C during the experiments. This is monitored by measuring the temperature in the wetting fluid at the outlet, thus allowing
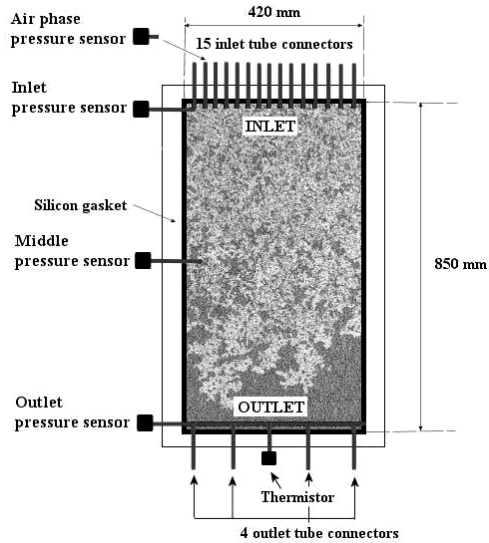
Figure 1.8: Sketch of the experimental model. There are 15 independent inlet holes with attached tubes where we inject (alternately) the wetting and the nonwetting phase with syringe pumps. This leads to a mixing of the two phases inside the model porous medium (a random mono-layer of glass beads), and a mix of the two phases flows out of the outlet channel at the opposite end of the system. In one of the inlet tubes (nonwetting phase) and in the porous model (wetting phase), pressure sensors are mounted for pressure measurements.

accurate estimation of the viscosity of the fluid.

During experiments the pressure is recorded at four different positions. In one of the air inlet tubes and in the wetting fluid at three positions: close to the inlet, at a distance $L/2$ in the flow direction, and in the outlet channel (Fig. 1.8).

The flow structure is visualized by illuminating the model from below with a light box, and images are captured at regular intervals with a digital camera. Each image contains 3000×2208 pixels, corresponding to a spatial resolution of ~ 0.19 mm per pixel (27 pixels in a pore of size 1 mm^2). Close to the inlet and to some degree along the model perimeter, there are boundary effects in the displacement structure. To avoid these, we define a (69×30)cm region of interest in the central part of the model used for image analysis.

In all experiments the porous model is initially filled with the wetting glycerol-water solution. An experiment is then started by injecting the wetting fluid and the nonwetting fluid from *every other* inlet hole (Fig. 1.8). Counting from one side this means that syringes no.: 1, 3, 5, ..., 15 inject the wetting fluid. Similarly, syringes no.: 2, 4, 6, ..., 14 are used for the nonwetting fluid. The movement of all 15 syringes are controlled by the same step motor, setting an equal displacement rate.

1.4.2   Image analysis

A substantial part of the results in Papers I and II are obtained from image analysis of the flow structure. In this subsection additional and complementary details to those provided in the papers will be given.

The raw image displays a wide range of gray levels with the darkest shadings corresponding to the water-glycerol mixture, and the lightest shadings corresponding to the air. The glass beads and possible film flow of water-glycerol appear as medium gray spots. The first task is to separate the phases from a gray scale of 256 levels into a binary representation by choosing a threshold level. The accuracy of any results obtained in this manner is highly dependent on how well the interfaces of the resulting black and white image trace the actual interfaces of the object imaged.

To obtain an optimal black and white image, the raw image itself must be of high quality. In this respect, homogeneous illumination of the flow structure is of vital importance. Uneven illumination is unfavorable due to intensity gradients, causing different regions of the image to be affected unevenly for a given threshold value. To this end, considerable effort has been made to ensure a homogeneous diffusive white illumination from the lightbox (depicted in Fig. 1.6).

In some cases when the object of interest has a very good contrast to
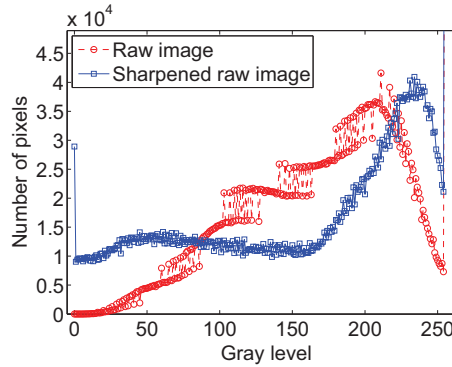
Figure 1.9: Gray level histogram of the imaged flow structure. Circular and square markers correspond to a raw image and a sharpened raw image respectively. Sharpening separates in particular the white air phase into a distinctive peak at a gray level of ~ 225.

the "background", and the background and object occupy roughly the same amount of space, the gray level histogram presents two distinctive separate peaks. The threshold value is then easily found at the local minimum between the two peaks. In our flow experiments however, it is hard to use this procedure to determine the threshold, due to the wide and mixed gray level distributions of fluid and air clusters seen in the raw image histogram in Fig. 1.9. The reason for this mixing is due to the flow structure. Thousands of small fragmented air clusters are embedded in a background flow field of fluid. A large number of clusters implies many interfaces between air and fluid, which again implies local gray level gradients in the images. The water-glycerol fluid also wets well the porous medium, and may give rise to film flow. Some air clusters are seen to appear darker than others, and might be due to a surrounding fluid film. The result is mixing of the two distributions, making the threshold challenging to find.

To further improve the quality of the raw images, i.e. isolate the gray level distribution corresponding to the white air phase, a sharpening algorithm is applied. It is somewhat technical to go into details of this algorithm, but it is a common tool in most image treatment software. Sharpening enhances the contrast and shifts "dark" and "bright" areas further towards lower and higher gray levels respectively, as shown in Fig. 1.10, thus reducing the problem with dark air clusters. Figure 1.9 shows how the sharpening algorithm affects the gray level distribution in a typical image of the flow structure.
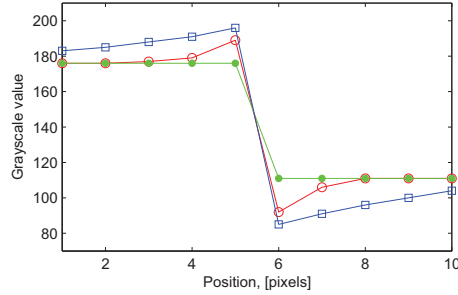
Figure 1.10: Application of a sharpening algorithm over an initial step-function of graylevels (filled circular marker). As more sharpening is applied (empty circular and square markers) the contrast between the two grayscale levels are enhanced.

When the raw image is sharpened, the gray level distribution presents two peaks corresponding to the white air-filled and dark gray glycerol-filled parts of the image. Particularly the white peak, seen to the right in Fig. 1.9, is very distinct. The image is then thresholded at a small constant offset from the white-peak to obtain a representative boundary between the two phases. This offset is found by careful visual inspection from raw images with extracted black and white interfaces superimposed. All further image treatment is performed on the resulting black and white image. A stepwise presentation of the image analysis is shown in Fig. 1.11.

In the black and white image, the glass beads are indistinguishable from the white air bubbles or clusters. This will not affect further analysis, provided one is at larger scales than the bead size (or pore size) a. Furthermore all connected regions of white pixels smaller than ~ 20 pixels are disregarded from analysis, as this roughly corresponds to the maximum size of a glass bead (see the inset of Fig. 13 in Paper II).

Finally the black and white image is analyzed with the image processing toolbox provided by MATLAB. This includes among other things the distributions of size and extent of air bubbles as explained in Papers I and II.

1.4.3   Flow structure

In this subsection a brief description of the flow pattern obtained by using the boundary conditions described in Sec. 1.4.1 will be given. The displacement structure in simultaneous two phase injection, is at all stages significantly

a)   b)

c)
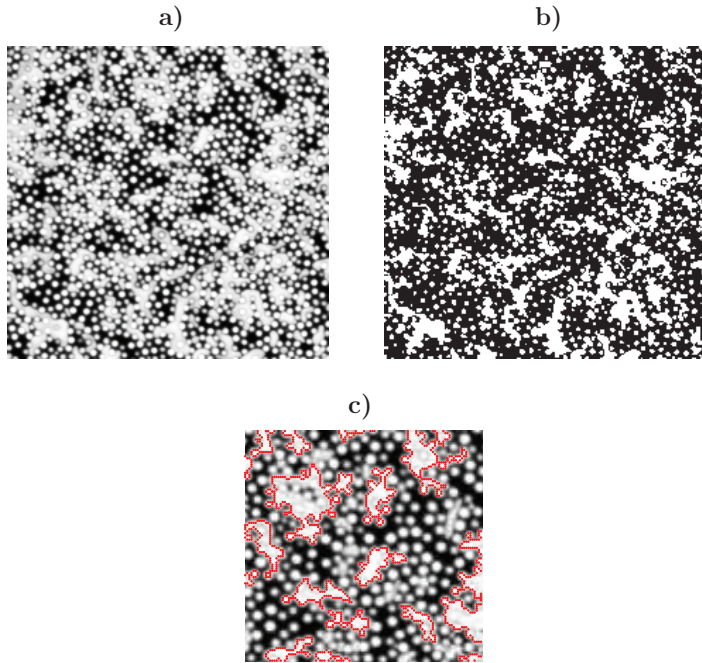
Figure 1.11: Three steps of the image analysis: **a)** Sharpened raw image of a small cropped section of the flow structure. **b)** Thresholded black and white image of the gray scale original in a). **c)** For illustrational purposes, only selected interfaces obtained from b) have been superimposed (in red) on a small section of the original raw image in a).

different from that of capillary- or viscous fingering. From a fractal continuous invasion cluster of nonwetting fluid, the presence of a background flow field of the wetting fluid, contributes to a high degree of fragmentation of the air phase. This is shown in figure 1.12. During the transient stage of invasion, the wetting fluid is displaced by numerous smaller invasion clusters of nonwetting fluid, along the front. After breakthrough, the average global saturation (of both phases) approaches a constant value, and the structure is characterized by a flow of fragmented air clusters, mixed in a background field of the water-glycerol fluid. As an air cluster moves through the porous medium, it can be deformed in many ways before it reaches the outlet. This may be by further fragmentation, merging with other clusters, trapping in the porous medium etc. What is referred to as *steady-state* is reached when both
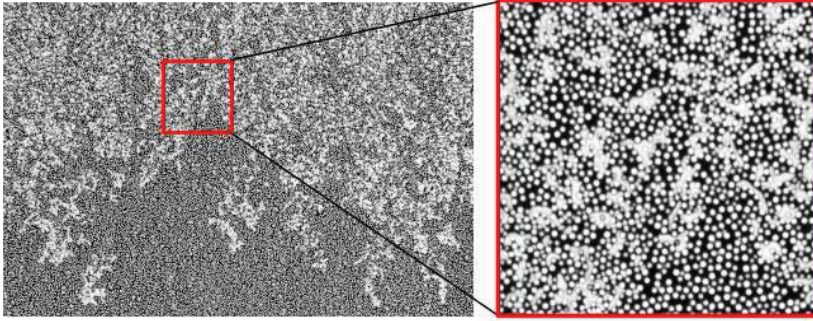
Figure 1.12: Snapshot of the invasion phase in one of our experiments, performed in the Complex lab (2007). Air (white) and water-glycerol (black) are injected simultaneously into a porous Hele-Shaw cell, initially saturated with the water-glycerol mixture. In the zoom-in we see the fragmented air-clusters.

phases are transported through the model without "long-time" flow parameter changes, implying that the pressure difference, relative permeabilities, saturations, and cluster distributions are on average constant.

In the experiments we tune the flowrate of both phases entering the model. A pronounced observable effect is the decrease in the typical size of clusters of fragmented air when the flowrate is increased. Also, the wetting fluid saturation increases with increasing values of the capillary number. This can be seen in Figs. 1.13 and 1.14, showing the different stages of invasion for two different capillary numbers.

The main structural difference between classical regimes described in Sec. 1.3 and simultaneous flow, is the existence of multiple independent invasion clusters, due to fragmentation. The simultaneous flow of the wetting and nonwetting phase, causes a competition between drainage and imbibition. When the air clusters extend a certain length into the model, *snap offs* will occur. By snap off we mean that imbibition displacement takes place somewhere behind the tip of a non-wetting cluster, and disconnects a part of it. We will see that snap offs introduce a characteristic length scale of the largest non-wetting clusters, thus being the origin of fragmentation. Both in Paper I and II we address how the dynamics of the flow is governed by this length scale, the global pressure difference over the model, and the system disorder.
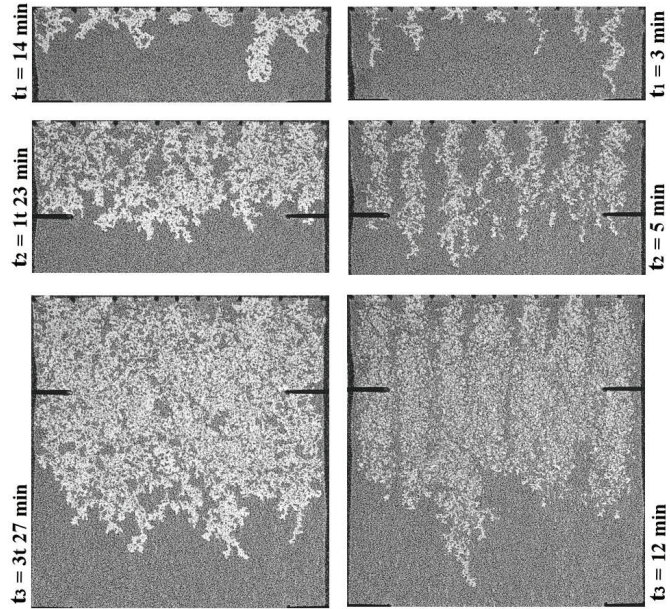
Figure 1.13: Time series (t_1, t_2 and t_3) of the invasion phase for a Ca = 0.0079 (left) and a Ca = 0.17 (right) experiment. In both cases the degree of fragmentation and mixing increases with time. The wetting fluid is displaced by several independent non-wetting clusters. In the right column, channel flow can be seen. This signature of the boundary conditions is gradually wiped out with time. In the left column virtually no signature effect is observed.
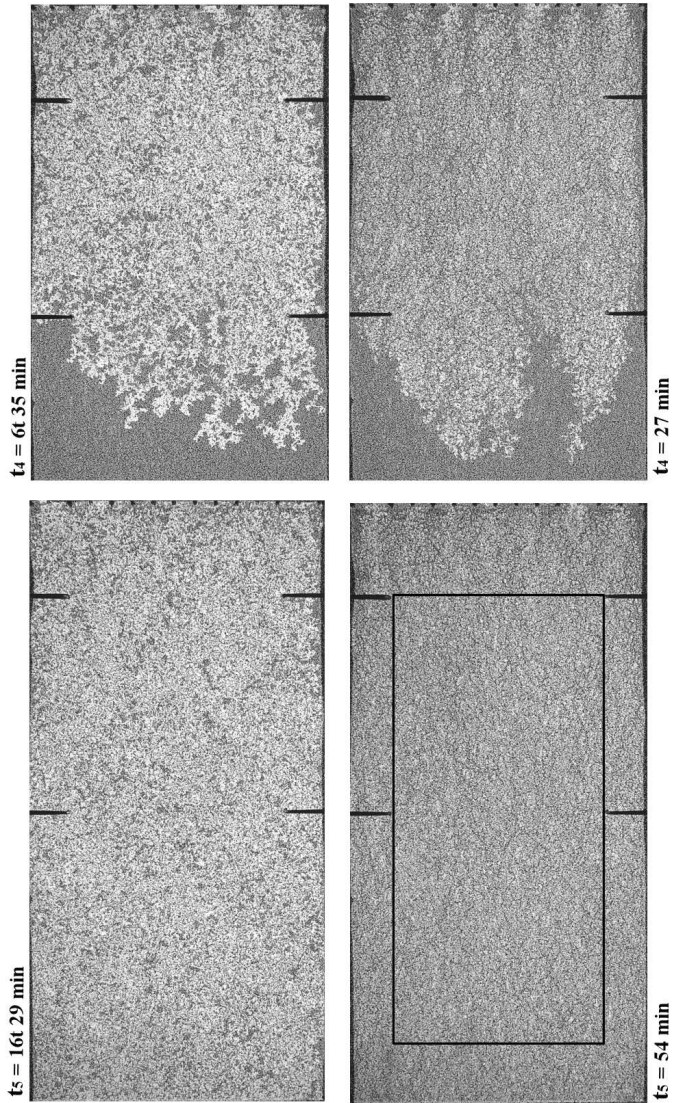
Figure 1.14: Continuation of Fig. 1.13. The timestep t_4 shows the middle stage of the invasion phase. At t_5 the systems are in steady-state. The whole porous matrix contains a homogeneous mix of the two phases. Note that much of the air invaded region in t_4 is similar to that of later steady-state. The region bound by the rectangle in the bottom right panel (ROI), shows the area considered during image analysis.

Chapter 2

In-plane fracture propagation

This chapter serves as a background to the second part of the thesis. Although being a different area of physics, fractures in heterogeneous materials share many similarities with flow in porous media. In particular the way quenched disorder in the system influences the dynamics. Sections 2.1-2.2 should be readable for those with a general physics background, whereas part of Secs. 2.3 and 2.4 will also involve some technicalities, relevant for the work presented in Paper III.

2.1 Introduction

The failure and fracturing of materials have obvious implications in everyday life and in the industry. It is known that Leonardo da Vinci measured the strength of iron wires, and found that their strength varied inversely with the wire length. Fracture is a complex process manifested on many scales; from the separation of atomic bonds, to the nucleation and growth of micro and macro voids, and even up to larger geological scales during earthquakes and fault dynamics.

The theory for describing fracture is relatively new, and to this date there is no single formalism that handles every aspect of the observed complexity. The foundation, however, for much of the obtained knowledge, and a cornerstone in modern fracture mechanics, is the pioneering work by A. A. Griffith published in 1920 [33]. Extended later by G. R. Irwin in 1956, introducing the energy release rate concept [34].

A main contribution to the description of fracture in heterogeneous media was provided by Rice *et. al* in 1985 [35], accounting for toughness fluctuations due to material irregularities. As improved experimental techniques have made it possible to map fracture surfaces with high resolution, the roughness

of cracks have been given much attention [36]. In particular, the universality concept of the morphological properties of fracture surfaces, proposed by E. Bouchaud *et. al* [37].

Material heterogeneities affect not only the morphology of fracture but also the dynamics. Similar behaviour is found in a variety of other systems, commonly referred to as crackling noise [38]. Måløy *et. al* [6] studied in 2006, high velocity avalanches of a fracture front propagating in a transparent Plexiglas model. The present work on fracture is an extension of [6], considering the dynamics during either forced or creep-relaxation of fracture in high and low velocity regimes.

2.2   Basic concepts from LEFM

In this section, a brief introduction to *linear elastic fracture mechanics* (LEFM) will be given. Knowledge of LEFM is important for any study of material failure. The theory concerns linear elastic homogeneous media, with a very small volume element of nonlinear and dissipative processes around the crack tip. This region is referred to as the *Fracture Process Zone*. The two terms *crack* and *fracture* will be used synonymously in the following.

2.2.1   The stress field in Mode I fracture

The fracture of solids can be categorized by three loading modes, or a combination of these. This is shown in Fig. 2.1. Mode I (opening mode) corresponds to a tensile loading normal to the plane of the fracture. Mode II (sliding mode) corresponds to in-plane shear loading perpendicular to the crack front, and tends to slide one crack face over the other. Mode III (tearing mode) corresponds to out ouf-of-plane shear loading, i.e. parallel to the plane of the crack and parallel to the crack front. In the present work only Mode I fracture will be considered. A fundamental question in fracture is how an applied outer stress is transmitted through the solid and in particular near the crack tip where fracture actually takes place. Inglis [40] considered in 1913 a highly illustrative model. Consider a uniformly stressed plate containing an elliptical cavity as shown in Fig. 2.2. The equation of the ellipse is given by

$$\frac{x^2}{c^2} + \frac{y^2}{b^2} = 1 \ . \tag{2.1}$$
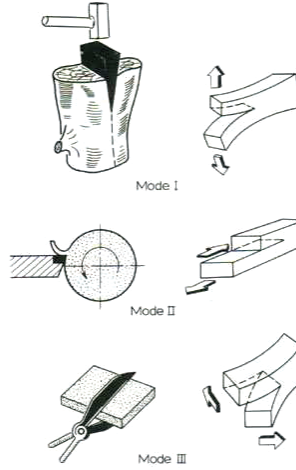
Figure 2.1: The three loading modes of fracture (from [39]). Mode I - opening, Mode II - sliding, and Mode III - tearing.

It may be shown that the radius of curvature r has a minimum value at the point C,

$$r = \frac{b^2}{c} , \quad \text{where} \quad b < c .$$ (2.2)

The analysis of Inglis relates stress at C to the applied stress σ_A:

$$\sigma_{yy}(c, 0) = \sigma_A \left(1 + 2\frac{c}{b}\right) ,$$ (2.3)

$$= \sigma_A \left(1 + 2\sqrt{\frac{c}{r}}\right) .$$ (2.4)

An interesting case with respect to fracture arises when $b \ll c$, in which Eq. (2.4) reduces to

$$\frac{\sigma_{yy}(c, 0)}{\sigma_A} \approx 2\sqrt{\frac{c}{r}} .$$ (2.5)

It is to be noted that the stress ratio in Eq. (2.5) depends on the surface geometry of the cavity rather than size or area, and can take values much larger than unity for a small radius of curvature. This means that a relatively
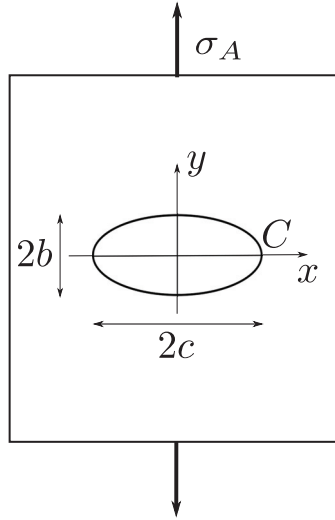
Figure 2.2: Uniform tensile loading of a plate containing an elliptical cavity. The applied stress is σ_A, the minor and major axis of the ellipse is given as b and c respectively, and the point C defines the notch tip of the ellipse.

small applied stress will cause a large stress consentration at the notch tip of a narrow cavity.

As an example consider the model in Fig. 2.2 "cut in half" along the $y-$axis, i.e. a surface cavity defined for $x > 0$ loaded in Mode I. It can be shown that the stress field component σ_{yy} will decrease asymptotically from its maximum value $\sigma_{yy}(c, 0)$ and approach σ_A for large x. Generally, the largest stress gradients are confined to a highly localised region of order r, surrounding the position of maximum stress concentration ($\sigma_{yy}(c, 0)$ at the point C in the present example).

A Mode I surface crack can in general be considered as a half-ellipse, infinitely narrow ($b \to 0$), with a finite crack length c and a small but finite curvature r at the tip. Approximating these boundary conditions by an infinitesimally narrow and perfectly sharp slit, as shown in Fig. 2.3, Irwin [41]

obtained the stress field solution[1]:

$$
\left\{
\begin{array}{c}
\sigma_{xx} \\
\sigma_{yy} \\
\sigma_{xy}
\end{array}
\right\}
=
\frac{K}{\sqrt{2\pi r'}}
\left\{
\begin{array}{c}
\cos(\theta/2)[1 - \sin(\theta/2)\sin(3\theta/2)] \\
\cos(\theta/2)[1 + \sin(\theta/2)\sin(3\theta/2)] \\
\sin(\theta/2)\cos(\theta/2)\cos(3\theta/2)
\end{array}
\right\} .
\qquad (2.6)
$$

Here r' and θ is the spherical coordinates of the stress field, and K is the so called *stress intensity factor*. The latter quantity depends on the crack length, applied stress, and sample geometry. As an example, for an edge crack under Mode I loading, $K = \sigma_A \sqrt{\pi c}$ and $K = 1.12 \sigma_A \sqrt{\pi c}$ for an infinite and a semi-infinite plate respectively. Equation (2.6) is only valid in close vicinity to the crack-tip, the so called *singularity dominated zone*. Further away from the crack tip, it should be mentioned that other non singular contributions to the stress field become important. These terms are however outside the scope of this introduction. The stress component σ_{yy} in Eq. (2.6) takes the same form as in Eq. (2.4). However, the Irwin solution diverges as $r' \to 0$, which is unphysical, since no material can sustain infinite stress. This has been of some concern since it is well known that at high stresses, plastic deformation may occur in metals and so called crazing[2] in polymers relaxes the stress field further. To this end, corrections from plasticity theory and nonlinear material behaviour have been proposed [42].
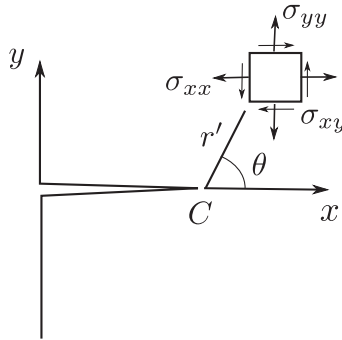
Figure 2.3: Irwin representation of a fracture, where C defines the sharp crack tip. For a small area of distance r' from C making an angle θ with the $x-$axis, the stresses are indicated.

---

[1]For illustrational purposes only the two dimensional solutions are given.
[2]Crazing is a network of fine micro cracks, preceding the main fracture.

2.2.2 The Griffith criterion for crack propagation

Around 1920 A. A. Griffith [33] developed a fracture theory based on energy considerations rather than local stress. Using a principle from thermodynamics he studied the energy balance of the system, and wanted to obtain the crack configuration that minimized the total free energy U_T of the system. Using the same notation as in [41] the free energy can be divided into two terms

$$U_T = U_M + U_S \ , \tag{2.7}$$

where $U_M = U_E + U_A$ is the mechanical energy, consisting of the stored elastic strain energy in the solid U_E, and the potential energy from the outer applied loading U_A. The term U_S is the surface energy, expressing the energy cost in creating new crack surfaces. Consider then a Mode I loading of the system in Fig. 2.3 with a crack length c, defined from the $y-$axis to the point C. For an imaginary extension of the crack dc, thermodynamic equilibrium is obtained by a balance between the mechanical and surface energy, expressible as

$$\frac{dU_T}{dc} = \frac{d}{dc}(U_S + U_M) = 0 \ . \tag{2.8}$$

The mechanical energy will decrease under crack extension due to the release of tractions across dc i.e. $dU_M/dc < 0$, whereas the surface energy will increase since cohesive molecular forces must be overcome in order to open new crack surface, i.e. $dU_S/dc > 0$. It is this balance that is expressed through Eq. (2.8).

It is common practice to define a quantity referred to as the *mechanical energy release rate*[3], given as

$$G = -\frac{dU_M}{dC} \ , \tag{2.9}$$

where C is now the crack area. In a straight crack, the crack length c is proportional to the crack area and we can write

$$G = -\frac{dU_M}{dc} = \frac{dU_S}{dc} = \Gamma \ , \tag{2.10}$$

where Γ denotes the surface energy per crack length, referred to as the *fracture energy*. When Eq. (2.10) is fullfilled, the crack is in equilibrium, but as soon as the energy release rate exceeds the fracture energy, the crack will

---

[3]Rate is in this context meant relative to extension of crack area or length, not time.

start to propagate. This is expressed through the famous Griffith criterion for fracture propagation

$$G \geq \Gamma \ . \tag{2.11}$$

In the case of quasi-static conditions, i.e. very slow propagation of the crack so that virtually no dissipation takes place at the crack tip, all the mechanical energy is used to drive the crack forward and create new crack surface. The velocity of the crack front is then proportional to the difference in mechanical and surface energy, given by [43]

$$\frac{1}{\mu}v = G - \Gamma \ , \tag{2.12}$$

where μ is an effective mobility of the crack front.

Finally it may be shown that the energy release rate can be expressed through the stress intensity factor

$$G = \frac{K^2}{E} \ , \tag{2.13}$$

where the denominator equals Young's elastic modulus E in plane stress loading. Note that Eq. (2.13) is the special case of Mode I fracture. Generally in mixed mode fracture the energy release rate is composed of three stress intensity terms, one for each mode [41]. Using Eqs. (2.13) and (2.10) the *fracture toughness* may be defined

$$\Gamma = \frac{K_c^2}{E} \quad \Rightarrow \quad K_c = \sqrt{E\Gamma} \ , \tag{2.14}$$

thus providing an alternate formulation of Griffith's criterion for crack propagation in terms of the stress intensity factor and the fracture toughness: $K \geq K_c$. The toughness is a constant material property for homogeneous media. In heterogeneous materials on the other hand, disorder will induce local toughness fluctuations.

2.2.3   Dynamical description of a crack tip

Using the framework presented in Secs. 2.2.1 and 2.2.2 it is possible to obtain an average equation of motion of a Mode I fracture, propagating in a plane of low toughness compared to the rest of the material. The analysis is indeed similar to the classical work by Obreimoff [44] (1930), studying the splitting strength of mica crystals.

The system is shown in Fig. 2.5, and it is assumed in this case that the loading is slow enough for quasi static conditions to apply. Furthermore it is assumed that the upper plate is completely fixed, and the lower plate is thin enough for simple beam bending theory to apply. For simplicity we consider an arbitrary cross section along the $y-$axis, i.e. a two dimensional version of the system. The crack length c is the horizontal distance from the end of the plate, where a point force F is applied, to the crack tip. The deflection or vertical separation between the two plates is in this case denoted δ.

From simple beam bending theory [45] the applied force may be related to the deflection and the vertical length of the bent plate (crack length) as

$$F = \frac{3EI\delta}{c^3} \ , \tag{2.15}$$

where I is the so called area moment of inertia, a property of a cross section of the lower plate in the $xz-$plane, depending only on plate geometry. This quantity can be viewed as the resistance of the plate to bending and deflection. The mechanical energy of the system consists of two terms; the negative work of the applied force F

$$dU_A = -Fd\delta \ , \tag{2.16}$$

and the strain energy U_E, given as

$$U_E = \frac{1}{2}F\delta = \frac{3EI\delta^2}{2c^3} \ , \tag{2.17}$$

by integration of the energy density in the deformed volume of the bent plate [41]. The change in strain energy for a deflection variation $d\delta$ and crack extension dc is

$$dU_E = \frac{\partial U_E}{\partial \delta}d\delta + \frac{\partial U_E}{\partial c}dc \tag{2.18}$$

$$dU_E = Fd\delta - \frac{3\delta F}{2c}dc \ . \tag{2.19}$$

Using the equilibrium condition of Eq. (2.8) and Eq. (2.10) we obtain

$$dU_T = dU_E + dU_A + dU_S = 0 \ , \tag{2.20}$$

$$Fd\delta - \frac{3\delta F}{2c}dc - Fd\delta + Gdc = 0 \ , \tag{2.21}$$

$$G = \frac{3\delta F}{2c} = \frac{9EI\delta^2}{2c^4} \ . \tag{2.22}$$

We now impose a time dependent linear loading, i.e. $\delta = V_a t$ where V_a is the constant velocity of the bar used to displace the lower plate. From the Griffith criterion [Eq. (2.11)] it is clear that the crack will remained fixed (c is constant) as long as $G \leq \Gamma$, and propagate whenever G tempts to exceed Γ, thus we obtain from Eq. (2.22)

$$c(t) = \left(\frac{9EIV_a^2}{2\Gamma} \right)^{1/4} t^{1/2} \; , \tag{2.23}$$

$$v(t) = \frac{dc}{dt} = \frac{1}{2} \left(\frac{9EIV_a^2}{2\Gamma} \right)^{1/4} t^{-1/2} \; . \tag{2.24}$$

Note that for a heterogeneous material, Eqs. (2.23) and (2.24) are applicable only on a global scale, giving the average[4] length and velocity of the crack in time.

2.3 Toughness fluctuations and roughness

LEFM has a common property with the macroscopic equations of flow in porous media, in the sense that it describes average behaviour of the dynamics when applied to heterogeneous materials. We turn now to describe the influence of toughness fluctuations on fracture, again analog to the influence fluctuations of capillary threshold pressures have on the displacement structures in porous media.

A crack propagating slowly in a purely homogeneous material will remain straight or smooth, and it is possible through LEFM theory to obtain the value of the stress intensity factor. In heterogeneous media on the other hand, local defects induce fluctuations in the toughness of the material. This will cause an initially straight crack to develop deformations, since the front is pinned with different strengths at different positions. This is referred to as *roughness* of the fracture front. Not only will toughness fluctuations cause roughness, but the stress field will be correlated along the crack tip, i.e. the stress intensity factor will be modified. In order to extend the LEFM theory to the case of heterogeneous materials, perturbation analysis have been used to account for disorder. First order corrections to fluctuations in the stress intensity factors were included by Rice *et al.* [35], and a second order term was proposed by Adda-Bedia *et al.* [46].

A particularly illustrative equation of motion can be obtained for fracture in a heterogeneous material considering the stress intensity factor solution by Rice, obtained for an infinite body. Remember that the stress intensity factor

---

[4]With respect to the $x-$direction in Fig. 2.5.

can also be expressed through the mechanical energy release rate [Eq. (2.13)]. In terms of the latter quantity, the first order perturbation solution [35, 47] is given as

$$G = G^0 \left(1 + \frac{1}{2\pi} \int_{-\infty}^{\infty} \frac{h(x',t) - h(x,t))}{(x'-x)^2} dx' \right) \; . \tag{2.25}$$

The position of the crack front at time t, now defined as $h(x,t)$ as shown in Fig. 2.6 in Sec. 2.4.1, is confined to the $xy-$plane. This is so called *in-plane* conditions. The parameter G^0 is a reference mechanical energy release rate that would result in the case of a straight crack front located at the same mean position $\langle h(x,t) \rangle_x$. The integral describes long range elastic interactions in the energy release rate, due to material heterogeneities. To model variation in the fracture energy, equivalent to local toughness fluctuations [Eq. (2.14)], we can write

$$\Gamma = \Gamma^0[1 + \eta(x, h(x,t))] \; , \tag{2.26}$$

where Γ^0 is the average fracture energy as in the case of a homogeneous material, and η is an uncorrelated random component with zero mean, often taken to be Gaussian. It is then straight forward to obtain the balance between the mechanical energy release rate and fracture energy by inserting Eqs. (2.25) and (2.26) into Eq. (2.12). The following equation of motion is obtained

$$\frac{1}{\mu}v = G^0 - \Gamma^0 + \frac{G^0}{2\pi} \int_{-\infty}^{\infty} \frac{h(x',t) - h(x,t))}{(x'-x)^2} dx' - \Gamma^0 \eta(x, h(x,t)) \; . \tag{2.27}$$

The terms on the right hand side of Eq. (2.27) represent the most important effects in heterogeneous fracture. For a straight crack front, or at scales large enough for the roughness to be disregarded, the crack velocity is simply given by the difference between the average value of the energy release rate and fracture energy (first two terms). For a rough crack front there is in addition the competition between long range elastic forces and the disorder term (last two terms). Equation (2.27) has been modeled extensively and shown to describe a variety of systems; including in-plane fracture in PMMA [48], wetting contact line motion on a disordered substrate [49], and interfaces in disordered magnets [50].

It should be emphasised that Eq. (2.27) is only one model proposed to describe disordered fracture propagation under certain conditions. Strictly speaking it is applicable only under quasi static conditions and zero temperature. At finite temperatures, thermally activated processes might cause

so called sub-critical propagation, meaning that even though the Griffith criterion [Eq. (2.11)] is not fullfilled, propagation can still take place [51, 52, 53].

Hopefully Eq. (2.27) convince the reader that toughness fluctuations cause both roughness and velocity fluctuations along the fracture front. Roughness will briefly be considered below, whereas the dynamics are the topic of Paper III and will be treated in the next section.

Consider the fracture front $h(x, t)$ in Fig. 2.6 in Sec. 2.4.1. One way of measuring the roughness [54] of such a profile is through the second moment of the height distribution

$$\Delta h(\Delta x) = \langle (h(x + \Delta x) - h(x))^2 \rangle_x^{1/2} \ , \tag{2.28}$$

where the average is taken over all possible origins x of the window of width Δx. Scale invariance of this function, i.e.

$$\Delta h(\Delta x) \sim \Delta x^H \ , \tag{2.29}$$

gives a Hurst [55] or *roughness exponent* H. Equation (2.29) corresponds to so called in-plane roughness. For three dimensional crack surfaces, one may also find an out-of-plane roughness exponent [56]. When a relation such as Eq. (2.29) can be found, the profile is said to display self-affine scaling properties. Typical values of the roughness exponent is between $0.4 \leq H \leq 0.8$.

Quite remarkably, many different materials share the same roughness exponent [57], and it has been proposed that the morphology of fracture is universal for some classes of materials, independent of loading conditions [37, 58].

2.4 Local dynamics of fracture propagation

This section concerns the experimental study of the fracture dynamics in a Plexiglas (PMMA) sample, shown in Fig. 2.4. Together with Paper III it covers the second part of the work presented in this thesis.

2.4.1 Experimental setup and loading conditions

The setup used in our fracture experiments is shown in Figs. 2.4 and 2.5. The fracture sample is made of two transparent PMMA plates: a thicker plate with dimensions $(30, 14, 1)$ cm and a thinner plate with dimensions $(30, 10, 0.4)$ cm for the length, width, and thickness respectively. The plates are then sandblasted on one side using glassbeads ranging between $50\,\mu$m and $300\,\mu$m in diameter. Sandblasting introduces random roughness on the originally "flat" surface. This causes light to be scattered in all directions from
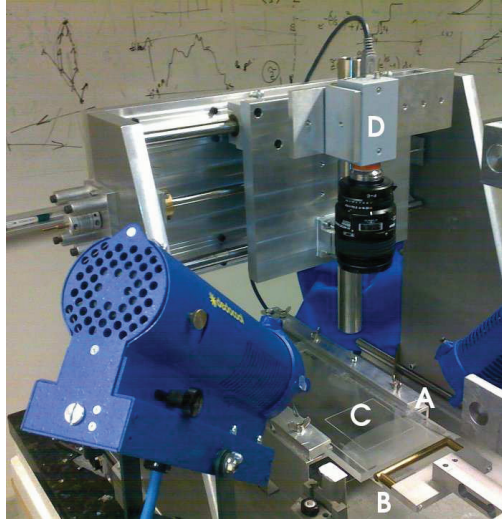
Figure 2.4: Picture of the experimental setup for studying fracture propagation in a PMMA block. A thick plate is clamped to an aluminum frame (A), while the thin plate is subjected to a load from the press bar, seen in the bottom right corner (B). The fracture front can be seen between the transparent and opaque part of the PMMA block (C), and is imaged from above with a digital camera (D).

these microstructures, and the plate is no longer transparent. The plates are clamped together in a pressure frame, with the sandblasted sides facing each other. The pressure frame is made of two parallel aluminum plates, exerting a normal homogeneous pressure on both sides of the PMMA. Finally, the pressure frame is put in a ceramic temperature controlled oven at $205\,^\circ$C for $30 - 50\,$min. This annealing or sintering procedure creates new polymer chains between the two plates and the resulting PMMA block is now fully transparent. The new layer created between the two plates is weaker than the bulk PMMA, so that we obtain a weak plane with quenched disorder in which the fracture can propagate. This system is ideal for direct visual observation since the fractured part of the sample immediately becomes opaque whereas the unfractured part remains transparent. The sharp and high contrast boundary between transparent and opaque parts defines the fracture front.

The thick plate of the PMMA block is mounted on a rigid aluminum
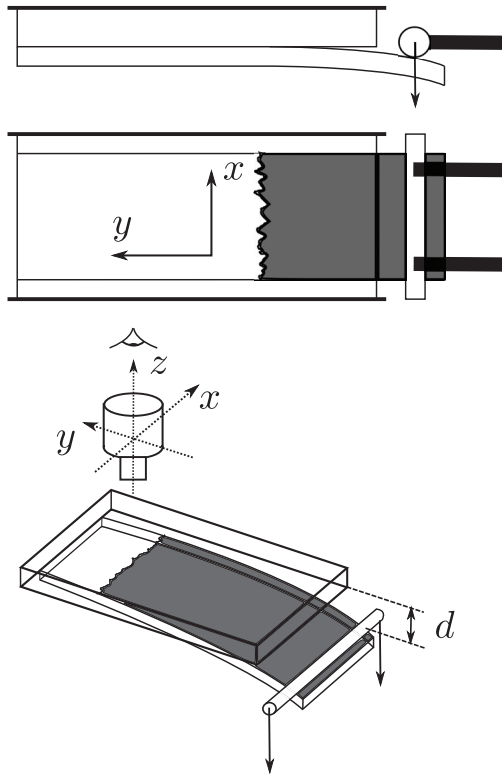
Figure 2.5: Sketch of the experimental setup. Two Plexiglas plates are sintered together, creating a weak in-plane layer for the fracture to propagate. Fracture is initiated by lowering a cylindrical press bar, controlled by a step motor, onto the lower plate, as seen in Fig. 2.4. The uncracked part of the sample is transparent, whereas the cracked part has lost transparency hence creating a good contrast at the fracture front. The fracture front is imaged from above by a digital camera. The deflection d (z-direction) between the plates is indicated in the lower panel. The fracture plane is (x, y), where the $x-$ and $y-$direction is transverse and parallel respectively, to the average direction of fracture propagation.

frame, also containing a camera setup for imaging. Mode-I fracture is induced by a normal displacement of the thin plate by a cylindrical pressbar, as shown in Fig. 2.4. Glycerol is put on the contact area between the plate and

the pressbar to reduce friction and prevent shear loading. The pressbar is mounted to a forcegage on a vertical translation stage controlled by a step motor, so that it can be moved up and down in the z-direction. Through the forcegage we are able to monitor the force exerted on the lower plate during an experiment.

In order to investigate how different loading conditions affect the local dynamics we apply the following loading to the PMMA sample: 1) forced crack propagation with an imposed constant deflection velocity of the press bar, and 2) creep relaxation with an imposed constant deflection of the press bar.

The front propagation is then followed in time, using a high speed digital camera, at the spatial resolution $\sim 2 - 5\,\mu$m/pixel. The obtained grayscale images contain two parts; a dark and a bright region, corresponding respectively to the uncracked and the cracked part of the sample. Contrary to the image analysis in Sec. 1.4.2, the gray level distribution of the raw image thus presents directly two distinctive peaks, and a stable threshold value is immediately obtained at the local minimum. The fracture front is then extracted from the black and white image in the same manner as interfaces were obtained in Sec. 1.4.2. For a more detailed description of the front extraction and image treatment see [59, 60]. Figure 2.6 shows the extracted fracture front superimposed on the raw image.
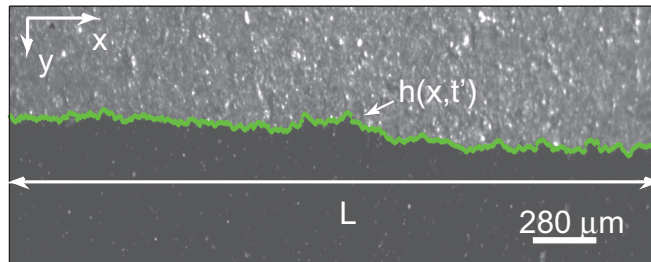

Figure 2.6: Fracture front line $h(x, t')$ at some time t', superimposed on the corresponding raw image. Direction of propagation is from top to bottom. System size L in the x-direction is indicated.

2.4.2   Avalanche dynamics

On a laboratory scale the fracture front can be viewed as a non-rough line propagating everywhere with the same velocity according to the loading conditions. Dynamically, disorder in the system results in pinning and avalanche like movement of the front. In some experiments this can be observed in realtime through the microscope. The front is seen in some parts to be almost completely pinned, or only moving slowly, and then suddenly jump to a new configuration. This can happen at multiple positions along the front at the same time. The areas covered in such jumps, seen both from observation and analysis, occur at very different sizes.

A big advantage of the setup is transparency. With a very high time resolution, the front shown in Fig. 2.6 is followed over a distance of roughly $\sim 500\,\mu$m. As described in Appendix A of Paper III, each image can be represented as a binary matrix, with unity entries at the position of the front and zeros elsewhere. All binary front matrices are then added to form the *waiting time matrix* (WTM). Each element of the WTM is then an integer, corresponding to the waiting time of the front at a particular position. The waiting time w is inversely proportional to the normal local velocity v of the fracture front

$$v = \frac{a_r}{dt\,w} \;, \tag{2.30}$$

where a_r and dt are the spatial and temporal image resolution respectively. A grayscale map of the waiting time matrix is shown for one of our experiments in Fig. 2.7. Dark regions correspond to a high waiting time and a low velocity, and vice versa for bright regions. The dark low velocity regions are seen to occur as irregularly shaped "lines" (pinning lines), separated by brighter compact regions referred to as high velocity avalanches. The wide span of waiting times shown by the colorbar, together with their irregular distribution in space, is direct visual confirmation of a complex dynamics. Furthermore this pinning/avalanche behaviour involves velocities on scales 1.5 and 2.5 decades below and above the average velocity of the fracture front respectively.

The statistical analysis of pinning lines and high velocity avalanches along the fracture front, is an important part of Paper III. The local velocity matrix $V(i,j)$, obtained through Eq. (2.30) for every element in the WTM, is a spatial map of the normal local velocities along the crack front. It is the basis for most of the analysis done in our fracture experiments. Avalanches are defined as connected regions or clusters in the thresholded binary velocity

$$L = 5.6 \text{ mm}$$
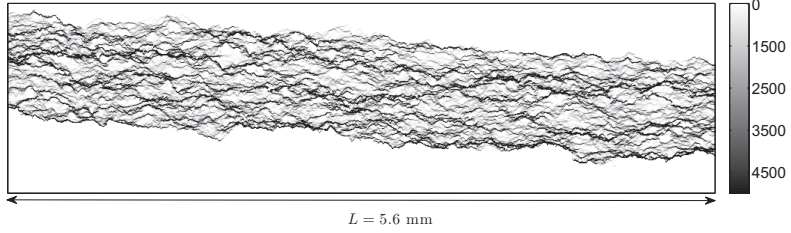
Figure 2.7: Waiting time matrix from one of our experiments. The average crack front velocity is $\langle v \rangle = 1.36 \, \mu\text{m/s}$. The map results from the extraction of $24\,576$ front lines at a rate of 50 fps. Dark regions correspond to a high waiting time and thus a low velocity, and vice versa for bright regions, as shown in the colorbar indicating the number of timesteps the front has been fixed at a given position. A unit timestep corresponds to $0.02 \, \text{s}$. Black pinning lines are visible, with bright depinning regions in between. The system size/width L is indicated.

matrix with elements

$$V_C(i,j) = \begin{cases} 1 & \text{for } V(i,j) \geq v_t \\ 0 & \text{for } V(i,j) < v_t \end{cases}, \qquad (2.31)$$

where $v_t = C_p \langle v \rangle$ is the threshold velocity. The parameter C_p is the threshold constant, an integer of a few unities, and $\langle v \rangle$ is the average propagation velocity of the crack front. For $C_p = 6$ and $\langle v \rangle = 0.17 \, \mu\text{m/s}$ a cropped region of V_C is shown in Fig. 2.9 a). The full size of V_C corresponds to the system size $L_x \times L_y$ (the size of a captured image). We show in Paper III that independently of C_p, clusters of high velocity show scale invariant behaviour up to some cutoff, both with respect to size and linear extension.

In addition to high-velocity avalanches, we consider also the statistics of low velocity pinning lines. Pinning lines are found by a similar thresholding procedure as in Eq. (2.31) but with reversed inequality signs, i.e. we consider velocities smaller than $v_t = C_p \langle v \rangle$. Figure. 2.8 shows for $C_p = 3$ and $\langle v \rangle = 1.36 \, \mu\text{m/s}$ the resulting thresholded matrix. The geometry of these pinning lines differ from high velocity avalanches, but as our study has shown, they share the same scaling properties.

Finally, the independence of the different loading conditions and average crack front velocity with respect to: statistical scaling, velocity distribution, and spatial and temporal velocity correlations, are amongst our findings.
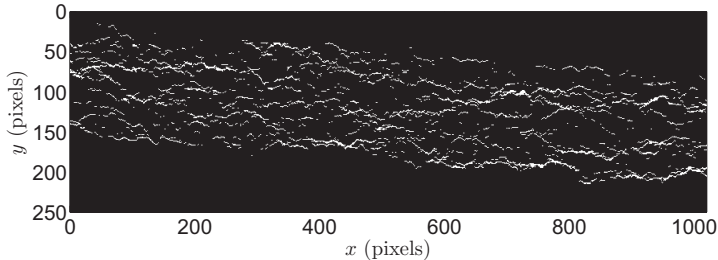
Figure 2.8: Pinning line matrix obtained for $C_p = 3$ and $\langle v \rangle = 1.36\,\mu\mathrm{m/s}$. Notice the difference in geometry of clusters compared to high velocity avalanches in Fig. 2.9 a).

2.4.3   Data analysis

In this section the robustness of the WTM procedure, introduced in the previous section and thoroughly described in Appendix A of Paper III, is demonstrated. Below, we consider a front subtraction method for obtaining avalanches along the fracture front. The purpose of introducing this algorithm is the comparison to the WTM method, and in this manner ensure that the extracted results in Paper III are not influenced by the chosen method of analysis.

The basis for this method is the front matrix $h(i, j)$, containing all captured fracture fronts during an experiment. The time index i runs from unity to the total number of captured images, the position index $1 \leq j \leq L_x$ denotes the position of the crack front along the $x-$axis, and h denotes the position of the crack front in the $y-$direction (see Fig. 2.6). Let Δ_t be the number of unit timesteps between two fronts to be subtracted (e.g $\Delta_t = 1$ is the timeresolution between two consecutive fronts) and let Δ_y be the distance (in pixels along the $y-$direction) the front has moved during Δ_t. We can now impose a threshold condition on Δ_t for a given value of Δ_y to isolate both high and low velocity regions of the fracture front. The front is considered to propagate at a high velocity between i and $i + \Delta_t$ if

$$h(i + \Delta_t, j) - h(i, j) \geq \Delta_y \; , \qquad (2.32)$$

for $1 \leq j \leq L_x$. It is now possible to obtain a binary matrix similar to V_C [Eq. (2.31)] by defining a zero matrix V_F of size $L_x \times L_y$. In looping through the front matrix $h(i, j)$ at a step of Δ_t for i and every j, the corresponding matrix elements $V_F(h(i, j) \rightarrow h(i + \Delta_t, j), j)$ are put to unity when the

condition in Eq. (2.32) is fullfilled. Note at this point that when all elements in V_F from $h(i,j)$ to $h(i+\Delta_t,j)$ are put to unity, it is implicitly assumped that also the fronts in between i and $i+\Delta_t$ obey Eq. (2.32). This assumption may not be fullfilled and could give rise to deviations, however the WTM method does not suffer from such problems.

a)

b)
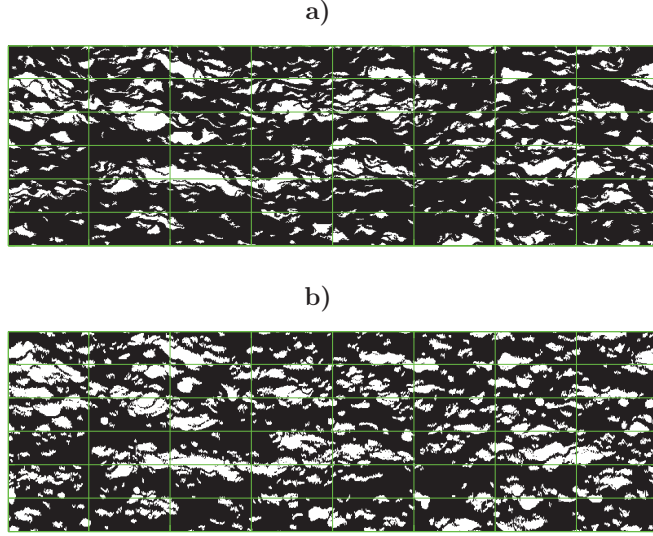
Figure 2.9: Thresholded velocity matrices showing high velocity avalanches for $C_p = 6$. One grid box has the dimensions 50×100 pixels. **a)** WTM method showing V_C, and **b)** front subtraction method showing V_F. To a large extent the two matrices are similar, but there are some deviations for smaller clusters, as these are more sensitive to experimental error.

In order to compare the WTM method and front subtraction, we have to threshold at approximately the same velocity. This is accomplished by rescaling Δ_y and Δ_t with the actual space and time resolution a_r and dt respectively. Thus from Eq. (2.31) it is required that

$$v_t = C_p \langle v \rangle = \frac{\Delta_y}{\Delta_t} \frac{a_r}{dt} \tag{2.33}$$

$$\Delta_t = \frac{\Delta_y}{C_p \langle v \rangle} \frac{a_r}{dt} . \tag{2.34}$$

Finally, Δ_t must be rounded to the closest integer value, since it is used as a matrix index. For the same parameters as was used to obtain V_C in Fig. 2.9 a), i.e. $C_p = 6$ and $\langle v \rangle = 0.17 \, \mu\text{m/s}$, we use $\Delta_y = 1$ for $a_r = 2.24 \, \mu\text{m}$ and $dt = 0.5 \, \text{s}$, giving $\Delta_t \approx 4$. The matrix V_F is shown in Fig. 2.9 b). In comparing V_F and V_C in Fig. 2.9, the structures are similar to a satisfactory degree, allthough there are deviations in shape and size, in particular for smaller clusters. However one can not expect to find identical clusters with the exact same perimeter and size, due to the different definitions of an high velocity avalanche in the two cases. In the WTM method, the velocity field is thresholded directly, whereas it is done so indirectly in front subtraction. It is also difficult to threshold at the exact same velocity due to integer rounding when using a Δ_t for a given C_p in Eq. (2.34). Finally, smaller clusters are more sensitive to experimental error such as pixel fluctuations in the apparatus, deviations in thresholding when obtaining the fronts and so on.

A more quantitative comparison can be made by considering the statistics of the clusters obtained with the two methods. Figure 2.10 shows the probability density function of cluster sizes using both the WTM and the front subtraction method, for two values of the threshold constant C_p. It is clear that the probability density functions are more or less equal in the two cases, thus we obtain the same statistical results.
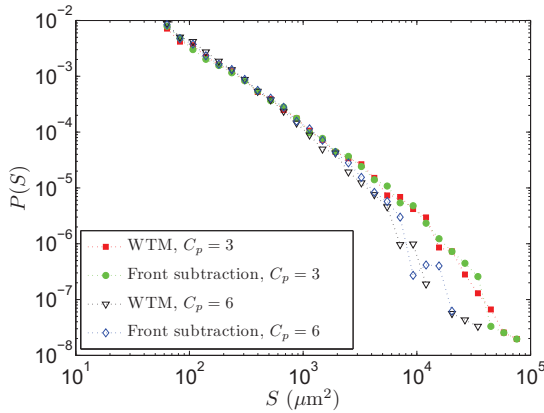
Figure 2.10: Probability density functions $P(S)$ for high velocity clusters of size S using both the WTM and front subtraction method. Filled and empty markers correspond to $C_p = 3$ and $C_p = 6$ respectively. It is apparent that the two methods produce the same statistics.

Note that this version of front subtraction is somewhat crude and might possibly be improved. In contrast to the WTM approach it does not give the actual velocity field of the fracture front, and has also shown to be more sensitive to experimental error, requiring a higher time resolution than the WTM method to be accurate.

Chapter 3

Summary of the papers

Paper I

In this paper the main experimental results from steady-state simultaneous two-phase flow in a quasi two-dimensional porous medium are presented. The wetting and the nonwetting phase are injected simultaneously from alternating inlet points into a Hele-Shaw cell containing one layer of randomly distributed glass beads, initially saturated with wetting fluid. The high viscous wetting phase and the low viscous nonwetting phase give a low viscosity ratio $M = 10^{-4}$. The dynamics is dominated by the interplay between a viscous pressure field from the wetting fluid and bubble transport of a less viscous, nonwetting phase. In contrast to more studied displacement front systems such as viscous and capillary fingering, steady-state flow is in equilibrium, in a statistical sense. This opens for a simpler theoretical description, so that the probability distribution of bubble sizes, depending on the Ca number, can be explained. From an equilibrium condition between the applied work rate on the system and the dissipation, we have been able to explain theoretically the experimentally found power law relation between the pressure gradient in the system and the capillary number.

Paper II

It is the same set of experiments that form the basis for Papers I and II. Paper II is an extension of Paper I, where both the transient and steady-state regimes of the flow are described. Transient behavior is followed in time and space. The duration of this regime is shown to scale with the Ca number, and it is observed that at a certain distance behind the initial front, a "local" steady-state develops. This region shares the same properties as the

later "global" steady-state. In this state, the nonwetting phase is fragmented into clusters, whose size distribution follows a scaling law, truncated by a characteristic cluster size. This cutoff is found to be inversely proportional to the capillary number. Furthermore it is demonstrated that a characteristic length scale, depending on the capillary number through the pressure gradient, controls the steady-state dynamics. Finally we devote a section to the effects of compressibility, since air is used as the nonwetting phase, and pressures can exceed several bars of atmospheric pressure.

Paper III

The propagation of a Mode I crack front along the heterogeneous weak plane of a transparent Plexiglas block is followed in space and time at high resolution. To study the effect of different boundary conditions, we apply two different loadings: 1) fracture is induced by opening the sample at a constant deflection velocity, and 2) the sample is opened to a deflection distance large enough to induce fracture and then kept fixed in this position. These loading conditions correspond to forced propagation and creep relaxation of the fracture respectively. The intermittent local dynamics for a wide range (over four decades) of average crack front velocities, has been of primary interest. We observe independently of loading conditions and average velocity, similar dynamics. From both visual inspection and statistical analysis of the velocity field, it is found that the fracture propagates through scale free pinning and depinning regions. Avalanches (depinning regions) of various sizes occur when the front jumps from one pinned configuration to the next. We have related the local fluctuations in the crack velocity to the distribution of avalanche sizes through a scaling relation. Additionally the analysis includes space-time correlations of the local velocities, and we find that the evolution of the width of the fracture front behaves as in simple diffusion growth.

Bibliography

[1] K. T. Tallakstad. *Steady-State, Simultaneous Two-Phase Flow in Porous Media*. M.Sc. thesis, University of Oslo, 2007.

[2] A. E. Scheidegger. *The physics of flow through porous media, Third Edition*. University of Toronto Press, 1974.

[3] D. G. Avraam and A. C. Payatakes. Flow regimes and relative permeabilities during steady-state two-phase flow in porous media. *J. Fluid Mech.*, 293:207–236, 1995.

[4] D. G. Avraam, G. B. Kolonis, T. C. Roumeliotis, G. N. Constantinides, and A. C. Payatakes. Steady-state two-phase flow through planar and nonplanar model porous media. *Transport in Porous Media*, 16:75–101, 1994.

[5] Jean Schmittbuhl and Knut Jørgen Måløy. Direct observation of a self-affine crack propagation. *Phys. Rev. Lett.*, 78(20):3888–3891, May 1997.

[6] Knut Jørgen Måløy, Stéphane Santucci, Jean Schmittbuhl, and Renaud Toussaint. Local waiting time fluctuations along a randomly pinned crack front. *Phys. Rev. Lett.*, 96(4):045501, Jan 2006.

[7] J. Bear. *Dynamics of Fluids in Porous Media*. American Elsevier Publishing Company, New York, 1972.

[8] F. A. L. Dullien. *Porous Media, Fluid Transport and Pore Structure, 2nd Edition*. Academic press, 1979.

[9] M. Sahimi. *Flow and transport in porous media and fractured rock: From classical methods to modern approaches*. Wiley-VCH, 1995.

[10] R. Lenormand, E. Touboul, and C. Zarcone. Numerical models and experiments on immiscible displacements in porous media. *J. Fluid Mech.*, 189:165–187, 1988.

[11] D. Wilkinson and J. F. Willemsen. Invasion percolation: a new form of percolation theory. *J. Phys. A: Math. Gen.*, 16(14):3365, 1983.

[12] Lincoln Paterson. Diffusion-limited aggregation and two-fluid displacements in porous media. *Phys. Rev. Lett.*, 52(18):1621–1624, Apr 1984.

[13] E. Aker, K. J. Måløy, A. Hansen, and G. G. Batrouni. A two-dimensional network simulator for two-phase flow in porous media. *Transport in Porous Media*, 32:163–186, 1998.

[14] O. Aursjø. *Two-Phase Flow in a Porous Medium Stimulated by Oscillations.* PhD thesis, University of Oslo, 2010.

[15] D. B. Das and S. M. Hassanizadeh. *Upscaling Multiphase Flow in Porous Media - From Pore to Core and Beyond.* Springer, Netherlands, 2005.

[16] Olav Aursjø, Henning Arendt Knudsen, Eirik G. Flekkøy, and Knut Jørgen Måløy. Oscillation-induced displacement patterns in a two-dimensional porous medium: A lattice boltzmann study. *Phys. Rev. E*, 82(2):026305, Aug 2010.

[17] M. Jankov. *Two phase flow in porous media with and without seismic stimulation.* PhD thesis, University of Oslo, 2010.

[18] L. D. Landau and E. M. Lifshitz. *Fluid Mechanics, 2nd Edition.* Butterworth-Heinemann, 1987.

[19] C. M. Marle. *Multiphase Flow in Porous Media.* Graham and Trotman Ltd., 1981.

[20] M. Sahimi. Flow phenomena in rocks: From continuum models to fractals, percolation cellular automata, and simulated annealing. *Rev. Mod. Phys.*, 65(4):1393–1534, 1993.

[21] W. B. Haines. Studies in the physical properties of soil. v. the hysteresis effect in capillary properties, and the modes of moisture distribution associated therewith. *The Journal of Agricultural Science*, 20(01):97–116, 1930.

[22] S. Maslov. Time directed avalanches in invasion models. *Phys. Rev. Lett.*, 74(4):562–565, 1995.

[23] Knut Jørgen Måløy, Liv Furuberg, Jens Feder, and Torstein Jøssang. Dynamics of slow drainage in porous media. *Phys. Rev. Lett.*, 68(14):2161–2164, Apr 1992.

[24] Liv Furuberg, Knut Jørgen Måløy, and Jens Feder. Intermittent behavior in slow drainage. *Phys. Rev. E*, 53(1):966–977, Jan 1996.

[25] Marek Cieplak and Mark O. Robbins. Dynamical transition in quasistatic fluid invasion in porous media. *Phys. Rev. Lett.*, 60(20):2042–2045, May 1988.

[26] Marek Cieplak and Mark O. Robbins. Influence of contact angle on quasistatic fluid invasion of porous media. *Phys. Rev. B*, 41(16):11508–11521, Jun 1990.

[27] Belita Koiller, Hong Ji, and Mark O. Robbins. Fluid wetting properties and the invasion of square networks. *Phys. Rev. B*, 45(14):7762–7767, Apr 1992.

[28] Grunde Løvoll, Yves Méheust, Renaud Toussaint, Jean Schmittbuhl, and Knut Jørgen Måløy. Growth activity during fingering in a porous hele-shaw cell. *Phys. Rev. E*, 70(2):026301, Aug 2004.

[29] P. G. Saffman and G. Taylor. The penetration of a fluid into a porous medium or hele-shaw cell containing a more viscous liquid. *Proc. Roy. Soc. A*, 245:312–329, 1958.

[30] Yves Méheust, Grunde Løvoll, Knut Jørgen Måløy, and Jean Schmittbuhl. Interface scaling in a two-dimensional porous medium under combined viscous, gravity, and capillary effects. *Phys. Rev. E*, 66(5):051603, Nov 2002.

[31] Olav Inge Frette, Knut Jørgen Måløy, Jean Schmittbuhl, and Alex Hansen. Immiscible displacement of viscosity-matched fluids in two-dimensional porous media. *Phys. Rev. E*, 55(3):2969–2975, Mar 1997.

[32] A. C. Payatakes and M. Dias. Immiscible microdisplacement and ganglion dynamics in porous media. *Reviews in Chemical Engineering*, 2:93–116, 1984.

[33] A. A. Griffith. The phenomena of rupture and flow in solids. *Philosophical Transactions*, 221:163–198, 1920.

[34] G. R. Irwin. Onset of fast crack propagation in high strength steel and aluminum alloys. *Sagamore Research Conference Proceedings*, 2:289–305, 1956.

[35] J. R. Rice. 1st-order variation in elastic fields due to variation in location of a planar crack front. *Journal of Applied Mechanics*, 52:571–579, 1985.

[36] D. Bonamy. Intermittency and roughening in the failure of brittle heterogeneous materials. *J. Phys. D: Appl. Phys.*, 42:214014, 2009.

[37] E. Bouchaud, G. Lapasset, and J. Planès. Fractal dimension of fractured surfaces: A universal value? *Europhys. Lett.*, 13(1):73, 1990.

[38] J. P. Sethna, K. A. Dahmen, and C. R. Myers. Crackling noise. *Nature (London)*, 410(2001):242–250.

[39] V. Z. Parton. *Fracture Mechanics: From Theory to Practice*. Gordon and Breach Science Publishers, 1992.

[40] C. E. Inglis. Stresses in a plate due to the presence of cracks and sharp corners. *Transactions of the Institute of Naval Architects*, 55:219–241, 1913.

[41] B. R. Lawn. *Fracture of Brittle Solids - Second Edition*. Cambridge University Press, 1993.

[42] T. L. Anderson. *Fracture Mechanics - Fundamentals and Applications, 2nd Edition*. CRC Press, 1995.

[43] L. B. Freund. *Dynamic Fracture Mechanics*. Cambridge University Press, 1990.

[44] J. W. Obreimoff. The splitting strength of mica. *Proceeding of the Royal Society of London A*, 127:290–297, 1930.

[45] S. P. Timoshenko and S. Woinowsky-Krieger. *Theory of Plates and Shells (2nd Edition)*. McGraw-Hill, 1959.

[46] M. Adda-Bedia, E. Katzav, and D. Vandembroucq. Second-order variation in elastic fields of a tensile planar crack with a curved front. *Phys. Rev. E*, 73(3):035106, Mar 2006.

[47] H. Gao and J. R. Rice. A first order perturbation analysis on crack trapping by arrays of obstacles. *J. Appl. Mech.*, 56:828, 1989.

[48] D. Bonamy, S. Santucci, and L. Ponson. Crackling dynamics in material failure as the signature of a self-organized dynamic phase transition. *Phys. Rev. Lett.*, 101(4):045501, Jul 2008.

[49] Deniz Ertaş and Mehran Kardar. Critical dynamics of contact line depinning. *Phys. Rev. E*, 49(4):R2532–R2535, Apr 1994.

[50] Gianfranco Durin and Stefano Zapperi. Scaling exponents for barkhausen avalanches in polycrystalline and amorphous ferromagnets. *Phys. Rev. Lett.*, 84(20):4705–4708, May 2000.

[51] Alejandro B. Kolton, Alberto Rosso, and Thierry Giamarchi. Creep motion of an elastic string in a random potential. *Phys. Rev. Lett.*, 94(4):047002, Feb 2005.

[52] Damien Vandembroucq, Rune Skoe, and Stéphane Roux. Universal depinning force fluctuations of an elastic line: Application to finite temperature behavior. *Phys. Rev. E*, 70(5):051101, Nov 2004.

[53] S. Santucci, L. Vanel, and S. Ciliberto. Slow crack growth: Models and experiments. *Eur. Phys. J. Special Topics*, 146:341–356, Jul 2007.

[54] Jean Schmittbuhl, Jean-Pierre Vilotte, and Stéphane Roux. Reliability of self-affine measurements. *Phys. Rev. E*, 51(1):131–147, Jan 1995.

[55] J. Feder. *Fractals*. Plenum Press New York, 1988.

[56] L. Ponson, D. Bonamy, and E. Bouchaud. Two-dimensional scaling properties of experimental fracture surfaces. *Phys. Rev. Lett.*, 96(3):035506, Jan 2006.

[57] Knut Jørgen Måløy, Alex Hansen, Einar L. Hinrichsen, and Stéphane Roux. Experimental measurements of the roughness of brittle cracks. *Phys. Rev. Lett.*, 68(2):213–215, Jan 1992.

[58] Xiaodong Zhang, M. A. Knackstedt, D. Y. C. Chan, and L. Paterson. On the universality of fracture surface roughness. *Europhys. Lett.*, 34:121–126, 1996.

[59] Arnaud Delaplace, Jean Schmittbuhl, and Knut Jørgen Måløy. High resolution description of a crack front in a heterogeneous plexiglas block. *Phys. Rev. E*, 60(2):1337–1343, Aug 1999.

[60] M. Grob, J. Schmittbuhl, R. Toussaint, L. Rivera, S. Santucci, and K. J. Måløy. Quake catalogs from an optical monitoring of an interfacial crack propagation. *Pure Appl. Geophys.*, 166:777–799, 2009.

Part II

Papers

PHYSICAL REVIEW LETTERS

Steady-State Two-Phase Flow in Porous Media: Statistics and Transport Properties

Ken Tore Tallakstad,[1] Henning Arendt Knudsen,[1] Thomas Ramstad,[2,3] Grunde Løvoll,[1] Knut Jørgen Måløy,[1]
Renaud Toussaint,[4] and Eirik Grude Flekkøy[1]

[1]*Department of Physics, University of Oslo, P.B. 1048 Blindern, NO-0316 Oslo, Norway*
[2]*Department of Physics, Norwegian University of Science and Technology, NO-7491 Trondheim, Norway*
[3]*Numerical Rocks AS, Stiklestadveien 1, NO-7041 Trondheim, Norway*
[4]*Institut de Physique du Globe de Strasbourg, UMR 7516 CNRS, Université de Strasbourg,
5 rue René Descartes, F-67084 Strasbourg Cedex, France*
(Received 16 October 2008; published 18 February 2009)

We study experimentally the case of steady-state simultaneous two-phase flow in a quasi-two-dimensional porous media. The dynamics is dominated by the interplay between a viscous pressure field from the wetting fluid and bubble transport of a less viscous, nonwetting phase. In contrast with more studied displacement front systems, steady-state flow is in equilibrium, statistically speaking. The corresponding theoretical simplicity allows us to explain a data collapse in the cluster size distribution as well as the relation $|\nabla P| \propto \sqrt{\text{Ca}}$ between the pressure gradient in the system and the capillary number.

Different types of immiscible multiphase fluid flow in porous media play an important role in many natural and commercial processes [1–3]. The complex fluid patterns observed in such processes have been extensively studied and modeled over the past decades; see [1–5], and references therein.

The vast majority of work up to now has focused on invasion processes: either pure drainage or pure imbibition. These inherently transient processes give different displacement patterns and are classified into capillary fingering [6], viscous fingering [5,7–12], and stable front displacement [13,14]. These are nonstationary processes, and to understand them in a broader context there is a need to understand the stationary case which has received far less attention: steady-state flow, which is in equilibrium in the sense that average flow properties and distribution functions are invariant in time. This stationary system is in statistical equilibrium although it is a dissipative process; an external energy input balances the internal energy loss to maintain the equilibrium.

With some notable exceptions, there is to our knowledge very little pore scale experimental data available for such problems [15]. The Payatakes group did pore scale steady-state experiments using network models etched in glass [16] and later theoretical modeling predicting the nonlinearity of such flows [17]. In addition, some numerical work has focused on a steady-state regime: a pore scale lattice Boltzmann study by Gunstensen and Rothman [18] and network simulations at larger scales by Knudsen *et al.* and Ramstad *et al.* [19–22].

In this Letter, we experimentally demonstrate that an equilibrium flow situation results after simultaneous injection of two fluids into a porous medium. This allows for the combination of mean-field approximations of local quantities and energy dissipation considerations. As a result, we analytically obtain the highly nontrivial steady-state

pressure-flow-rate relationship. Furthermore, in contrast to transient flows, steady-state mass conservation gives a normalization condition based on flow rate rather than saturation. From this we derive a scaling law of the cluster size distributions of nonwetting fluid.

Our system is shown in Fig. 1. The horizontal porous model consists of a monolayer of glass beads of diameter $a = 1$ mm, which are randomly spread between two transparent contact papers [7,13]. The model dimensions are $L \times W = 85 \times 42$ cm^2, with thickness a and volume $V = aLW$. The porosity and absolute permeability are measured to be $\phi_0 = 0.63$ and $\kappa_0 = (1.95 \pm 0.1) \times 10^{-5}$ cm^2, respectively. The wetting fluid used is a 85%–15% by
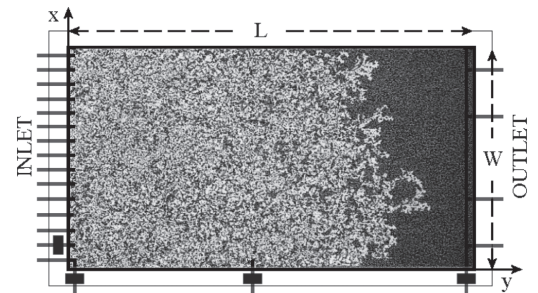
FIG. 1. Depicted inside the model frame ($L \times W = 85 \times 42$ cm^2) is the initial transient stage of an experiment. There are 15 independent inlet holes with tubes and syringes attached. Every second syringe injects the wetting phase; the others inject the nonwetting one. An outlet channel with four exit holes allows the fluid mix to leave the system. Three *SensorTechnics 26PC0100G6G* flow-through pressure sensors (indicated by the solid rectangles) are attached alongside the model at the positions $y = 0, L/2, L$. Additionally, one pressure sensor is attached to the first ''air'' tube from the bottom.

weight *glycerol-water* solution dyed with 0.1% Negrosine and has a viscosity $\mu_w = 0.11$ Pa s at room temperature. *Air* is used as the nonwetting fluid with viscosity $\mu_{nw} = 1.9 \times 10^{-5}$ Pa s, giving a viscosity ratio $M = \mu_{nw}/\mu_w \sim 10^{-4}$. The surface tension is measured to be $\gamma = 6.4 \times 10^{-2}$ N m^{-1}.

The tuning parameter in the experiments is the total flow rate, i.e., the sum of the flow rate of the wetting and nonwetting fluid, and can during steady state be written as $Q_{tot} = Q_w + Q_{nw} = (8 + 7)Q_0$, where Q_0 is the flow rate from every single syringe.

Gray scale images of the flow structure are taken at regular intervals with a *Pixelink Industrial Vision PL-A781* digital camera. An image contains 3000×2208 pixels, corresponding to a spatial resolution of ~ 0.19 mm per pixel (27 pixels in a pore of size 1 mm^2). All analysis is done on the basis of black and white thresholded images [14] and the measured pressure signals.

The porous model is initially saturated with the wetting phase. An experiment is started by injecting the fluid pair from every other inlet hole. The initial structure consists of bubbles or clusters of air distributed over various sizes, but always much smaller than the system size. The clusters are embedded in a background field of percolating wetting fluid. Usually, the smallest air clusters are immobile and trapped, whereas larger clusters are mobile and propagate in the porous medium. However, trapped clusters can be mobilized when they coalesce with larger migrating clusters, and migrating clusters can be fragmented and thereby trapped.

We divide an experiment into two regimes. A *transient* regime where the mix of nonwetting clusters and wetting fluid gradually fills up the model, as seen in Fig. 1. During this time, the measured average pressure difference between $y = 0$ and $y = L$, ΔP_L, increases. This is due to the presence of more and more air clusters trapped in the system, effectively lowering the relative permeability for the viscous wetting fluid. At some characteristic time, shortly after both phases are produced at the outlet, ΔP_L starts to fluctuate around a constant value. This marks the start of the *steady-state* (or statistically stationary) regime. The whole model now contains a homogeneous mix of the two phases, transported through the model without "long time" flow parameter changes.

Through six experiments we have studied how the measured steady-state pressure difference ΔP_L varies with the capillary number Ca, defined as

$$\text{Ca} = \frac{\mu_w Q_w a^2}{\gamma \kappa_0 A}, \qquad (1)$$

where $A = Wa$ is the cross-sectional area. This is shown in Fig. 2, for a span in the Ca number of roughly two decades. The steady-state pressure fluctuations are Gaussian, indicating that ΔP_L results from a sum of independent, local pressure differences over scales smaller than the system size. It is evident that the pressure is consistent with a power law in the Ca number $\Delta P_L \propto \text{Ca}^\beta$, where the ex-
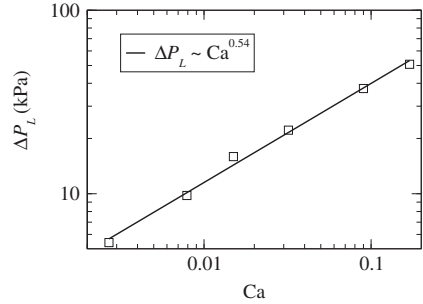

FIG. 2. Mean pressure difference ΔP_L during steady state as a function of Ca. The fluctuations in ΔP_L are of the order of 1 kPa, i.e., very small compared to the mean values. A power law dependence is found, with exponent $\beta = 0.54 \pm 0.08$.

ponent is found to be $\beta = 0.54 \pm 0.08$. This is a nontrivial result, and we will return to the discussion shortly.

A general trend in the experiments, in passing from high to low Ca numbers, is that the size or area of the largest air clusters increases. This means that the geometry of the clusters depends on the steady-state pressure gradient. To quantify this, we have found the normalized probability distributions of cluster extension in the x and y directions, $P(l_x)$ and $P(l_y)$, respectively (see Fig. 3). We define the extension lengths l_x and l_y as the sides of the smallest rectangle (bounding box) that can contain a cluster. For clarity, l_y lays parallel whereas l_x lays transverse to the average flow direction.

Analysis shows that, for a cluster of a given area s, the extension lengths have well defined means $\langle l_x \rangle$ and $\langle l_y \rangle$ increasing monotonically with s [23]. The corresponding
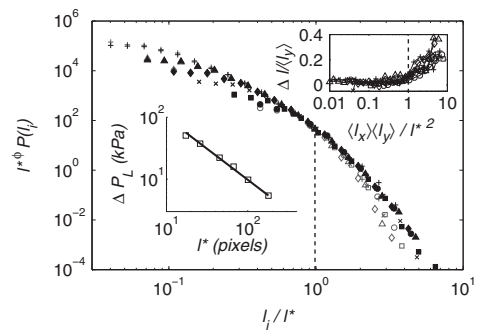
FIG. 3. Air cluster extension length distributions $P(l_y)$ (filled markers) and $P(l_x)$ (empty markers), collapsed by the rescaling $l^{*\phi}P(l_i)$ vs l_i/l^*, where $i \in \{x, y\}$ and $\phi = 2.8$. The dashed vertical line at $l_i = l^*$ indicates the start of the different cutoff behavior in the two directions. The lower left inset shows (solid line) $\Delta P_L \propto 1/l^*$ with the corresponding experimental values (squares). The upper right inset shows $\Delta l/\langle l_y \rangle$ vs $\langle l_x \rangle \langle l_y \rangle / l^{*2}$, where $\Delta l = \langle l_y \rangle - \langle l_x \rangle$.

standard deviations are small and proportional to these means (relatively 20%) for all $\langle l_x \rangle$ and $\langle l_y \rangle$ values [23]. Furthermore, we find that $\langle l_x \rangle = \langle l_y \rangle$ up to a characteristic length scale in the system l^*. Above l^*, $\langle l_y \rangle > \langle l_x \rangle$, as shown in the upper right inset in Fig. 3. The exact same behavior is seen in the distributions $P(l_x)$ and $P(l_y)$. Figure 3 shows, for the same Ca numbers used previously, a collapse of the $P(l_x)$ and $P(l_y)$ distributions by the rescaling $l^{*\phi} P(l_i)$ vs l_i/l^*. The scaling exponent $\phi = 2.8 \pm 0.3$ is taken as the value that gives the best collapse. Apart from the expected crossover when the extension lengths reaches the pore length scale a, the collapse is very good. The above results reveal important information of our system, particularly that there is only one length scale l^*, dependent on the pressure difference ΔP_L, that controls the steady-state displacement structure.

In the following, we shall give a simple and minimal scaling theory for the purpose of predicting the exponents β and ϕ from Figs. 2 and 3 respectively.

Consider a nonwetting cluster in the porous medium surrounded by flowing viscous wetting fluid. The cluster perimeter is made up of several menisci standing in different pores. A single meniscus at a particular position has a surface pressure given by the pressure difference of the nonwetting and wetting fluid on each side. The nonwetting fluid pressure is assumed constant inside the cluster due to its low viscosity, whereas the wetting fluid pressure is position-dependent, decreasing in the y direction. The neighboring pores inside and outside the meniscus can be either imbibed or drained, respectively, if the surface pressure exceeds one of the capillary pressure thresholds for imbibition or drainage. The imbibition and drainage threshold pressures depend on pore geometry and are thus distributions due to the randomness of the porous medium [24].

If all menisci along the perimeter are in mechanical equilibrium, the cluster is *immobile*. This is typically the case for clusters with only a small l_y extension. However, for large enough l_y, the viscous pressure drop on the wetting side of the perimeter is sufficient for a migration step to take place. Migration is the process of drainage in one pore and imbibition in another along the perimeter. The result of several migration steps is that the cluster moves and perhaps also changes shape. The onset of migration will depend on the difference between the mean threshold pressure for drainage and imbibition [24], a pressure we denote $\bar{P}_t$. Furthermore, $\bar{P}_t$ predicts a characteristic length of extension l^* for cluster *mobility*

$$|\nabla P| l^* = \Delta P_L \frac{l^*}{L} = \bar{P}_t, \qquad (2)$$

where we make the mean-field assumption that the pressure gradient $|\nabla P|$ is constant. The scaling of the last equality in Eq. (2) is verified experimentally, as shows the lower left inset in Fig. 3. Note that l^* also determines when clusters become unstable against breakup, since the mechanism of cluster mobilization is the same as that of cluster fragmentation. This is important because it links the single crossover length that collapses both $P(l_i)$ distributions in Fig. 3 to the extension of mobilized clusters. Particularly, it means that the characteristic l_x extension of mobilized clusters is l^*.

Equilibrium conditions require the total dissipation in the system to be balanced by the work rate done through the external pressure drop: $Q_{tot} \Delta P_L = D_f$. In obtaining D_f, we assume that the main contribution to dissipation is in the volume of the wetting fluid and that the dissipation in the nonwetting fluid is negligible. Visual observation indicates that most of the wetting fluid is restricted to flow through narrow channels at some typical spacing. The motion and configuration of the nonwetting clusters seem to show that the channel width is of the order of a pore size $\sim a$ and that the permeability in between channels is made relatively low by the presence of lowly mobile nonwetting clusters. Motivated by these observations, we define a dissipative wetting fluid volume:

$$V_{dis} = L A_{dis} = L a^2 \frac{W}{l^*} = \frac{aV}{l^*}, \qquad (3)$$

where l^* is taken as the spacing between channels, making W/l^* the number of channels through the system. This simplification of channel flow of the wetting fluid is a strong assumption, but supporting numerical simulations also show that the dissipative volume is constrained to a small fraction of the total volume, changing with the flow rate.

Since the overall interface area between the wetting and nonwetting phase is fluctuating around a constant value in steady state, changes in the potential energy stored in the interfaces do not contribute to the average dissipation, and we are justified in writing

$$Q_{tot}\Delta P_L = D_f = -\int_{V_{dis}} dV u |\nabla P| = \frac{\mu_w}{\kappa_0} \int_{V_{dis}} dV u^2, \quad (4)$$

where we have applied Darcy's law locally, in the dissipative part of the wetting fluid. Taking the local Darcy velocity $u = (Q_w/A)(V/V_{dis})$ as a constant, and using Eqs. (3), (1), and (2), respectively, we obtain

$$\Delta P_L = \frac{8\gamma V l^*}{15 a^3 A} \mathrm{Ca} \Rightarrow |\nabla P|^2 = \frac{8\gamma \bar{P}_t}{15 a^3} \mathrm{Ca}, \qquad (5)$$

i.e., $|\nabla P| \propto \sqrt{\mathrm{Ca}}$, consistent with the exponent β in Fig. 2. An alternative interpretation of this result is that the wetting fluid experiences an effective permeability, assuming a Darcy law $\kappa_{eff}(\mathrm{Ca}) = \mu_w Q_w/A|\nabla P|$, due to the flow of air:

$$\kappa_{eff}^2 = \frac{15\gamma}{8a\bar{P}_t} \kappa_0^2 \mathrm{Ca}. \qquad (6)$$

We turn now to the distributions of cluster extension lengths and the found exponent ϕ. From the collapses in Fig. 3, it is seen that the distributions can be written

$$P_i(l) = l^{-\phi} h_i(l/l^*), \qquad (7)$$

where the cutoff functions $h_i(x)$ are dominating. Note that

this scaling form should be expected to hold only for l above the lower cutoff scale $\sim a$. To obtain ϕ, we use the fact that the nonwetting flow rate is an imposed quantity and must in steady state be equal to the accumulated flow of all mobile clusters on the average. The contribution of a single cluster of extent l to the total nonwetting flow rate is $alU(l)$, where $U(l)$ is the average center of mass velocity. Further, the average number of clusters of extension $(l, l + dl)$ that intersects any given cross section A is given as $dlP_i(l)Nl/L$. Hence we can write

$$Q_{nw} = \frac{aN}{L} \int_a^\infty dll^2 U(l) P_i(l), \qquad (8)$$

where N is the total number of clusters. This number is measured and found to depend only weakly, at most logarithmically, on Q_{nw}. For simplicity, N will be treated as a constant in the following.

To obtain $U(l)$, we make the general assumption that it is linear in Q_{nw} and has some functional dependence on l/l^*:

$$U(l) = \frac{Q_{nw}}{A} f(l/l^*). \qquad (9)$$

As a first-order approximation, $f(x)$ would be a step function, since clusters of size $l < l^*$ usually are immobile. By Eqs. (7) and (9) and the substitution $x = l/l^*$, Eq. (8) can be written

$$1 = l^{*(3-\phi)} \frac{aN}{V} \int_{a/l^*}^\infty dx x^{2-\phi} f(x) h_i(x). \qquad (10)$$

Since the right-hand side of Eq. (10) must be independent of l^*, we obtain $\phi = 3$ consistent with the experimental value in Fig. 3.

In conclusion, experiments have been done on two-phase flow in a porous medium under steady-state conditions. In contrast to invasion processes and other inherently transient phenomena of two-phase flow, steady state is in a statistical sense an equilibrium situation. Whereas the description of transient behavior is a whole range of separate loosely attached cases, depending on flow parameters, the description and formalism for steady state should be more integrated and universal. Our work explores a part of its parameter space, and we find a robust power law behavior: Pressure increases as $\Delta P_L \propto \text{Ca}^{0.5}$, alternatively for permeability $\kappa_{\text{eff}} \propto \text{Ca}^{0.5}$.

The power law is valid over roughly two decades, but there should be cutoffs for large and small flow rates. For high flow rate, the cutoff cluster size will approach the pore size, and from that point the permeability must reach a plateau. The same is the case for flow rates low enough that the largest clusters are limited by the system size. These limits were not realized experimentally, but in numerical work these cutoffs have been seen [20,22].

The scaling behavior of the system was explained by theoretical arguments, relying on a high viscosity ratio. Numerical work with a lower viscosity ratio (steady state but somewhat different boundary conditions) indicates a lower exponent: $\Delta P_L \propto \text{Ca}^{\beta'}$, where $\beta' < 0.5$ [20]. We conjecture that the presented theory is a limiting case and thus is suitable as a starting point for further theoretical developments, aiming at incorporating the more complex case where the two fluids have more similar viscosities.

[1] J. Bear, *Dynamics of Fluids in Porous Media* (Elsevier, New York, 1972).
[2] F. A. L. Dullien, *Porous Media Fluid Transport and Pore Structure* (Academic, San Diego, 1992), 2nd ed.
[3] M. Sahimi, *Flow and Transport in Porous Media and Fractured Rock* (VCH Verlagsgesellschaft mbH, Weinheim, 1995).
[4] R. Lenormand, E. Touboul, and C. Zarcone, J. Fluid Mech. **189**, 165 (1988).
[5] P. G. Saffman and G. Taylor, Proc. R. Soc. A **245**, 312 (1958).
[6] R. Lenormand and C. Zarcone, Phys. Rev. Lett. **54**, 2226 (1985).
[7] G. Løvoll, Y. Meheust, R. Toussaint, J. Schmittbuhl, and K. J. Måløy, Phys. Rev. E **70**, 026301 (2004).
[8] L. Paterson, Phys. Rev. Lett. **52**, 1621 (1984).
[9] K. J. Måløy, J. Feder, and T. Jøssang, Phys. Rev. Lett. **55**, 2688 (1985).
[10] J. P. Stokes, D. A. Weitz, J. P. Gollub, A. Dougherty, M. O. Robbins, P. M. Chaikin, and H. M. Lindsay, Phys. Rev. Lett. **57**, 1718 (1986).
[11] J.-D. Chen and D. Wilkinson, Phys. Rev. Lett. **55**, 1892 (1985).
[12] R. Toussaint, G. Løvoll, Y. Meheust, K. J. Måløy, and J. Schmittbuhl, Europhys. Lett. **71**, 583 (2005).
[13] O. I. Frette, K. J. Måløy, J. Schmittbuhl, and A. Hansen, Phys. Rev. E **55**, 2969 (1997).
[14] Y. Meheust, G. Løvoll, K. J. Måløy, and J. Schmittbuhl, Phys. Rev. E **66**, 051603 (2002).
[15] M. J. Oak, L. E. Baker, and D. C. Thomas, J. Pet. Technol. **42**, 1054 (1990).
[16] D. G. Avraam and A. C. Payatakes, J. Fluid Mech. **293**, 207 (1995).
[17] M. S. Valavanides and A. C. Payatakes, Adv. Water Resour. **24**, 385 (2001).
[18] A. K. Gunstensen and D. H. Rothman, J. Geophys. Res. **98**, 6431 (1993).
[19] H. A. Knudsen, E. Aker, and A. Hansen, Transp. Porous Media **47**, 99 (2002).
[20] H. A. Knudsen and A. Hansen, Phys. Rev. E **65**, 056310 (2002).
[21] H. A. Knudsen and A. Hansen, Europhys. Lett. **65**, 200 (2004).
[22] T. Ramstad and A. Hansen, Phys. Rev. E **73**, 026306 (2006).
[23] K. T. Tallakstad, G. Løvoll, H. A. Knudsen, T. Ramstad, and K. J. Måløy (to be published).
[24] H. Auradou, K. J. Måløy, J. Schmittbuhl, and A. Hansen, Transp. Porous Media **50**, 267 (2003).

II

Steady-state, simultaneous two-phase flow in porous media: An experimental study

Ken Tore Tallakstad,[1,*] Grunde Løvoll,[1] Henning Arendt Knudsen,[1] Thomas Ramstad,[2,3]
Eirik Grude Flekkøy,[1] and Knut Jørgen Måløy[1]

[1]*Department of Physics, University of Oslo, PB 1048 Blindern, NO-0316 Oslo, Norway*
[2]*Department of Physics, Norwegian University of Science and Technology, NO-7491 Trondheim, Norway*
[3]*Numerical Rocks AS, Stiklestadveien 1, NO-7041 Trondheim, Norway*

We report on experimental studies of steady-state two-phase flow in a quasi-two-dimensional porous medium. The wetting and the nonwetting phases are injected simultaneously from alternating inlet points into a Hele-Shaw cell containing one layer of randomly distributed glass beads, initially saturated with wetting fluid. The high viscous wetting phase and the low viscous nonwetting phase give a low viscosity ratio $M = 10^{-4}$. Transient behavior of this system is observed in time and space. However, we find that at a certain distance behind the initial front a "local" *steady-state* develops, sharing the same properties as the later "global" steady state. In this state the nonwetting phase is fragmented into clusters, whose size distribution is shown to obey a scaling law, and the cutoff cluster size is found to be inversely proportional to the capillary number. The steady state is dominated by bubble dynamics, and we measure a power-law relationship between the pressure gradient and the capillary number. In fact, we demonstrate that there is a characteristic length scale in the system, depending on the capillary number through the pressure gradient that controls the steady-state dynamics.

I. INTRODUCTION

There is truly a broad range of different immiscible multiphase flows in porous media [1–3]. Intrigued by the observed complex dynamics and geometry, researchers have over the past decades taken great interest to explain and model these systems [1–7]. Not only is it important to understand these processes from a scientific point of view, but there are also huge commercial advantages. Many questions in this field still remain unanswered; thus, to develop a better understanding is highly warranted.

Traditionally, experimental and theoretical works focused on invasion processes: pure drainage (a nonwetting fluid displacing a wetting fluid from a porous medium), or pure imbibition (a wetting fluid displacing a nonwetting fluid from a porous medium) [8,9]. Different displacement patterns were observed and classified into capillary fingering [6,10], which has been modeled by invasion percolation [11], viscous fingering [7,12–16], and stable front displacement [8,17,18]. Later experimental work has also been done by Tsakiroglou *et al.*, focusing on transport coefficients of such systems [19–22]. The common feature of these effects is that they are inherently transient. In large-scale reservoir systems there will be regions and length scales where one or both of the fluids are fragmented and transported as bubbles, i.e. dynamically very different from the regimes described above. This transport is governed by the interplay and competition between drainage and imbibition, and it is not sufficient to look at these two processes separately. We therefore approach this problem by studying the steady-state regime experimentally on laboratory scale inside "a representative elementary volume."

This kind of flow regime, where drainage and imbibition are occurring simultaneously, has received less attention than the now classic "pure invasion" problems. There is a short literature listing of steady-state pore-scale studies, but to the best of our knowledge little experimental data are available. Avraam and Payatakes [23–25] did pore-scale steady-state experiments using etched two-dimensional glass models. Their main focus was relative permeability and a qualitative description and classification of flow regimes. Payatakes and co-workers worked on numerical modeling and theory for such problems [26–30]. In an experimental setup quite similar to ours, Vedvik *et al.* did experiments on fragmentation of capillary fingering clusters in a background viscous field [31]. Also numerical work has focused on a steady-state regime. By means of two-dimensional numerical network simulations Knudsen *et al.* and Ramstad and Hansen studied average flow properties and cluster formation in steady-state two-phase flow [32–35].

In this paper we report on an experiment, in which a nonwetting fluid with low viscosity (air) and a highly viscous wetting fluid (a glycerin/water solution) simultaneously are injected into a horizontal two-dimensional porous medium. Hence, gravity has no influence on the displacement. The medium is initially saturated with the wetting fluid, and we investigate the initial transient regime, where the two fluids mix, invade, and fill the system. We demonstrate that a steady state is reached after some characteristic time. By letting the injection continue beyond this point, we study the flow dynamics and transport properties in steady state. The main characteristic of this process is that the nonwetting fluid is broken up and transported through the system as disconnecting bubbles. We therefore pay special attention to the size distribution of nonwetting clusters (bubbles). For six different injection rates (spanning a range of two orders of magnitude), the probability density of cluster size is measured and found to obey a scaling law. We also report results
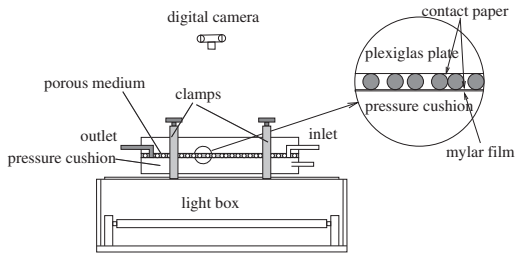
_____
*k.t.tallakstad@fys.uio.no

FIG. 1. Sketch of the experimental setup with the light box for illumination, the porous model, and the digital camera. The porous medium is sandwiched between two contact papers and kept together and temperature controlled with a water-filled pressure cushion.

on the relation between the global pressure, a characteristic cluster length scale, and the capillary number.

II. EXPERIMENTAL SETUP

The experimental setup is shown in Figs. 1 and 2. We use a monolayered porous stratum consisting of glass beads of diameter $a=1$ mm, randomly spread between two contact
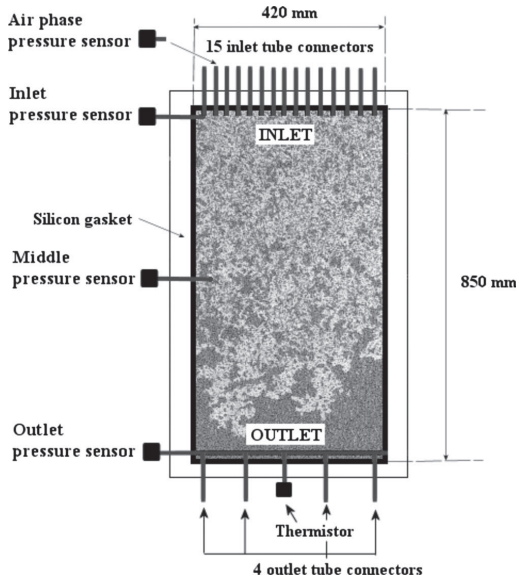

FIG. 2. Sketch of the experimental model. There are 15 independent inlet holes with attached tubes where we inject (alternately) the wetting and the nonwetting phase with syringe pumps. This leads to a mixing of the two phases inside the model two-dimensional porous medium (a random monolayer of glass beads) and a mix of the two phases flows out of the outlet channel at the opposite end of the system. In one of the inlet tubes (nonwetting phase) and in the porous model (wetting phase) pressure sensors are mounted for pressure measurements.

TABLE I. Geometrical parameters of the experimental setup and measured fluid properties. The absolute permeability κ_0 is measured in a separate experiment with the wetting fluid only.

Description	Symbol	Value
Model length	L	850 mm
Model width	W	420 mm
Bead diameter	a	1.0 mm
Porosity	ϕ_0	0.63
Permeability	κ_0	$(1.95 \pm 0.1) \times 10^{-5}$ cm^2
Wetting fluid viscosity	μ_w	0.11 Pa s
Nonwetting fluid viscosity	μ_{nw}	1.9×10^{-5} Pa s
Wetting fluid density	ρ_w	1217 kg m^{-3}
Nonwetting fluid density	ρ_{nw}	1.168 kg m^{-3}
Viscosity ratio	M	$\sim 10^{-4}$
Surface tension	γ	6.4×10^{-2} N m^{-1}

papers [16,17]. The model is a transparent rectangular box of dimensions $L \times W = 850 \times 420$ mm^2 and thickness a (see Table I for a listing of model parameters).

A 2-cm-thick Plexiglas plate is placed on top of the model. In order to squeeze the beads and the contact paper together with the upper plate, a Mylar membrane mounted on a 2.5-cm-thick Plexiglas plate, below the model, is kept under a 3.5 m water pressure as a "pressure cushion." The upper and the lower plates are kept together by clamps, and the side boundaries are sealed by a rectangular silicon rubber packing. The upper plate has 15 independent drilled inlets for fluid injection and a milled outlet channel (Fig. 2). The distance between the inlets and the outlet channel defines the length of the model.

The wetting fluid used in all our experiments is a 85 -15 % by weight *glycerol-water* solution dyed with 0.1% Negrosine (black color). *Air* is used as the nonwetting fluid. This gives a black and white fluid pair with good visual contrast. The wetting and the nonwetting fluids have viscosities of $\mu_w \approx 0.11$ Pa s and $\mu_{nw} = 1.9 \times 10^{-5}$ Pa s, respectively. The viscous ratio is thus $M = \mu_{nw}/\mu_w \sim 10^{-4}$, which is typical for a gas/liquid system. Other fluid parameters are found in Table I. The model is held at a constant temperature of 20 °C during the experiments. This is monitored by measuring the temperature in the wetting fluid at the outlet, thus allowing an accurate estimation of the viscosity of the fluid.

During experiments the pressure is recorded at four different positions, in one of the air inlet tubes and in the wetting fluid at the edge of the model: close to the inlet, at a distance $L/2$ in the flow direction, and in the outlet channel (Fig. 2) using SensorTechnics 26PC0100G6G Flow Through pressure sensors.

The flow structure is visualized by illuminating the model from below with a light box and pictures are taken at regular intervals with a Pixelink Industrial Vision PL-A781 digital camera, which is controlled by a computer over a FireWire connection. This computer records both the pictures and the pressure measurements. Each image contains 3000 $\times 2208$ pixels, which corresponds to a spatial resolution of ~ 0.19 mm per pixel (27 pixels in a pore of size of 1 mm^2).

The color scale contains 256 gray levels. The gray level distribution of the image presents two peaks corresponding, respectively, to the white air-filled and dark gray glycerol-filled parts of the image. The image is thresholded at a constant offset from the white peak so as to obtain a representative boundary between the two phases [18]. All further image treatments are performed on the resulting black and white image. The exact choice of the threshold value influences the extracted results. However, by visual inspection and analyses of results from a range of threshold values around the chosen one, the deviations are found to be small and systematic with this perturbation. We therefore claim that this procedure of choosing the threshold value is consistent and that the resulting data may be compared directly.

Close to the inlet and to a small degree along the model perimeter, there are boundary effects in the displacement structure. To avoid these, we define a (69×30) cm region of interest (ROI) in the central part of the model. Image analysis is then performed only inside this ROI.

In all experiments the porous model is initially filled with the wetting glycerol-water solution. An experiment is then started by injecting the wetting fluid and the nonwetting fluid from every other inlet hole (Fig. 2). Counting from one side this means that syringes $1,3,5,\ldots,15$ altogether eight individual syringes for the wetting fluid are used for the injection. Similarly, syringes $2,4,6,\ldots,14$ altogether seven individual syringes are used for the nonwetting fluid. The movements of all 15 syringes are controlled by the same step motor, setting an equal displacement rate.

III. RESULTS

As the nonwetting fluid enters the model, it first forms elongated clusters which are connected with their respective inlets. As these clusters grow, they are snapped off by the wetting fluid and transported as bubbles along the flow toward the outlet of the model. Over time the nonwetting air clusters propagate all the way to the outlet of the model, thus filling the whole porous matrix with a mixture of air and glycerol-water solution. The air only exists in the form of fragmented clusters while the glycerol-water solution percolates the model at all times. It is observed that the smallest air clusters usually are immobile and trapped. Larger clusters on the other hand are mobile and propagate in the porous medium. However, mobilization of trapped clusters can occur when they coalesce with larger migrating clusters. Conversely, fragmentation and trapping of migrating clusters also take place, so the fate of an air cluster is thus highly undecided. In this context it is worth mentioning the detailed pore-scale study of cluster mobilization and entrapment by Avraam and Payatakes [23,39].

We run the experiment for a significant time after air breakthrough. Shortly after breakthrough the transport process reaches steady state, meaning that both phases are transported through the model without "long-time" flow parameter changes, implying that the pressure difference, relative permeabilities, saturations, and cluster distributions are on average constant. Images of the evolution of the transient part of a typical experiment are shown in Fig. 3.
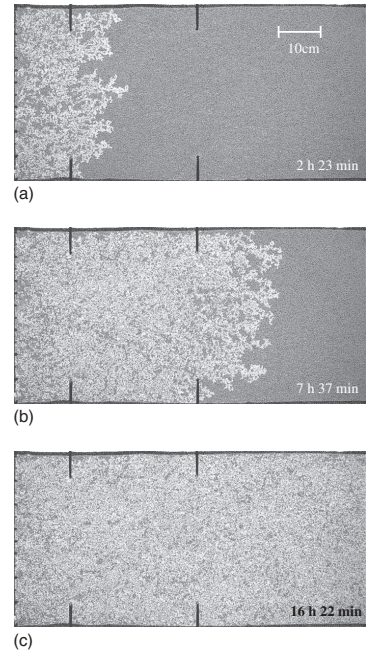

(a)

(b)

(c)

FIG. 3. For the Ca=0.0079 experiment, the system is shown at three different times. Both fluids are injected at left hand side; the outlet is at the right. The upper panel shows a sample in the early transient regime. The water-glycerol mixture is of dark color. This is best seen to the right of the upper panel, where the small bright dots are the solid glass beads. The air is bright white, and glass beads surrounded by air may be indiscernible. The middle panel shows a later stage in the transient. The lower panel shows fully developed steady state.

In Fig. 4 pressure differences over the model are plotted as function of time. Three pressure sensors are used: at the inlet, in the middle of the model, and at the outlet. Even though pressure measurements are local, and measured in the wetting phase, they reflect on average the global pressure development of both phases. If both phases are present along a given cross section transverse to the flow, the pressure along this cross section will only vary by small capillary and viscous fluctuations. Due to the size of our system and the high viscosity of the wetting phase, the measured pressure drop is much larger than these fluctuations. Physically relevant for the motion inside the model is the pressure difference between (i) inlet and outlet and (ii) middle of the model and outlet which, for brevity, are referred to as *inlet* and *middle pressures*. In Fig. 4(a) we can see the signature of a "breakthrough" just before $t \simeq 60$ min in the pressure signals. Here, the apparent linear increase in pressure stops. Shortly after this time the two signals approach a constant level as we reach steady state. In the transient regime the overall pressure behavior at the two sensors appears different. As air enters the model, the inlet pressure starts to increase and it increases linearly until breakthrough, while the
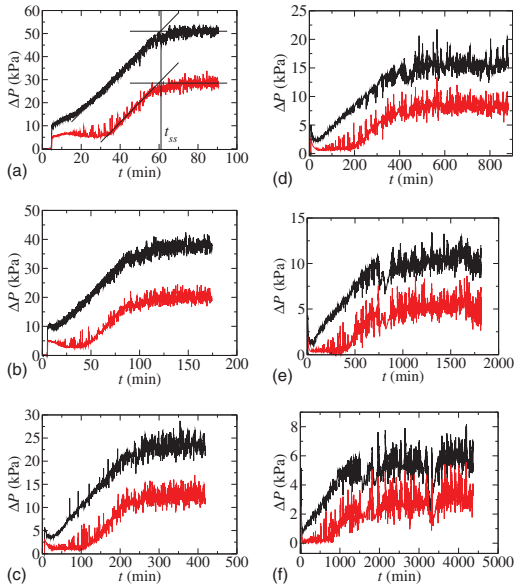
FIG. 4. (Color online) Time evolution of the pressure in each of the six experiments, performed at different injection rate, which is denoted in terms of the capillary numbers (a) Ca=0.17, (b) Ca =0.90, (c) Ca=0.032, (d) Ca=0.015, (e) , and (f) Ca=0.027. The upper black curves are the measured pressure differences between the inlet and the outlet. The lower red (dark gray) curves are the pressure differences between the middle of the model and the outlet. The straight line fit to the pressure curves in (a) shows the determination of the steady-state time t_{ss}, i.e., at which time the system enters into steady state.

middle pressure is constant until the air bubbles reach the sensor ($\sim$30 min). At this point the middle sensor pressure also starts to increase linearly. This is because the average pressure at a point inside the porous medium is controlled by the viscous pressure drop between that point and the outlet channel. Moreover, as air bubbles pass the sensor, the effective permeability of the medium in front of the sensor is lowered. In order to maintain constant flow rate, the pressure has to increase.

In order to learn more about the transient and the transition to steady state, here, we present the results of six experiments performed at different injection rates. The injection rate is controlled by the speed of the step motor used to control the syringe pistons. The rates and the corresponding capillary numbers are given in Table II. We define the capillary number as the ratio between the viscous and the capillary pressure drops over a pore of typical size a,

$$\text{Ca} = \frac{\mu_w Q_w a^2}{\gamma \kappa_0 A} = \frac{\mu_w a^2 v_w}{\gamma \kappa_0}, \quad (1)$$

where $A = Wa$ is the cross-sectional area, $Q_w = 8Q_0$ is total flow rate of the wetting fluid, and v_w is the Darcy velocity of the wetting fluid.

TABLE II. For each of six experiments are given the capillary number, the corresponding flow rate out of a single syringe pump Q_0, the total flow rate $15Q_0$, and the "total invasion flow rate" Q_{tot}^{inv} (see Fig. 14). The difference between $15Q_0$ and Q_{tot}^{inv} is due to compressibility effects as will be discussed in Sec. III D. The capillary number is calculated from Eq. (1).

Ca	Q_0 (ml/min)	$15Q_0$ (ml/min)	Q_{tot}^{inv} (ml/min)
0.17	0.553	8.29	5.73
0.090	0.279	4.18	2.90
0.032	0.114	1.71	1.29
0.015	0.055	0.83	0.67
0.0079	0.023	0.41	0.35
0.0027	0.011	0.16	0.15

A. Transient behavior

A first characteristic time in the transient regime is the elapsed time from onset of invasion until the first breakthrough of nonwetting fluid (air). Recall that the model initially is filled with wetting fluid. We determine this breakthrough time t_b by visual inspection in each experiment. A second characteristic time is when all signs of transient behavior vanish: the steady-state time t_{ss}. To some degree it is possible to see the transition to steady state also by visual inspection. However, as opposed to the breakthrough time, which is sharply defined visually, the steady-state time is not so sharply defined in this way.

In order to quantize the steady-state time, we make use of the measured pressure curves. Figure 4 shows the evolution of the pressure difference between (i) inlet and outlet and (ii) middle point and outlet for each experiment. The pressure saturates and fluctuates around some value at late times in all cases. Prior to saturation there is a period of close to linear increase in the pressure. By making a straight line fit to this slope and flat line fit to the saturated value, we define their crossing point to be the steady-state time t_{ss}, as shown in Fig. 4(a). This definition is sharp and consistent in the sense that this time is the same no matter which of the pressure measurement points (inlet or middle) is used.

The resulting characteristic times versus the capillary number are plotted in Fig. 5. Power-law fits are obtained as shown in the legend. Leaving out details of the process one
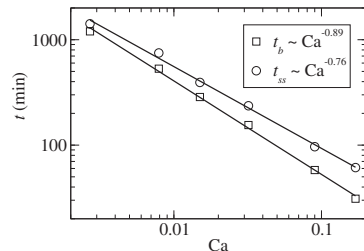

FIG. 5. Measured breakthrough time t_b and steady-state time t_{ss} as a function of the capillary number Ca.
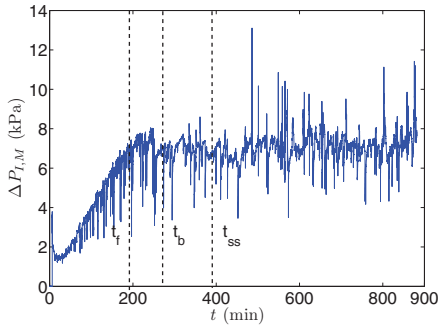
FIG. 6. (Color online) Pressure difference between inlet and middle sensor $\Delta P_{I,M}$ as a function of time t for Ca=0.015. Three characteristic times are indicated by dashed lines; the time at which the front passes the middle sensor t_f, the breakthrough time t_b, and steady-state time t_{ss}.

would expect these times to be proportional to the inverse injection rate. The deviations in the found exponents are small, but nevertheless indicating that there are variations in invasion structure and saturation with Ca.

B. Steady state

In Sec. III A we learned that there exists a well-defined transition to steady state based on analysis of the pressure signal. This is a global criterion, meaning that the system as a whole has reached a steady state. We wish to look at this also on a local scale.

From the onset of invasion a frontal region establishes, containing quite large nonwetting clusters (see Fig. 3). Here, the wetting saturation is somewhat larger than compared to the region behind the frontal region. In addition the region behind the front is more fragmented and homogeneous. We claim that, locally, the region behind the front has already entered into steady state. This is interesting because this happens very early in the process. The region with local steady state grows as the front sweeps through the model. Two arguments support this observation.

First, there is the fact that the pressure monitored by the middle sensor increases linearly from a time t_f right after the front has reached the sensor [see Fig. 4(d)]. This linear increase has the same slope as the inlet sensor pressure until steady state is reached globally (see Fig. 6). For all experiments we find that the pressure difference between the inlet and the middle sensors, $\Delta P_{I,M}(t_f < t < t_{ss})$, during this linear increase is hardly distinguishable from $\Delta P_{I,M}(t > t_{ss})$, as shown in Fig. 6. Since the displacement rate is constant and close to equal both in the transient and the steady states, it follows from Fig. 6 that the relative permeability of the region behind the front must equal that of the later global steady state.

Second, image analyses of parts of the model behind the front in the transient regime as well as in global steady state were performed, yielding similar results for saturation and cluster distribution. This statistical equality and the above
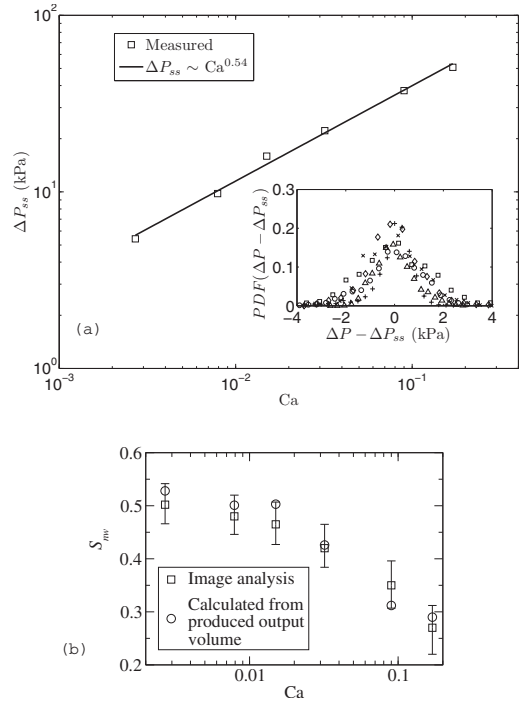

FIG. 7. (a) Average steady-state pressure difference ΔP_{ss} vs capillary number Ca. The solid line is a power-law fit to the measured points giving an exponent $\beta=0.54\pm0.08$. Inset shows the Gaussian-like PDF of $\Delta P(t > t_{ss}) - \Delta P_{ss}$. Note that for all experiments the fluctuations are small and on the order of 1 kPa. (b) The nonwetting saturation S_{nw} as a function of the capillary number Ca.

results demonstrate that the region behind the front is in local steady state.

The global steady state can be quantized by the averaged global pressure drop between the inlet and the outlet,

$$\Delta P_{ss} = \frac{1}{t_{end} - t_{ss}} \int_{t_{ss}}^{t_{end}} \Delta P(t) dt, \qquad (2)$$

where t_{end} is the end time of the experiment and the nonwetting fluid saturation S_{nw} [see Figs. 7(a) and 7(b)].

Experimentally, saturation is not an easily accessible parameter and two approaches have been employed to determine the saturation [see Fig. 7(b)]. A direct method uses the measured amount of wetting fluid that leaves and enters the model. It is in principle a precise method, but it is global. Possible boundary effects, e.g., different saturations near edges or corners, are ignored. Further, image analysis was used by setting a certain grayscale clipping level, as described in Sec. II, and then from the binary image count the amount of wetting fluid.

One observes that the nonwetting saturation decreases with increasing the total injected flow rate. The constraint that the fractional flow is kept constant, a situation for which

little previous results exists, makes it difficult to say whether this is intuitively correct. Numerical studies have sought after relations between saturation and other flow properties [33,34]. However, another factor, to be discussed in Sec. III D, are possible compressibility effects. It is *a priori* not clear that the saturation would be the same if the air were incompressible. This is an issue that we will pursue in further studies.

Figure 7(a) shows the mean steady-state pressure difference ΔP_{ss} as a function of the capillary number Ca. The pressure fluctuations are small as shown in the pressure distributions PDF($\Delta P - \Delta P_{ss}$) in the inset of Fig. 7(a). For all experiments the standard deviation in ΔP_{ss} is on the order of 1 kPa. It is evident that ΔP_{ss} follows a power law in Ca,

$$\Delta P_{ss} \propto Ca^\beta, \tag{3}$$

with the exponent

$$\beta = 0.54 \pm 0.08. \tag{4}$$

This behavior is by no means obvious [36], and we will return to a physical interpretation and quantitative derivation of this result in Sec. III C.

C. Cluster size distributions

After the systems have entered into steady state, we have analyzed images of the structure in order to determine the size distribution of nonwetting clusters or bubbles. The normalized probability density function (PDF) $p(s)$ as a function of cluster size s for all Ca numbers investigated is shown in Fig. 8(a). A trivial observation is the decrease in probability with increasing cluster size. Less obvious is the fact that the curves show an exponential-like cutoff depending on the capillary number. Additionally there is a cutoff region for smaller clusters, as the cluster size approaches the bead size. Since the beads are counted as part of the clusters during image analysis, we have no information at this size scale. For the highest Ca numbers, the whole distribution is dominated by the exponential cutoff. However, as the Ca number is decreased, a small region of power-law-like behavior is observed in between the two cutoffs.

Analogously to what is done in percolation theory [37], we assume that the distribution of the clusters follows the PDF,

$$p(s) \propto s^{-\tau} \exp(-s/s^*), \tag{5}$$

where s^* is the cutoff cluster size. The latter function has been fitted, using a proportionality constant τ and s^* as fit parameters, to the experimental data for each Ca number. This is shown by the solid lines in Fig. 8(a). By averaging the fitted τ exponents it is found that $\tau = 2.07 \pm 0.18$. The uncertainty only reflects the difference in fitted exponents. From the distributions it is seen that no power-law region is well pronounced, and we do not claim that τ is determined with a large degree of certainty in this case. When it comes to the cutoff cluster size, the fitted values of s^* are found to scale with Ca [Eq. (1)] as
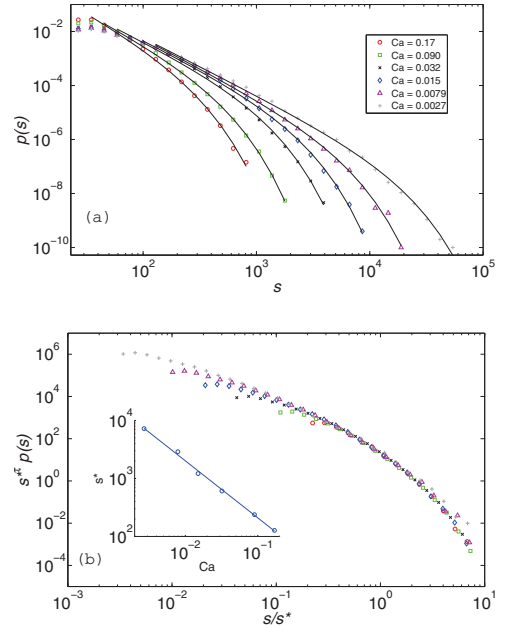

FIG. 8. (Color online) Nonwetting cluster size PDF $p(s)$ in steady state for all experiments. The cluster size s is measured in pixels; 1 pixel = 0.037 mm². (a) Normalized probability distributions. The dominating cutoff behavior is evident. The solid lines represent fits of Eq. (5). (b) The horizontal and the vertical axes are rescaled with $1/s^*$ and $s^{*\tau}$, respectively, to obtain the data collapse. The Ca dependence of the cutoff cluster size s^* is shown in the inset.

$$s^* \propto Ca^{-\zeta}, \tag{6}$$

where $\zeta = 0.98 \pm 0.07$. This is shown in the inset of Fig. 8(b). One should note, even for the lowest Ca number, that $s^* \sim 10^5$ pixels is considerably smaller than the system size $\sim 10^7$ pixels, meaning that large-scale finite-size effects should not be of importance. Equation (5) predicts a rescaling of the horizontal and the vertical axes with $1/s^*$ and $s^{*\tau}$, respectively. On this basis the data collapse in Fig. 8(b) is obtained.

From the above considerations, the cluster size PDF of nonwetting clusters in steady state obeys the scaling function

$$p(s) \propto s^{*-\tau} H(s/s^*), \tag{7}$$

where $H(x)$ contains an exponential cutoff [Eq. (5)], so that $p(s) \rightarrow 0$ when $x \gg 1$.

Up to now the cluster size measured in area was studied. One step further is to consider the linear extension of the clusters in the two directions: l_x transverse to the overall direction of flow and l_y oriented along the overall direction of flow. This is achieved by assigning a bounding box of sides l_x and l_y to a cluster of size s, i.e., the smallest rectangle that can contain the cluster. In the following, l_i, where $i \in \{x, y\}$, will denote both the l_x and the l_y extensions. It is
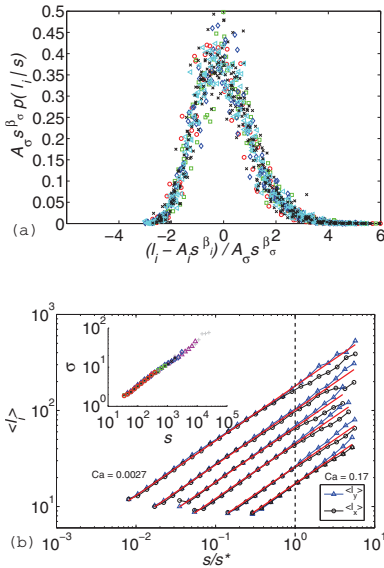
(a)

(b)

FIG. 9. (Color online) The extension lengths l_i are measured in pixel units; 1 pixel=0.19 mm. (a) Data collapse of multiple $p(l_i|s)$ PDFs, where $i \in \{x, y\}$. The s values are picked from all experiments and ranges over four decades. The collapse is obtained by a rescaling predicted by the Gaussian distribution function. (b) Scaling of $\langle l_y \rangle$ and $\langle l_x \rangle$ with s for all Ca numbers. The horizontal axis has been rescaled with $1/s^*$ to emphasize that Eq. (9), represented by the solid red (dark gray) lines, shows deviations for $s > s^*$. The inset shows the scaling of σ with s, [Eq. (8)].

found that the PDF of l_i for a given cluster size s, $p(l_i|s)$, is a Gaussian. Additionally, for $s \leq s^*$, the corresponding standard deviation σ and mean $\langle l_i \rangle$ of $p(l_i|s)$ scale with the cluster size as

$$\sigma = A_\sigma s^{\beta_\sigma}, \tag{8}$$

$$\langle l_i \rangle = A_i s^{\beta_i}, \tag{9}$$

with prefactors $A_\sigma = 0.25$ and $A_i = 1.12$, where $\beta_\sigma = 0.55 \pm 0.06$ and $\beta_i = 0.57 \pm 0.05$. Within the limits of uncertainty, β_σ and β_i can be considered equal. The corresponding prefactors yield

$$\sigma/\langle l_i \rangle \approx 0.22, \tag{10}$$

meaning that the standard deviation is roughly 22% of the mean extension length.

The collapse of multiple $p(l_i|s)$ PDFs of different cluster sizes and Ca numbers and the scaling of Eqs. (8) and (9) are shown in Figs. 9(a) and 9(b), respectively. Figure 9(a) reveals a strong correlation between cluster size and linear extension, and we believe that the use of bounding boxes to characterize the clusters is justified. It is evident from Fig. 9(b) that the scaling of $\langle l_x \rangle$ and $\langle l_y \rangle$ is equal for $s \leq s^*$, a point to which we will return shortly. However, at this stage we note that the cutoff cluster size s^* corresponds to a cutoff
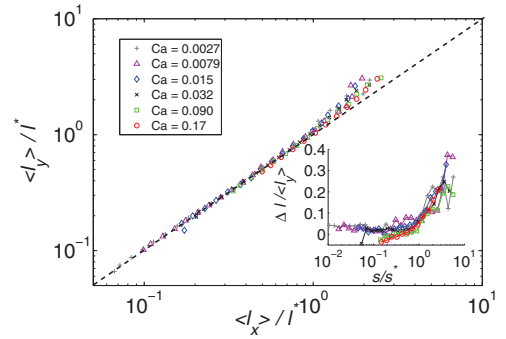

FIG. 10. (Color online) Average extension length $\langle l_x \rangle$ vs $\langle l_y \rangle$, with both axes rescaled with the cutoff length l^*. Clusters are not elongated, on the average, until l^* is reached. The inset shows the relative length difference $\Delta l/\langle l_y \rangle$ as a function of s/s^*, where $\Delta l = \langle l_y \rangle - \langle l_x \rangle$. $\Delta l/\langle l_y \rangle$ increases significantly when s^* is reached.

extension length l^*. From Eqs. (6) and (9) it follows that

$$l^* = A_i s^{*\beta_i} \propto Ca^{-\zeta\beta_i}. \tag{11}$$

The similar scaling of $\langle l_i \rangle$ for $s \leq s^*$ means that nonwetting clusters fit into quadratic bounding boxes on the average and can thus be considered isotropic at these sizes. This is seen from Fig. 10 where $\langle l_x \rangle$ is plotted vs $\langle l_y \rangle$, both rescaled with the cutoff extension length l^*. It is evident that the average bounding box for $\langle l_i \rangle \leq l^*$ is quadratic, and furthermore this behavior is independent of Ca. When $\langle l_i \rangle$ reaches l^*, equivalent to the cluster size reaching s^*, there is a crossover and the clusters are seen to be somewhat elongated in the direction of flow on the average. Cluster elongation or anisotropy is best emphasized by considering the average relative length difference $\Delta l/\langle l_y \rangle$, where $\Delta l = \langle l_y \rangle - \langle l_x \rangle$. The inset of Fig. 10 shows, for six Ca numbers, the relative length difference for all cluster sizes. Each curve is characterized by a region where the relative length difference is constant or only slowly increasing, always less than 5%. As the cutoff cluster size s^* is reached, $\Delta l/\langle l_y \rangle$ increases significantly. Specifically, the largest sustainable clusters are roughly 30% longer in the direction of flow than transverse to the direction of flow.

To understand elongation, one has to consider how the capillary pressure at the cluster perimeter is affected by a surrounding viscous pressure field. In mechanical equilibrium, the surface pressure $P_{nw} - P_w$ equals the capillary pressure P_{cap}

$$P_{nw} - P_w = P_{cap} = \gamma\left(\frac{1}{R_1} + \frac{1}{R_2}\right), \tag{12}$$

where R_1 and R_2 are the radii of curvature in the well-known *Young-Laplace* law. The wetting fluid pressure difference ΔP_w over a cluster of length l_y can be approximated as

$$\Delta P_w \approx \frac{\Delta P_{ss}}{L} l_y, \qquad (13)$$

whereas the nonwetting fluid pressure P_{nw} is constant inside the cluster. The capillary pressure over the interface of the cluster will thus decrease in a direction opposite to that of the overall flow, highest at the tip and lowest at the tail of the cluster. As we shall see, this introduces anisotropy which will depend on the crossover length l^*.

In the case of steady-state simultaneous flow, the dynamics of nonwetting clusters are influenced by a competition of *both* drainage and imbibition processes. A pore is drained or imbibed when the capillary pressure is above or below the capillary threshold pressure for drainage P_c^D or imbibition P_c^I, respectively. Due to the randomness in the local geometry of the porous medium, P_c^D and P_c^I are not fixed values. As discussed by Auradou *et al.* [38], they will vary independently from pore to pore according to their respective distribution function. Furthermore, these distributions are isotropic.

Clusters of length $l_y < l^*$ are observed from experiments to migrate only small distances in the porous matrix. Usually they get trapped and can only be remobilized by coalescing with larger migrating clusters. Migration is the process where drainage is followed by imbibition, so that a cluster moves without changing its volume. The viscous pressure field sets a length scale, below which the local geometry dominates the choice of flow path. Above this length scale, growth near the advancing tip and retraction near the receding tail are favored due to the now significant capillary pressure difference between the cluster tip and tail.

As we have seen, clusters cannot grow infinitely large. It is the occurrence of snap-offs [38] of the cluster tail, caused by imbibition, that will determine the l_y extension. The probability of a cluster snap-off will mainly depend on (1) the difference between the average capillary pressure threshold for drainage and imbibition $\bar{P}_t = \bar{P}_c^D - \bar{P}_c^I$ and (2) the capillary pressure difference $\Delta P_{cap} = P_{cap,tip} - P_{cap,tail}$ [see Eq. (12)] between the advancing tip and receding tail of a cluster. Further, snap-offs will typically occur when

$$\Delta P_{cap} > \bar{P}_t. \qquad (14)$$

Using Eqs. (12) and (13) we obtain the following crossover length scale from Eq. (14):

$$\frac{\Delta P_{ss}}{L} l^* = \bar{P}_t, \qquad (15)$$

$$l^* = \bar{P}_t L \frac{1}{\Delta P_{ss}}. \qquad (16)$$

Equation (16) predicts a cutoff length l^*, inversely proportional to ΔP_{ss}, over which clusters can stay connected. At this point an important observation is made; inserting Eq. (3) into Eq. (16), we see that the cutoff length l^* scales with the Ca number as in Eq. (11), provided $\beta = \zeta \beta_i$. All of the latter exponents have uncertainty, which within we can make the reasonable claim that they are equal, and thus that our findings are consistent with
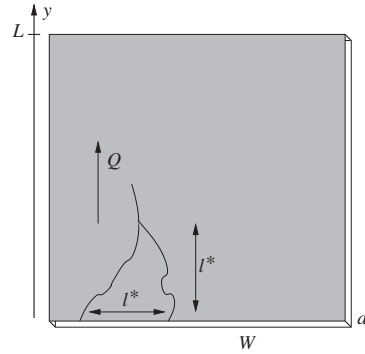

FIG. 11. A conceptual sketch of the assumed channel system. Channels of the wetting fluid, of a characteristic width that coincides with the pore width, are separated by a distance l^*. Q indicates the average direction of flow.

$$l^* \propto \frac{L}{\Delta P_{ss}}. \qquad (17)$$

To sum up, we claim that Eq. (17) controls the onset of (1) cluster elongation or anisotropy as seen in Fig. 10, (2) snap-offs and the size of the largest sustainable clusters as seen in Fig. 8, and (3) cluster mobilization.

The scaling relation between ΔP_{ss} and Ca [Eq. (3)] can be derived by the following argument of dissipation balance [36]. Since the average interface area of the system will remain constant in steady state, all the power that is put into the system goes into viscous dissipation. This dissipation will then take place in the high viscous wetting fluid. The flow pattern of the wetting fluid is best described as an interchanging network in between the air clusters, containing larger islands connected by narrow channels on the order of a pore size wide. It is reasonable to assume that the majority of viscous dissipation will take place in the narrow channels, since the local flow velocity is much higher here. In this respect it is also important to remember that the permeability for the most part is set by the narrowest parts of the fastest flow path through the medium. Islands of wetting fluid do not contribute as much.

Careful visual observation indicates that the width of the channels are typically one or a few pore widths, while the spacing between these channels must be the characteristic cluster length l^*. This conceptual picture is illustrated in Fig. 11. Thus, the volume in which the dissipation happens is then assumed to be the volume of these channels and will be denoted as V_{dis}. We may then write the following proportionality for V_{dis}:

$$V_{dis} \propto \text{number of channels} = \frac{W}{l^*} \propto \Delta P_{ss}, \qquad (18)$$

where the last proportionality follows from Eq. (17). On the other hand, the total work per unit time which is done by the pressure drop across the system must equal the internal dissipation D, so that

$$15Q_0 \Delta P_{ss} = D \propto V_{dis} u^2, \tag{19}$$

where u is the average flow velocity of the wetting fluid and D is the integral over V_{dis} of $u|\nabla P|$. Furthermore, the pressure gradient $|\nabla P| \propto u$ thanks to Darcy's law. The flow velocity u is set by the volume flux as

$$u \propto \frac{Q_w}{V_{dis}} \propto \frac{Q_w}{\Delta P_{ss}} \tag{20}$$

by the use of Eq. (18). Upon insertion of u in Eq. (19) we may write in terms of the Ca number (Ca $\propto Q_w \propto Q_0$)

$$\Delta P_{ss} \propto \sqrt{\text{Ca}}, \tag{21}$$

which is the scaling relation we set out to prove. Darcy's law allows us to write things in terms of a Ca-dependent effective permeability $\kappa(\text{Ca})$. Since Darcy's law takes the form

$$Q_w = \frac{\kappa}{\mu_w} \frac{\Delta P_{ss}}{L}, \tag{22}$$

we immediately obtain

$$\kappa \propto \sqrt{\text{Ca}}. \tag{23}$$

We have already discussed the normalized PDF of nonwetting clusters, $p(s)$, which was shown to obey a scaling law in the cutoff cluster size s^* [Eq. (7)], and thus also in the capillary number Ca [Eq. (6)]. We now turn to a discussion of the PDF of l_i for all s, namely, the marginal PDF $p(l_i)$. Since there is no *one-to-one* correspondence between l_i and s, no exact analytical solution of $p(l_i)$ can be obtained from Eq. (5). However, $p(l_i|s)$ is Gaussian [Fig. 9(a)] and narrowly peaked around $\langle l_i \rangle$ [Eq. (10)]. On this basis we would expect $p(l_i)$ to have similarities with the PDF

$$g(l) = p(s) \frac{ds}{dl}, \tag{24}$$

$$g(l) \propto l^{-\phi} \exp\left[-\left(\frac{l}{l^*} \right)^{1/\beta_i} \right], \tag{25}$$

where

$$\phi = \frac{\tau + \beta_i - 1}{\beta_i} \approx 2.9. \tag{26}$$

The function $g(l)$ is thus the PDF obtained when assuming that Eq. (9) applies for all l_i.

The PDFs $p(l_y)$ and $p(l_x)$ are plotted in Fig. 12(a), and it is evident that a cutoff behavior is dominant, similar to what is found for $p(s)$. Furthermore, for the largest extension lengths, the probability density $p(l_y)$ is larger than $p(l_x)$ for all the Ca numbers. This is intrinsically linked to the fact that large clusters are elongated in the direction of flow as discussed previously. We have already argued that there exists a cutoff length l^* common for both l_i directions. The observed difference between $p(l_x)$ and $p(l_y)$ is thus due to different cutoff behaviors in these PDFs as a consequence of elongation.

On the basis of Eq. (25) a rescaling of the form $l^{*\phi}p(l_i)$ vs l_i/l^* is predicted. The corresponding data collapse is shown
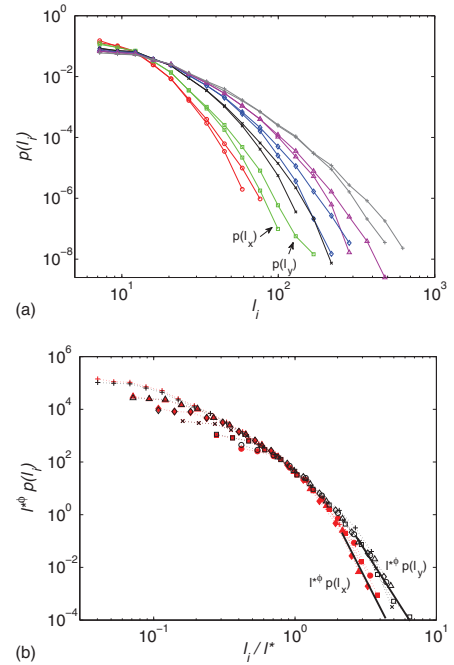

FIG. 12. (Color online) (a) Plot of the linear extension PDF $p(l_x)$ and $p(l_y)$ for various Ca numbers (similar symbol encoding as in Fig. 10). (b) shows a data collapse, predicted by Eq. (25), of the same curves. The red (dark gray) filled and black empty markers represent l_x and l_y, respectively. The exponent ϕ is taken as the value that gives the best collapse, and it is found that $\phi = 2.8 \pm 0.3$. Solid black lines indicate the difference in cutoff function of $p(l_x)$ and $p(l_y)$.

in Fig. 12(b). The exponent ϕ is in this case taken as the value giving the best collapse, and it is found that $\phi = 2.8 \pm 0.3$, in agreement with Eq. (26). Again there is a crossover as the extension length approaches the pore scale, but above this scale the collapse is most satisfactory. The small difference in the cutoff function, as discussed above, is indicated by the two solid lines in Fig. 12(b). Analog to Eq. (7), $p(l_i)$ obeys the scaling function

$$p(l_i) \propto l^{*-\phi} G_i(l_i/l^*), \tag{27}$$

for clusters above the lower cutoff scale.

The imposed nonwetting flow rate during steady state $Q_{nw} = 7Q_0$ must on average equal the flux of nonwetting clusters inside the model. As shown in [36], this gives a normalization condition that can be used to obtain the value of the scaling exponent ϕ, in Eq. (27),

$$Q_{nw} = \frac{aN}{L} \int_a^\infty dl \, l^2 U(l) p(l), \tag{28}$$

where we have skipped subindices. Here, N denotes the total number of clusters. Below we show that this number de-
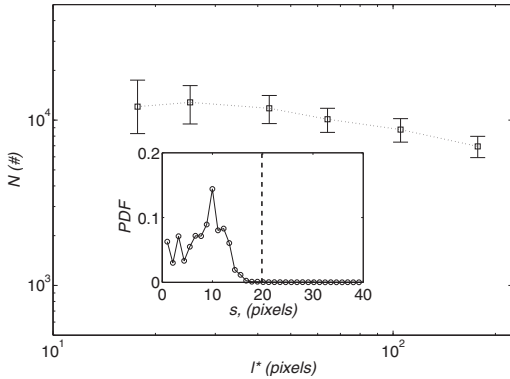
FIG. 13. Total number of clusters N in the system of area $A = L \times W$ as a function of the crossover length l^*. The upper and the lower limits of the error bars correspond to a chosen threshold of $s = 14$ and $s = 30$, respectively. Inset shows the size PDF of glass beads. A threshold of $s = 20$ pixels ensures that no glass-bead "clusters" are included in N.

pends only very weakly on the flow rate. $U(l)$ denotes the average center of mass velocity of a cluster of extent l. This function is assumed to be linear in Q_{nw} and to depend only on some function $f(l/l^*)$. As a first approximation one could take $f(l/l^*) \propto \Theta(l/l^* - 1)$, where $\Theta(x)$ is the usual Lorentz-Heaviside step function, since small clusters usually are immobile,

$$U(l) = \frac{Q_{nw}}{A} f(l/l^*). \tag{29}$$

By insertion of the distribution of l_i in Eq. (27) and applying the substitution $x = l/l^*$, Eq. (28) gives

$$1 = l^{*(3-\phi)} \frac{aN}{V} \int_{a/l^*}^{\infty} x^2 f(x) G_t(x) dx, \tag{30}$$

where the integrand converges in both limits. In particular, the lower limit corresponds to immobile clusters where $U(l) = 0$. If the total number of clusters N is constant with respect to l^* or Ca, we obtain immediately $\phi = 3$. This is consistent with our experimental findings. We wish however to elaborate somewhat on the influence of N on the exponent ϕ, as measurements of N is found to have a weak, at most logarithmic, dependence of l^*. In counting the number of clusters, there is an experimental technicality that needs to be addressed. In the black and white images used in the cluster analysis, both the glass beads that constitute the porous medium and regions of air show up as white pixels. This means that there is a size distribution of bead "clusters" that should be disregarded from the real air cluster size distribution. Analyzing background images, i.e., images of the porous matrix filled with the black wetting fluid only, it is found that the distribution of glass beads does not exceed a size of $s = 20$ pixels as shown in the inset of Fig. 13. Thus, in obtaining N we use $s = 20$ pixels as a lower threshold for a cluster to be counted. However, clusters of all sizes contain pixels
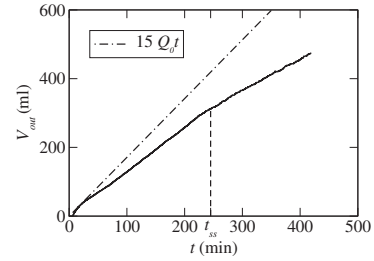

FIG. 14. The solid line is the measured accumulated outflow of the wetting phase since the start of the experiment. After the steady-state time t_{ss} the slope of this curve equals $8 \times Q_0$ as one should expect since this is the injection rate of the wetting phase. However, for $t < t_{ss}$ the pressure increases in the model, thus compressing air, and therefore the outflow of wetting fluid Q_{tot}^{inv} is less than $15 \times Q_0$ which one would expect in the case of incompressible fluids.

from both glass beads and air. As a consequence, when we are above the typical bead size, a constant size fraction is added to the original cluster size and it does not affect the analysis in any way. When clusters approach the average size of a glass bead, somewhat below the threshold, the extracted area is largely dominated by the glass bead and we have little information at this scale. This small-scale effect is most dominant in high Ca-number experiments, as air clusters are smaller here (low l^* values). In this case, the value of N will be underestimated, since there are actual air clusters smaller than the chosen glass bead threshold.

Figure 13 shows a weak decreasing trend in the number of clusters N as a function of l^*, with error bars corresponding to glass bead cluster thresholds $s = \{14, 30\}$ pixels. As a matter of convenience, we quantify this dependence through a power law and we find an exponent of -0.25 ± 0.10 between N and l^*. Accounting for this dependence in Eq. (30), the exponent ϕ is reduced and we obtain $\phi = 2.75$, corresponding well with the experimental value. Using this ϕ we obtain through Eq. (26) an exponent $\tau \approx 2$ for the cluster size PDF. This is also in good agreement with the found experimental value.

D. Compressibility effects

In addition to the pressure, we record the volume of wetting fluid flowing out of the model, V_{out}. This is shown in Fig. 14 for the Ca = 0.032 experiment. If the fluids were incompressible, the total outflow would equal the total inflow, i.e., $15Q_0$, until the first nonwetting fluid is produced. For $t < t_{ss}$ we define the total invasion flow rate as $Q_{tot}^{inv} = dV_{out}/dt$. One observes that this slope is smaller than $15Q_0$, which is caused by air compression as the pressure increases. For each experiment this slope is found to be roughly constant, with values listed in Table II. As steady state is reached, i.e., $t \geq t_{ss}$, we expect a total flow rate of $Q_{tot} \equiv 15Q_0$. At this point the pressures are relaxed at a constant average value, and the air is not compressed any further, meaning that a flow rate of Q_0 is obtained from all seven air-filled syringes.

As an example, for Ca=0.17 the inlet and the outlet pressures during steady state are ~55 and ~5 kPa, respectively. This gives a pressure difference of ~50 kPa as seen in Fig. 4(a). This means that air entering the model has a compressed volume of roughly ~2/3 relative to the volume at the outlet. The question is to what extent air compressibility affects the flow dynamics and structure, i.e., compared to the flow of two incompressible fluids.

We claim that most of the expansion of compressed air happens during short time intervals through "avalanches" in the porous medium. In the following a qualitative description will be given. This phenomenon is a study in its own respect, and a quantitative analysis is beyond the scope of this paper. From visual inspection it is observed that air is frequently blocked out by the local configuration of wetting fluid around one or more of the air inlet nodes. This causes further compression and thereby a pressure increase in the air tubes. As the pressure continues to increase, the air is seen to slowly displace the blocking wetting fluid. At some point an avalanche of expanding air is triggered and the air and inlet pressure drop abruptly. The avalanche is characterized by channels, not more than a pore size wide, created between existing nonwetting clusters. The temporarily existing nonwetting cluster is narrow in the l_x direction but spans the air invaded region in the l_y direction. This means that an avalanche cluster reaches from the originating inlet node to either the displacement front or all the way through the model, dependent on whether the system is in the transient or in the steady state, respectively. During an avalanche in the transient state, air is seen to propagate rapidly to the displacement front where it expands surrounded only by the wetting fluid. This rapid propagation of expanding air is also seen in steady state but the air is now immediately transported to the model outlet. The time scale of an avalanche is on the order of ~1 s. During this time, a signature of the avalanche is seen as a spike in the pressure signal from the middle and the outlet pressure sensors. As the pressure inside the avalanche cluster relaxes, the interconnecting channels are imbibed by the surrounding wetting fluid and the displacement now returns to "normal." Being a highly dynamical phenomenon, the flow of expanding air in avalanches is visually striking. Figure 15 shows an avalanche through the central part of the model, also compared to normal displacement during the same time interval.

It is not trivial to obtain the details of how the flow dynamics is affected by compressibility of the nonwetting fluid. It is clear that the avalanches occurring on small time scales are solely an effect of compressibility. However we believe that the results of our statistical analysis of clusters would be the same as in the incompressible case. Mainly there are two arguments supporting this. (1) From the above description of avalanches it is natural to assume that most of the compressed air volume inside clusters is released during an avalanche. Hence in between avalanches, the normal motion, breakup, stranding and coalescing of clusters would be as in the incompressible case. (2) Intuitively one might imagine that compressible clusters would expand and grow larger when moving toward lower pressure at the outlet, thus giving a position dependence of the cluster PDF and saturation. This is however not the case as shown in Fig. 16, where the dis-
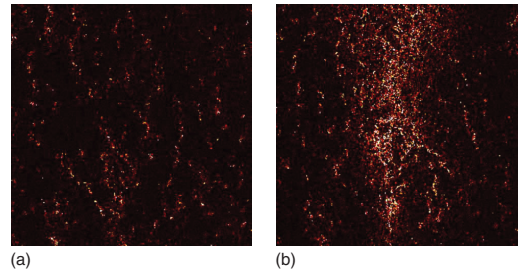

(a)   (b)

FIG. 15. (Color online) A central region of the model, (17 × 17) cm consisting of ~10^4 pores, is captured with a fast camera during steady state (Ca=0.090). Flow direction is from top to bottom. By subtracting two images of the displacement structure, separated in time by $\Delta t \sim 1$ s, pores imbibed or drained (bright regions) during this time can be distinguished from pores of unchanged fluid configuration (dark regions). (a) Normal displacement. Pore fluid configurations are close to unchanged during Δt. (b) Avalanche through the same region as depicted in (a). In this case the fluid configurations are drastically changed in a narrow central part of the image during Δt as the avalanche passes through. This is the signature of air expanding rapidly through the region.

tribution of clusters from two different regions of the model are compared and found to be identical. Thus, the saturation and the distribution of clusters are homogeneous throughout the model, as expected for an incompressible system. This can be explained by recalling the importance of the viscous pressure drop in the wetting fluid, which in essence determines the size of nonwetting clusters through the cutoff length or size, as argued previously. Either if clusters expand due to compressibility or, e.g., because two smaller clusters coalesce to make one big cluster, snap-off will occur at the cutoff size regardless of the origin of growth.

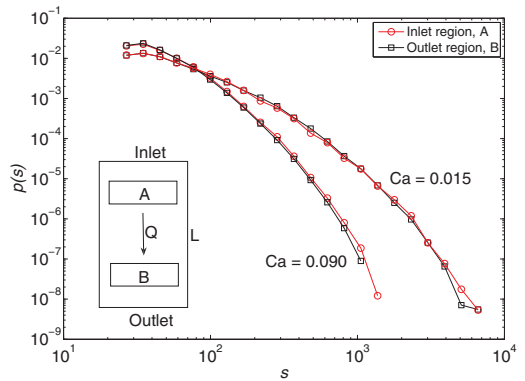FIG. 16. (Color online) Cluster size PDF $p(s)$, for Ca=0.090 and Ca=0.015. For each Ca number a region A close to the inlet and region B close to the outlet has been considered, as shown in the inset sketch. It is evident that the clusters are distributed equally in the direction of flow and not affected by air compressibility. This behavior is found to apply for all Ca numbers considered in the experiments.

IV. CONCLUSION

Simultaneous two-phase flow in porous media has been studied experimentally, in a large quasi-two-dimensional laboratory model of roughly $\sim 10^5$ pores. We use a gas-liquid phase pair, resulting in a low viscosity ratio $M \sim 10^{-4}$. Both the transient and the steady states of this system have been considered.

The mixed displacement structure of wetting and nonwetting fluids is more complex than what is found in the transient regimes of, e.g., capillary or viscous fingering. Due to the simultaneous flow of high viscous wetting fluid, clusters of low viscous nonwetting fluid will be snapped off from the inlet nodes. The competition of both drainage and imbibition causes fragmentation of the nonwetting fluid, and the dynamics is characterized by the movement and mixing of discreet nonwetting clusters in a background field of wetting fluid. Initially, the fragmentation and the mixing of fluids increase, but are seen to stabilize when the most advanced parts of the front have reached roughly halfway through the model. At this point the invasion structure consists of a heterogeneous region at the front and a homogeneous region further behind, locally in steady state, similar to that of later global steady state. It is an important result, because this kind of similarity between transient and steady regimes is far from obvious.

The probability distribution of the size of nonwetting clusters exhibits a clear cutoff for all Ca numbers investigated during steady state. No clear power-law behavior is found, however, for larger clusters reasonable fits are obtained to Eq. (5). We find $\tau \approx 2$ and that the cutoff cluster size s^* is inversely proportional to the capillary number. Additionally a scaling relation is found between the mean extension length $\langle l_i \rangle$ and $s \leq s^*$, equal in both directions with the exponent $\beta_i \approx 0.57$. Clusters at these sizes are thus isotropic. Clusters above s^* are elongated in the direction of flow due to the anisotropic influence of the viscous pressure field. From these scaling relations we demonstrate experimentally and theoretically the important result that both $1/l^*$ and ΔP_{ss} scale approximately as the square root of the Ca number.

The observed avalanche behavior, occurring in the compressible nonwetting phase, is an interesting phenomenon that we have not explored fully in this work. To the best of our knowledge, this kind of dynamics in a gas-liquid system in porous media has not previously been reported. To characterize and obtain a better understanding of these dynamical events is certainly something worthy to pursue.

In a recent paper by Ramstad and Hansen [35], cluster size distributions during steady-state two-phase flow in a porous medium was studied numerically for $M=1$, i.e., viscosity match of the fluid pair. They found that below a critical value of the nonwetting fluid saturation, the nonwetting cluster size distribution was dominated by a cutoff behavior similar to what have been presented here. Above the critical saturation value, power-law behavior was observed. Due to the large difference in viscosity contrast between our experiments and these simulations, no direct comparison can be made. Nevertheless, it would be interesting to perform future experiments with the intention of exploring such a critical value.

Despite the variety of findings in this study, only a small part of the parameter space was explored. Our theoretical predictions should be used as a starting point of incorporating the more complex case of, e.g., viscosity matched fluids. Thus, we would like in the future to consider experiments where the two phases has more similar viscosities and also the possibility of tuning the wetting and the nonwetting fluid flow rates independently. At the present time, preliminary results indicate that the flow dynamics show no strong dependence of the latter flow parameter. Finally, the question of any history dependence of the global steady state is important. It is not obvious that the system will reorganize itself to a unique steady-state structure independent on initial transients. However, a preliminary steady-state experiment, initially at Ca=0.0027 and then increased to Ca=0.032, shows that the structure organizes into a statistically identical structure as in an ordinary Ca=0.032 experiment.

[1] J. Bear, *Dynamics of Fluids in Porous Media* (American Elsevier Publishing Company, New York, 1972).

[2] F. A. L. Dullien, *Porous Media Fluid Transport and Pore Structure*, 2nd ed. (Academic Press, Inc., San Diego, 1992).

[3] M. Sahimi, *Flow and Transport in Porous Media and Fractured Rock* (VCH Verlagsgesellschaft mbH, Weinheim, 1995).

[4] M. Sahimi, Rev. Mod. Phys. **65**, 1393 (1993).

[5] R. Lenormand, E. Touboul, and C. Zarcone, J. Fluid Mech. **189**, 165 (1988).

[6] R. Lenormand and C. Zarcone, Transp. Porous Media **4**, 599 (1989).

[7] P. G. Saffman and G. Taylor, Proc. R. Soc. London, Ser. A **245**, 312 (1958).

[8] R. Lenormand, C. Zarcone, and A. Sarr, J. Fluid Mech. **135**, 337 (1983).

[9] R. Lenormand, J. Phys.: Condens. Matter **2**, SA79 (1990).

[10] R. Lenormand and C. Zarcone, Phys. Rev. Lett. **54**, 2226 (1985).

[11] D. Wilkinson and J. F. Willemsen, J. Phys. A **16**, 3365 (1983).

[12] L. Paterson, Phys. Rev. Lett. **52**, 1621 (1984).

[13] K. J. Måløy, J. Feder, and T. Jøssang, Phys. Rev. Lett. **55**, 2688 (1985).

[14] J. P. Stokes, D. A. Weitz, J. P. Gollub, A. Dougherty, M. O. Robbins, P. M. Chaikin, and H. M. Lindsay, Phys. Rev. Lett. **57**, 1718 (1986).

[15] D. A. Weitz, J. P. Stokes, R. C. Ball, and A. P. Kushnick, Phys.

Rev. Lett. **59**, 2967 (1987).

[16] Grunde Løvoll, Yves Meheust, Renaud Toussaint, Jean Schmittbuhl, and Knut Jorgen Måløy, Phys. Rev. E **70**, 026301 (2004).

[17] O. I. Frette, K. J. Måløy, J. Schmittbuhl, and A. Hansen, Phys. Rev. E **55**, 2969 (1997).

[18] Y. Meheust, G. Løvoll, K. J. Måløy, and J. Schmittbuhl, Phys. Rev. E **66**, 051603 (2002).

[19] C. D. Tsakiroglou, M. A. Theodoropoulou, and V. Karoutsos, AIChE J. **49**, 2472 (2003).

[20] C. D. Tsakiroglou, M. A. Theodoropoulou, V. Karoutsos, D. Papanicolaou, and V. Sygouni, J. Colloid Interface Sci. **267**, 217 (2003).

[21] C. D. Tsakiroglou, M. A. Theodoropoulou, V. Karoutsos, and D. Papanicolaou, Water Resour. Res. **41**, W02014 (2005).

[22] M. A. Theodoropoulou, V. Sygouni, V. Karoutsos, and C. D. Tsakiroglou, Int. J. Multiphase Flow **31**, 1155 (2005).

[23] D. G. Avraam and A. C. Payatakes, J. Fluid Mech. **293**, 207 (1995).

[24] D. G. Avraam and A. C. Payatakes, Transp. Porous Media **20**, 135 (1995).

[25] C. D. Tsakiroglou, D. G. Avraam, and A. C. Payatakes, Adv. Water Resour. **30**, 1981 (2007).

[26] G. N. Constantinides and A. C. Payatakes, J. Colloid Interface Sci. **141**, 486 (1991).

[27] G. N. Constantinides and A. C. Payatakes, AIChE J. **42**, 369 (1996).

[28] M. S. Valavanides, G. N. Constantinides, and A. C. Payatakes, Transp. Porous Media **30**, 267 (1998).

[29] D. G. Avraam and A. C. Payatakes, Ind. Eng. Chem. Res. **38**, 778 (1999).

[30] M. S. Valavanides and A. C. Payatakes, Adv. Water Resour. **24**, 385 (2001).

[31] A. Vedvik, G. Wagner, U. Oxaal, J. Feder, P. Meakin, and T. Jøssang, Phys. Rev. Lett. **80**, 3065 (1998).

[32] H. A. Knudsen, E. Aker, and A. Hansen, Transp. Porous Media **47**, 99 (2002).

[33] H. A. Knudsen and A. Hansen, Phys. Rev. E **65**, 056310 (2002).

[34] H. A. Knudsen and A. Hansen, EPL **65**, 200 (2004).

[35] T. Ramstad and A. Hansen, Phys. Rev. E **73**, 026306 (2006).

[36] A. C. Payatakes, Annu. Rev. Fluid Mech. **14**, 365 (1982).

[37] D. Stauffer and A. Aharony, *Introduction to Percolation Theory* (Taylor & Francis, London, 1992).

[38] H. Auradou, K. J. Måløy, J. Schmittbuhl, and A. Hansen, Transp. Porous Media **50**, 267 (2003).

[39] K. T. Tallakstad, H. A. Knudsen, T. Ramstad, G. Løvoll, K. J. Måløy, R. Toussaint, and E. G. Flekkøy, Phys. Rev. Lett. **102**, 074502 (2009).

III

Local Dynamics of a Randomly Pinned Crack Front during Creep and Forced Propagation: An Experimental Study

Ken Tore Tallakstad,[1] Renaud Toussaint,[2] Stephane Santucci,[3] Jean Schmittbuhl,[2] and Knut Jørgen Måløy[1]

[1]*Department of Physics, University of Oslo, PB 1048 Blindern, NO-0316 Oslo, Norway*
[2]*Institut de Physique du Globe de Strasbourg, UMR 7516 CNRS,*
Université de Strasbourg, 5 rue René Descartes, F-67084 Strasbourg Cedex, France
[3]*Laboratoire de Physique, Ecole Normale Suprieure de Lyon,*
CNRS UMR 5672, 46 Alle d'Italie, 69364 Lyon cedex 07, France
(ΩDated: September 8, 2010)

We have studied the propagation of a crack front along the heterogeneous weak plane of a transparent PMMA block using two different loading conditions: imposed constant velocity and creep relaxation. We have focused on the intermittent local dynamics of the fracture front, for a wide range of average crack front propagation velocities spanning over four decades. We computed the local velocity fluctuations along the fracture front. Two regimes are emphasized: a de-pinning regime of high velocity clusters defined as avalanches and a pinning regime of very low velocity creeping lines. The scaling properties of the avalanches and pinning lines (size and spatial extent) are found to be independent of the loading conditions and of the average crack front velocity. The distribution of local fluctuations of the crack front velocity are related to the observed avalanche size distribution. Space-time correlations of the local velocities show a simple diffusion growth behaviour.

PACS numbers: 62.20.mt, 46.50.+a, 68.35.Ct

I. INTRODUCTION

Failure of heterogeneous materials has a vast importance in geophysical systems, industrial applications and of course fundamental physics. This subject is far from understood, and has been studied extensively over the years [1–3]. Of key importance for brittle materials is the competition between pinning forces due to local material heterogeneities and elastic forces due to outer applied stress, resulting in a complex roughening of fracture surfaces. In general this competition triggers a rich history dependence of the fracture process. Up until quite recently, a broad range of experimental and simulation studies have been concerned with the morphology of either fracture surfaces in the case of three-dimensional solids [4], or interfacial crack fronts for planar fracture [5–7]. In both geometries it has been well established that the fracture roughness exhibits self affine scaling properties [8–11]. To this end, theoretical approaches have been suggested: the fluctuating line model [12, 13], where the interface is seen as an elastic string propagating in a rough morphology, being pinned with different strengths at different positions, and also the stress weighted percolation approach [14] with a damage zone ahead of the crack.

In this study, we will pay our attention to the dynamics of fracture propagation. Owing to the material heterogeneities, the motion is complex and characterised by abrupt jumps separated by periods of rest. Both the jumping and the resting behaviour span a large range of time scales. This dynamics is often referred to as *Crackling Noise* [16]. Apart from direct observation of fracture [17–20], such intermittent dynamics embody also large scale activity in earthquakes [21–23], acoustic emission during material failure (fiberglass [24],

rocks [25], paper [26] etc.), magnetic domain wall motion (Barkhaussen noise) [27], wetting contact line motion on a disordered substrate [28, 29], and imbibition fronts in porous media [30].

Studies on fracture propagation often characterize the complex dynamics through related effective average quantity, due to the difficulties of direct observation and/or insufficient resolution of the spatio-temporal behaviour at local scale. In contrast we use here a transparent PMMA model for in-plane mode-I fracture well suitable for capturing optically detailed intermittent behaviour with high precision in both time and space [5].

The present work is a completion and substantial extension of the experimental study presented by Måløy *et al.* in [18], where the concept of the waiting time matrix was introduced; a consistent way of obtaining the local velocity field of the propagation of a pinned interface. Statistical analysis, based on the waiting time matrix, of avalanche behaviour in fracture front propagation has since been followed up by simulations. Bonamy *et al.* [32] quantitatively reproduced the intermittent crackling dynamics observed in experiments, using a crack line model based on linear elastic fracture mechanics extended to disordered materials. Using a similar string model, but with pure quasistatic driving and zero average propagation velocity, Laurson *et al.* [33] have recently proposed a scaling relation connecting the global activity with the observed local avalanches, connecting the dynamics at large and small scales. Further they find that the aspect ratio of local avalanches is consistent with recent experimental advances of multiscale roughness analysis [7]. Experimentally, Grob *et al.* [31] have, through the terminology of seismic catalogs, been able to compare the dynamics of interfacial crack propagation to what is found in shear rupture for earthquakes.

Most of the previous studies mentioned in the above paragraph address only rapid event statistics, for a fracture propagation that is forced by the imposed boundary conditions (critical fracture propagation). What we present here is more elaborate and general in the sense that we consider intermittency in *both* high and low velocity regimes of crack propagation using two different methods of external loading: 1) constant opening velocity of the crack and 2) creep relaxation of a crack maintained at a constant opening distance. While it is easy to imagine that these different boundary conditions will give a very different global behaviour, we are surprised to find that the local dynamics is similar in every respect. This is shown by statistical analysis of high and low velocity events, referred to as depinning and pinning clusters respectively, and by considering the autocorrelation of the velocity field. The vanishingly small timecorrelations have been related to the time evolution of the width of the fracture front [17]. We see that it follows simple diffusion growth. Another important finding is that the pinning and depinning size distributions are described by the same power law exponent. Moreover we propose a relationship between the different power law exponents describing the fracture process, thus linking velocity fluctuations with spatial avalanches.

This paper is organized as follows: In Sec. II we describe in detail the experimental setup, including sample preparation, loading conditions and optical setup. We then present the results in Sec. III starting with the distribution of local velocities along the fracture front (Sec. III A). In Sec. III B we obtain the autocorrelation functions in time and space for these velocities. Finally in Sec. III C we give the main statistical analysis of spatial clusters that we eventually show to be linked to the local velocity distribution in Sec. III A. Section IV summarizes the paper with concluding remarks.

II. EXPERIMENTAL SETUP

A. Sample preparation

The experimental setup [5, 6, 31] is shown in Fig. 1. The fracture sample is made out of two transparent Plexiglas (PMMA) plates: a thicker plate with dimensions $(30, 14, 1)$ cm and a thinner plate with dimensions $(30, 10, 0.4)$ cm for the length, width, and thickness respectively. The plates are then sandblasted on one side using glassbeads ranging between $50 \, \mu m$ and $300 \, \mu m$ in diameter. Sandblasting introduces random roughness on the originally "flat" surface. This causes light to be scattered in all directions from these microstructures, hence transparency of the plate is lost and it becomes opaque. The plates are then clamped together in a pressure frame, with the sandblasted sides facing eachother. The pressure frame is made of two parallel aluminum plates, exerting a normal homogeneous pressure on both sides of the PMMA. Finally, the pressure frame is put

in a ceramic temperature controlled oven at $205\,^{\circ}$C for $30 - 50$ min. This annealing or sintering procedure creates new polymer chains between the two plates and the resulting PMMA block is now fully transparent. The new layer created between the two plates are weaker than the bulk PMMA, so that we obtain a weak plane with quenched disorder in which the fracture can propagate. This system is ideal for direct visual observation since the fractured part of the sample immediately becomes opaque whereas the unfractured part remains transparent. The sharp and high contrast boundary between transparent and opaque parts thus defines the fracture front.
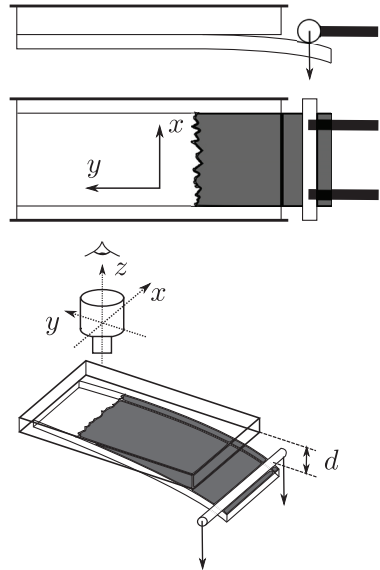

FIG. 1: Sketch of the experimental setup. Two PMMA plates are sintered together, creating a weak in-plane layer for the fracture to propagate. Fracture is initiated by lowering a cylindrical press bar, controlled by a step motor, onto the lower plate. The uncracked part of the sample is transparent, whereas the cracked part has lost transparency hence creating a good contrast at the fracture front. The fracture front is imaged from above by a digital camera. The deflection d (z-direction) between the plates is indicated in the lower panel. The fracture plane is (x, y), where the x-direction is transverse to the average direction of fracture propagation whereas the y-direction is parallel to the average direction of fracture propagation.

The rough surface generated by the sandblasting technique depends on the volume flux of the beads, the kinetic energy of the beads, the bead size, and the total time of the sand blasting. It is important to note that there is no obvious direct link between the bead size and the characteristic size of the disorder. The rough surface will after annealing give local toughness fluctuations. The strength

of these fluctuations will depend on the sintering time. The relationship between the disordered morphology of the plates and the toughness fluctuations is very difficult to access experimentally. However we know that the toughness fluctuations will change when the disorder of the plates changes [7]. In [35] a white light interferometry technique was used to measure the rough surface, sandblasted with $50 - 100 \, \mu$m particles, and it was found that the local heterogeneities had a characteristic size of $\sim 15 \, \mu$m. Other samples have been studied through a microscope [6] where the random position of the defaults and the maximum size of the defaults was seen to roughly correspond to the bead size $\sim 50 \, \mu$m. However we emphasize that the image pixel resolution is smaller ($\sim 1 - 5 \, \mu$m) and the largest length scales considered ($\sim 10^3 \, \mu$m) is much larger than the sample disorder.

Two different PMMA samples, characterised by the glass bead diameter, have been used in our experiments. Sample #1 has been sandblasted with $100 - 200 \, \mu$m beads whereas sample #2 has been sandblasted with $200 - 300 \, \mu$m beads. Both samples where sintered in the oven for 50 min.

B. Mechanical setup and loading conditions

The thick plate of the PMMA block is mounted on a rigid aluminum frame, also containing a camera setup for imaging. Mode-I fracture is induced by a normal displacement of the thin plate pushed by a cylindrical press bar, as shown in Fig. 1. Indicated is also the definition of our coordinate system, where (x, y) is the fracture plane: the x-direction is transverse to the average direction of fracture propagation whereas the y-direction is parallel to the average direction of fracture propagation. The deflection d is defined as the plate separation at the position of the press bar. A bit of glycerol is put on the contact between the plate and the press bar to reduce any friction and prevent shear loading. The pressbar is mounted to a force gage on a vertical translation stage controlled by a step motor, so that it can be moved up and down in the z-direction. Through the force gage we are able to monitor the force exerted on the lower plate during an experiment.

We use two sets of loading conditions: 1) The imposed deflection d (see Fig. 1) as a function of time t is given by

$$d(t) = v_p t \, , \qquad (1)$$

where v_p is the velocity of the press bar. Throughout the experiment we can measure the force F on the lower plate at the position of the press bar. As an example, the force development during an experiment is shown in the upper panel of Fig. 2(a). Initially there is a period of linear increase, corresponding to pure elastic bending of the lower plate. At some point, indicated by the dashed line, linear behaviour is deviated and fracturing occurs. After some transient period, the force decays only slowly in

time as the fracture propagates in the sample. The corresponding linear increase of the deflection is shown in the bottom panel. We will refer to these loading conditions as *constant velocity boundary conditions* (CVBC).
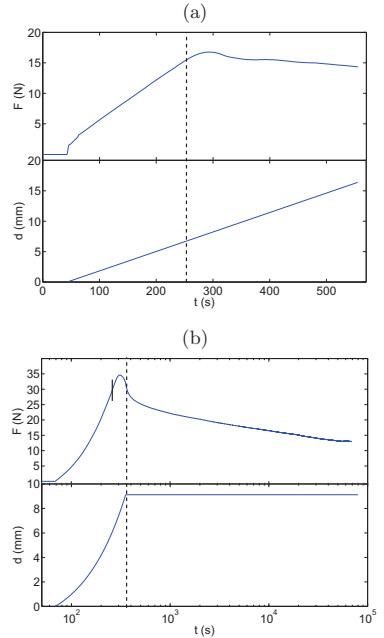

FIG. 2: **(a)** Constant velocity boundary conditions (CVBC). Upper panel shows the force development $F(t)$ on the lower plate as it is bent by the pressbar. The dashed line indicates the onset of fracturing. Lower panel shows the linear increase of the deflection $d(t)$. **(b)** Creep boundary conditions (CBC). Same as in (a) but $F(t)$ and $d(t)$ are in semilog scale. The short solid line in the upper panel indicates the onset of fracturing, whereas the dashed line indicates the time at which the pressbar is stopped and maintained in a constant position according to Eq. (2).

2) The deflection is given by

$$d(t) = \begin{cases} v_p t & \text{for } t < t_{stop} \\ \text{const.} & \text{for } t > t_{stop} \end{cases} , \qquad (2)$$

where t_{stop} marks the time at which the step motor controlling the pressbar is switched off, i.e $v_p = 0$. We will refer to these loading conditions as *creep boundary conditions* (CBC), since it is seen that the fracture front continues to propagate at "creepingly slow" velocities over several days after t_{stop}. An example is shown in Fig. 2(b), where we see a logarithmic decay of the force while the deflection is maintained constant. Motivated by the different global behaviour of the fracture in CVBC and CBC,

we have performed experiments using both loading conditions to study the local dynamics.

C.   Optical setup

The front propagation is followed in time using a high speed digital camera mounted on a microscope. In one experiment between 12 000 and 30 000 frames are captured using either the *Photron Fastcam-Ultima APX* (512×1024 pixels) or the *Pixelink Industrial Vision PL-A781* (2200×3000 pixels). High-resolution images ($\sim 1 - 5\,\mu$m/pixel) are captured at high frame rate relative to the average propagation velocity of the crack front (see Table I). This is important as the local fluctuations in velocity can range over several decades. As large amounts of data are accumulated, we only have the possibility to follow the fracture front over short time windows compared to the long-time global development in the examples shown in Fig. 2. Both in the case of CBC and CVBC these time windows are small enough so that the average propagation velocity of the crack front is considered constant. Also for CBC we did several experiments with very different average velocity (Fig. 2(b)) during the same loading periods. The span of the timewindows will of course vary depending on the average velocity, but the y-distance (parallel to direction of propagation) covered by the crack front is roughly $\sim 500\,\mu$m in all our experiments. Finally, image capture is initiated only after onset of the fracture process.

The obtained grayscale images of the fracture front contain two parts: a dark and a bright region, corresponding respectively to the uncracked and the cracked part of the sample. The gray level distribution of the image thus presents two distinct peaks. Image analysis is performed to obtain the coordinates of the fracture front line, $h(x,t)$, separating the two regions. This is done by thresholding the grayscale image at the local minimum of the gray level histogram, between the bright and dark peak. We then obtain a black and white image from which the front can easily be extracted. We always obtain a very good contrast between the cracked and uncracked part of the sample; the extracted fronts are very robust with respect to perturbations in the chosen threshold. For a more detailed description of the front extraction and image treatment see [6, 31].

Fig. 3 shows an extracted front line $h(x,t)$ superimposed on the corresponding raw image. Its roughness is due to local pinning asperities of high toughness, created as a result of the sandblasting and annealing procedure as explained earlier. Occasionally, on small scales close to the pixel resolution, the front shows local overhangs and is not always a single valued function of x. However the number of overhangs per front and the scale at which they occur are small; hence we construct the single valued front $h(x,t)$ by keeping only the most advanced y−coordinate at the front line for a given x−coordinate. Arbitrarily we could also have chosen the least advanced
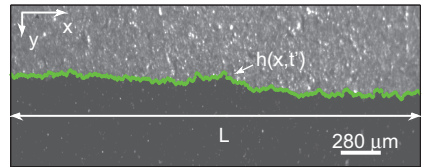

FIG. 3: Fracture frontline $h(x,t')$ at some time t', superimposed on the corresponding raw image. Direction of propagation is from top to bottom. System size L in the x-direction is indicated.

y−coordinate. Single valued fronts are constructed in order to simplify the statistical analysis, which has shown not to influence the results.

III.   RESULTS

The rough fracture front exhibits self-affine scaling properties [8–11, 13, 14] together with a complex avalanche like motion with very large velocity fluctuations. Due to the large temporal and spatial variations in front velocity it is not straight forward to analyze the local dynamics by a simple front subtraction procedure. Therefore we characterize this complex behaviour by measuring the local waiting time fluctuations of the crack front during its propagation, following the procedure introduced first in [18]. We compute a so called *waiting time matrix* (WTM) [30–32], which is a pinning time map with elements w, giving the amount of time the front is pinned down or fixed at a particular position (x,y) in time step units. As explained in Appendix A, the local velocity v at a given position is given as $v = a/(w\,\delta t)$. Using $h(x,t)$ and the WTM, it is then straight forward to obtain the local velocities along a fracture front $v(x,t)$. Furthermore, by computing $v(x,t)$ for all time steps, we build the spatio-temporal velocity map $V_t(x,t)$. The average velocity $\langle v \rangle$ is defined as the average over all elements of $V_t(x,t)$, i.e the total average over all fronts.

Presented below are the results of eight experiments (both CBC and CVBC), spanning a broad average propagation velocity range, where we have characterized the local dynamics. The total duration of an experiment is within the range of 4 seconds to 7 hours, whereas the average distance of front propagation, is $\sim 500\,\mu$m in all cases. The details of each experiment can be found in Table I. Additionally we will also compare the present data to previous experiments from [18].

A.   Distribution of local velocities

A gray scale map of the waiting time matrix is shown for a CBC experiment in Fig. 4. Dark regions correspond

TABLE I: Parameters of the different experiments, sorted after the average propagation velocity of the front $\langle v \rangle$: System size L (x−direction), image timestep δt gives the time delay between the capture of two subsequent images, resolution a gives the pixel resolution of an image, displacement type denotes the set of boundary conditions used, and the last column indicates the sample number. Sample #1 has been sandblasted with $100 - 200\,\mu m$ beads whereas sample #2 has been sandblasted with $200 - 300\,\mu m$ beads.

	$\langle v \rangle$ (μm/s),	L (μm),	δt (s),	a (μm/pixel),	displacement type,	sample
Exp1	0.028	6700	1	2.24	CBC	#2
Exp2	0.15	6700	5×10^{-1}	2.24	CBC	#2
Exp3	0.42	5600	2×10^{-2}	5.52	CVBC	#2
Exp4	1.36	5600	2×10^{-2}	5.52	CBC	#2
Exp5	2.4	2865	8×10^{-3}	2.83	CVBC	#1
Exp6	10.1	2865	2×10^{-3}	2.83	CBC	#1
Exp7	23	2865	2×10^{-3}	2.83	CVBC	#1
Exp8	141	2842	5×10^{-4}	2.83	CVBC	#1

to a high waiting time and thus a low velocity, and vice versa for bright regions. The dark low velocity regions are seen to occur as irregularly shaped "lines", separated by brighter compact regions referred to as high velocity avalanches. The wide span of waiting times shown by the colorbar, together with their irregular distribution in space, is direct visual confirmation of the complex dynamics found in this system. Furthermore, the visual impression of the WTM for a CBC experiment compared to a CVBC experiment is identical. The similarity of the local dynamics in CBC and CVBC experiments is also confirmed in our analysis, as we will return to.

From the local velocities along all front lines $V_t(x, t)$ we can compute the normalized probability density function (PDF) $P(v)$. By rescaling every local velocity with the average propagation velocity $v/\langle v \rangle$, we obtain a data collapse for all experiments as shown in Fig. 5. In this figure the results from all experiments in Table I are put on top of previous experiments from [18]. It was found that

$$P(v/\langle v \rangle) \propto (v/\langle v \rangle)^{-\eta} \quad \text{for} \quad v/\langle v \rangle > 1 \,, \quad (3)$$

with the exponent $\eta = 2.55 \pm 0.15$. The result primarily obtained for CVBC is now extended to the case of creep experiments. It is indeed very stable over the different experiments, considering the wide range of average velocities. We emphasize that Fig. 5 provides quantitative confirmation on the similarity between the local dynamics for CBC and CVBC experiments.

At this point we divide the velocity distribution in two and define: a *pinning* regime for $v/\langle v \rangle < 1$ and a *depinning* regime for $v/\langle v \rangle > 1$, as indicated in Fig. 5. The Fig. 5 inset shows the corresponding PDF of waiting times $P(w/\langle w \rangle)$. Through Eq. (A2) the two distributions are related by $P(v)dv = P(w)dw$ (cf. Eq. (35)), giving $P(w/\langle w \rangle) \propto (w/\langle w \rangle)^{\eta-2}$ for $w/\langle w \rangle < 1$. Note that the waiting time distribution decays very fast in the pinning regime compared to the depinning regime.

B. Space and time correlations

The power law distribution of the local velocities confirms the visual impression of a non trivial local dynamics of the fracture process. As mentioned earlier, the front propagates through high velocity bursts of different sizes. An important question is thus how the local velocities along and between different front lines are correlated in space and time.

We define the normalized autocorrelation function $G(\Delta x)$ and $G(\Delta t)$ for the local velocities on all frontlines $v(t, x)$ in space and time as

$$G(\Delta x) = \left\langle \frac{\langle (v(x + \Delta x, t) - \langle v \rangle_x)(v(x, t) - \langle v \rangle_x) \rangle_x}{\sigma_x^2} \right\rangle_t \quad (4)$$

$$G(\Delta t) = \left\langle \frac{\langle (v(x, t + \Delta t) - \langle v \rangle_t)(v(x, t) - \langle v \rangle_t) \rangle_t}{\sigma_t^2} \right\rangle_x \,, \quad (5)$$

where $\langle v \rangle_x$ and σ_x is the spatial average and standard deviation respectively at a given time in $V_t(x, t)$, whereas $\langle v \rangle_t$ and σ_t is the temporal average and standard deviation respectively for a given position in $V_t(x, t)$. The outer brackets in Eqs. (4) and (5) denotes an average over all different realizations in time and space respectively, i.e over all columns and rows in the V_t matrix.

In Fig. 6 the spatial correlation function $G(\Delta x)$ is shown for all experiments listed in Table I. It is more or less evident that correlation functions obtained from the same sample are grouped together, independently of the average propagation velocity and loading condition. By fitting the data with power law functions with an exponential cutoff we get

$$G(\Delta x) \propto \Delta x^{-\tau_x} \exp(-\Delta x/x^*) \,, \quad (6)$$

where $\tau_x = 0.53 \pm 0.12$ is the average exponent and $x^* = \{92, 131\}\,\mu$m is the average cutoff or correlation length of the local velocities in the x-direction, for sample #1 and #2 respectively. The quality of the fits is not perfect, as
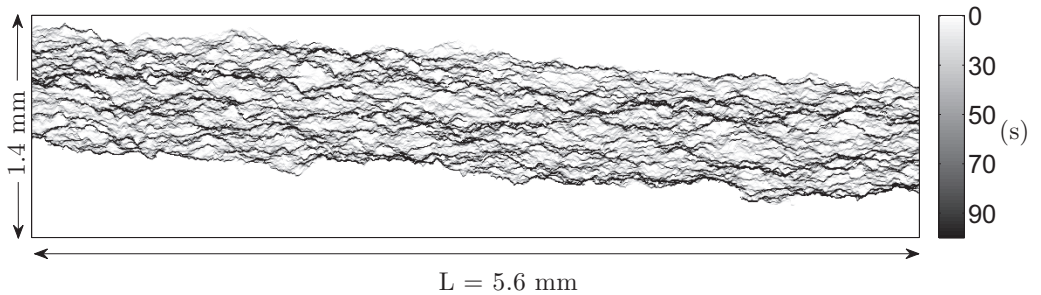
FIG. 4: Waiting time matrix of a CBC experiment, $\langle v \rangle = 1.36\,\mu$m/s. The map results from the extraction of 24 576 front lines at a rate of 50 fps. Dark regions correspond to a high waiting time and thus a low velocity, and vice versa for bright regions, as shown in the colorbar indicating the amount of time (in seconds) the front has been fixed at a given position. Black pinning lines are visible, with bright depinning regions in between. The system size L is indicated.
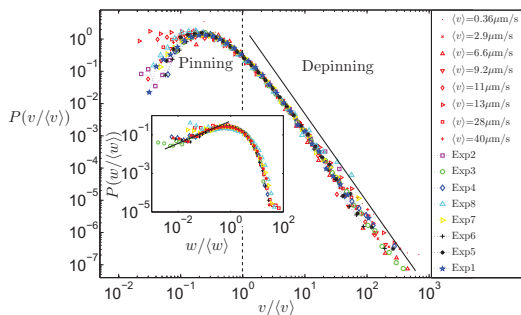

FIG. 5: Distribution of local velocities $P(v/\langle v \rangle)$ rescaled by the average propagation velocity for various experimental conditions: A range of roughly four decades in average crack front velocity including both CBC and CVBC experiments. Symbols colored red are results from [18]. A fit to all the data for $v > \langle v \rangle$ shows power law behaviour with an exponent -2.55. Inset shows the corresponding waiting time distribution $P(w/\langle w \rangle)$ The exponent transforms in this case to 0.55.
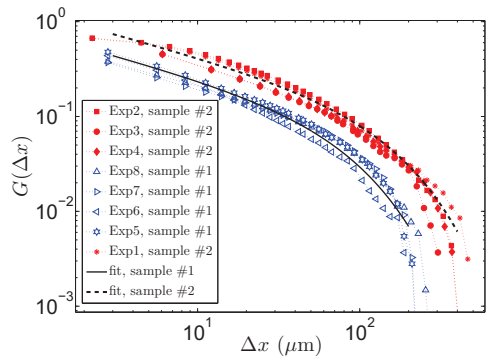

FIG. 6: Space correlation functions $G(\Delta x)$. Functions from the same sample are grouped together (sample #2 - filled markers, sample #1 - open markers). A power law with exponential cutoff has been fitted to each group of correlation functions, as indicated by the solid and dashed line for sample #1 and #2 respectively (see text).

can be seen in Fig. 6, but they represent each group of correlation functions fairly well. It is to be noted that extracting well defined correlation lengths is not trivial in our data. Other estimators of Eq. (4) are possible to use, e.g the power spectrum method.

In Fig. 7(a) the time correlation function $G(\Delta t)$ is shown for all experiments listed in Table I. For each experiment, functional fits analog to Eq. (6) have been made. Using the average value of the power law exponent $\tau_t \approx 0.43$ and different cutoff correlation times t^*, a good collapse is obtained. We note also that t^* is small; typically more than two orders of magnitude smaller than the duration of an experiment. The inset shows the scaling of the correlation time with the average propagation velocity

$$t^* = y^*/\langle v \rangle \ , \tag{7}$$

where $y^* \approx 7\,\mu$m. The proportionality constant y^* has the dimension of a length since the scaling exponent equals minus unity. This length scale is on the order of the pixel resolution a and also within the disorder limit. Hence y^* is very small and might be influenced both by resolution and disorder effects. For comparison we calculate $G(\Delta y)$ directly, i.e. the velocity autocorrelation in space along the direction of propagation, defined similar to Eq. (4) and shown in Fig. 7(b). We find no power law decay in this case but the drop to zero correlation occurs between $10-20\,\mu$m consistently with y^*. Correlation functions from the same sample are shown in similar colors (red - sample #2, blue - sample #1). Within the
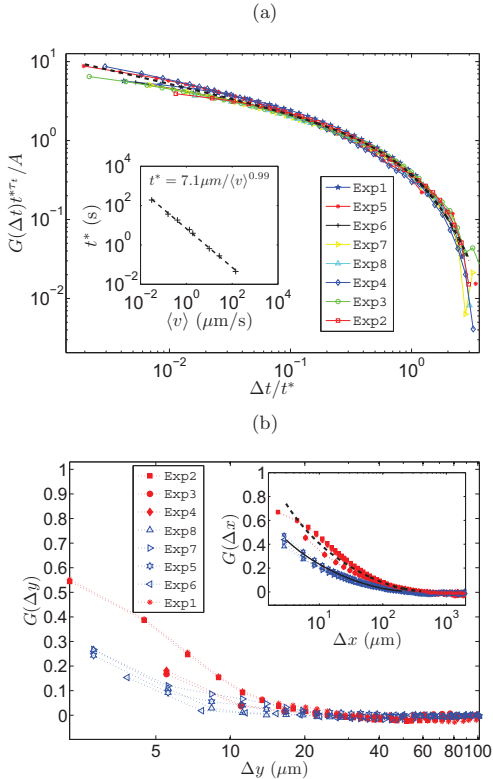
(a)

(b)

FIG. 7: **(a)** Time correlation functions collapsed onto eachother according to a power law with an exponential cutoff $G(\Delta t) = A\Delta t^{-\tau_t}\exp(-\Delta t/t^*)$. The exponent is $\tau_t \approx 0.43$. Inset shows the scaling between the crossover correlation time and average propagation velocity $t^* \approx 7\,\mu m/\langle v\rangle$. **(b)** Space correlation function $G(\Delta y)$ with logarithmic $\Delta y-$axis. Consistently with (a) and Eq. (7), the local velocities become uncorrelated after only a short distance ($\sim 10-20\,\mu m$) in the $y-$direction. Correlation functions from experiments performed on sample #2 and #1 have filled and open markers respectively. To some extent we see also here grouping of experiments from the same sample. The difference is however not as clear as for the spatial correlations along the transverse $x-$axis (subparalell to the fronts), on the inset showing $G(\Delta x)$ with logarithmic $x-$axis. The reason might be that the drop to zero correlation occurs close to the resolution scale for $G(\Delta y)$.

interval $\{a, 20\}\,\mu m$, where a is the image resolution, the sample grouping is not so clear as in the case for $G(\Delta x)$ as shown in the inset, but the same initial trend is observed. This can be attributed to resolution effects and the very small correlation lengths. Thus at the time and length scales we are looking at, the local velocities are considered uncorrelated in the $y-$direction.

Since the local fluctuations control the global advance-

ment of the crack, it is of interest to consider the evolution of the width of the fracture front in time. This growth process is known to depend on the system correlations. It has been shown previously [15] that uncorrelated growth processes such as simple diffusion, Brownian motion, etc, can be described by a growth exponent $\alpha = 1/2$. For the present case we define the *root-mean-square* (RMS) value of the front width $\Delta h(t)$ as

$$\langle \Delta h(t)^2\rangle^{\frac{1}{2}} =$$
$$\left\langle \left[\left(h(x, t+t_0) - \overline{h}\right) - \left(h(x, t_0) - \overline{h}_0\right)\right]^2\right\rangle^{\frac{1}{2}}_{x,t_0}, \quad (8)$$

where $h(x, t_0)$ is an initial front line and $\overline{h}$ indicates a positional average height at a given time. This differs somewhat from the usual situation of a front growth from an initially flat front. In our case the front width is defined as the fluctuations from an initially rough line which corresponds to the geometry of the front at the onset of the experiment. The front width is related to the autocorrelation of local velocities in time. By rewriting Eq. (8) and using that $h(t+t_0) - h(t_0) = \int_{t_0}^{t+t_0} v(t')dt'$ we obtain

$$\langle \Delta h(t)^2\rangle = \left\langle [h(x, t+t_0) - h(x, t_0)]^2\right\rangle - (t\langle v\rangle)^2$$
$$= \int_{t_0}^{t+t_0}\int_{t_0}^{t+t_0}\langle v(n)\cdot v(m)\rangle dm\, dn - (t\langle v\rangle)^2 . \quad (9)$$

By substituting $n + \Delta t = m$ and using Eq. (5) we get

$$\langle \Delta h(t)^2\rangle = \int_{t_0}^{t+t_0}\int_{t_0-n}^{t+t_0-n}\langle v(n)\cdot v(n+\Delta t)\rangle d\Delta t\, dn \ ...$$
$$- (t\langle v\rangle)^2$$
$$= \sigma_t^2 \int_{t_0}^{t+t_0} dn \int_{t_0-n}^{t+t_0-n} d\Delta t\, G(\Delta t) . \quad (10)$$

As argued above, we consider the local velocities uncorrelated in time. The regime where $G(\Delta t)$ behaves as a power law is very short, and should only affect $\Delta h(t)$ on very small time scales. Thus we approximate the autocorrelation function with the Dirac delta function $G(\Delta t) \approx \delta(\Delta t)$ which gives

$$\langle \Delta h(t)^2\rangle \propto t \quad \Rightarrow \quad \langle \Delta h(t)^2\rangle^{\frac{1}{2}} \sim t^\alpha , \quad (11)$$

with the growth exponent $\alpha = 1/2$. Figure 8 shows the scaling of the front width as a function of time for all experiments. We find indeed a growth exponent $\alpha = 0.55 \pm 0.08$ consistent with Eq. (11), as indicated by the fitted dashed line. The large scale crossover is an effect of a limited system size in the direction of crack propagation. Our direct measurement of the growth exponent also agrees with the indirect measures in [17, 35], where the front width power spectrum was analysed at different times and interpreted in terms of a Family-Vicsek scaling, with a dynamic exponent $\kappa = 1.2$ and a roughness exponent $\delta = 0.6$ giving $\alpha = \delta/\kappa = 0.5$.
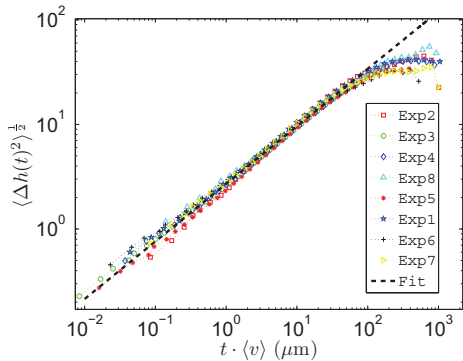
FIG. 8: Scaling of the front width as a function of time, rescaled with the average velocity. The dashed line corresponds to $\langle \Delta h(t)^2 \rangle^{\frac{1}{2}} \propto t^{0.55}$.

Due to the one-to-one correspondence between velocity and waiting time [Eq. (A2)], the above analysis of correlations could just as well have been performed using the latter quantity. Calculating $G(\Delta x)$, $G(\Delta t)$ and $G(\Delta y)$ using w, we obtain approximately the same trends and correlation lengths as for v. We turn now to the statistics of the dynamical avalanches in the pinning and depinning regimes.

C. Cluster analysis

1. Spatial map of clusters

As discussed earlier the local dynamics of the fracture front is a mix of pinning lines where the front is fixed or only moves slowly, and sudden propagation in high velocity jumps or bursts. The statistics in both the pinning and depinning regimes will be shown to be scale invariant and characterized by equal scaling exponents. In order to study both these regimes we apply a thresholding procedure to the velocity matrix $V(x,y)$ and obtain a thresholded binary matrix V_C:

$$V_C = \begin{cases} 1 & \text{for } v \geq C \langle v \rangle \\ 0 & \text{for } v < C \langle v \rangle \end{cases} \quad , \qquad (12)$$

for the depinning regime and

$$V_C = \begin{cases} 1 & \text{for } v \leq \frac{1}{C} \langle v \rangle \\ 0 & \text{for } v > \frac{1}{C} \langle v \rangle \end{cases} \quad , \qquad (13)$$

for the pinning regime. Here C is a threshold constant of the orders of a few unities. An example of a thresholded matrix V_C in both regimes is shown, in Fig. 9. The geometrical characteristics of the two regimes can be seen quite clearly. Depinning clusters (high velocity regions) are compact and extend somewhat longer in the $x-$direction than in the $y-$direction. Pinning clusters (low velocity regions) have also a long $x-$direction extension, but are very narrow in the $y-$direction on the other hand. Thus they can be described almost like irregularly curved lines in the fracture plane. From Eq. (12) it is clear that the cluster size decreases with increasing values of the threshold parameter C in both regimes. Obviously one must choose reasonable values of C in the two regimes as the number of clusters goes to one and zero when C is very small or very large respectively.

In order for the thresholding of the velocity matrix to be consistent, it is important to note that the average velocity must be constant in time to avoid clusters from being affected by a size gradient. Thus we ensure that the duration of image capture is short enough for the global development of the average velocity to be approximated as constant for CBC and CVBC experiments.

2. Size distribution of clusters

We will denote the size/area of a cluster, for both pinning and depinning, S. Figure 10 shows for $C = 3$ the normalized probability density function (PDF) of the sizes $P(S)$ respectively for all experiments. There are several aspects to emphasize about these figures. First of all, the distributions show a power law decay, with a cutoff for large sizes S. Furthermore the distributions fall on top of eachother, meaning that they span the same range of cluster sizes, independently of the average propagation velocity. There is neither no clear indication that the PDF cutoffs depend on the correlation length x^*. It is thus reasonable to average cluster data from all the experiments to improve in particular the tail of the distribution. Finally, the distributions from both CBC and CVBC experiments cannot be distinguished. Thus the distributions seem to indicate that the local dynamics are very similar in the two cases, despite very different boundary conditions. We will in the following quantify the properties of these distributions.

Figure 11 shows the averaged $P(S)$ distributions for a threshold range $C = 2 - 12$ in the pinning regime. It is clear that the distributions follow a power law with an exponential like cutoff. Furthermore it is evident and to be expected that the size of the largest clusters, i.e. the cutoff cluster size, decreases with increasing values of the threshold level. A similar behaviour is found for the PDFs of cluster sizes in the depinning regime, but the cutoff size is generally larger due to the cluster geometry. In contrast to what was done in [18], where the distributions were rescaled by the average cluster size ($P(S/\langle S \rangle)$), we choose to fit the distributions according to the function

$$P(S) \propto S^{-\gamma} \exp(-S/S^*) \,, \qquad (14)$$

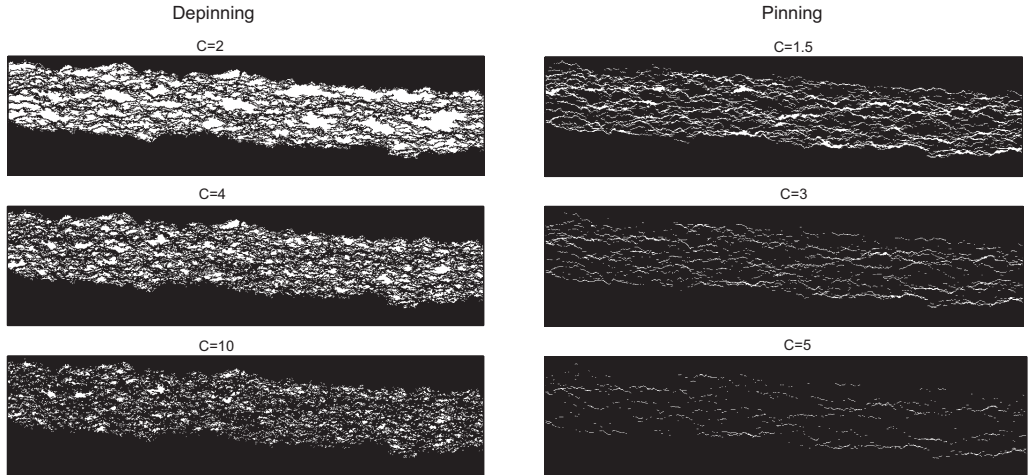where S^* is the cutoff cluster size and γ the power law exponent. This is shown for the pinning regime in Fig. 11,

Depinning

C=2

C=4

C=10

Pinning

C=1.5

C=3

C=5

FIG. 9: Thresholded matrix V_C (5600×1400)μm in the depinning (left) and pinning (right) regime for a CBC experiment with $\langle v \rangle = 1.36\,\mu$m/s. White clusters correspond to velocities C times larger than $\langle v \rangle$ for the depinning case, whereas white clusters or lines correspond to velocities C times less than $\langle v \rangle$ for the pinning case.
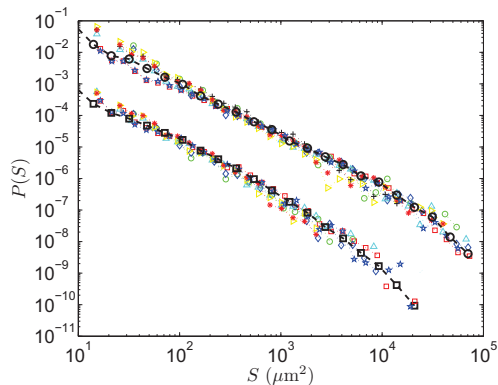

FIG. 10: Probability distribution function $P(S)$ for all experiments using a threshold $C = 3$. A distribution averaged over all experimental conditions is also included for the depinning (dashed line and circular markers) and pinning regime (dashed line and square markers). The pinning size distributions have been shifted along the $y-$axis to enhance visual clarity.

FIG. 11: Distributions of pinning clusters $P(S)$ averaged over all different experimental conditions, for a threshold range $C = 2 - 12$. Solid lines show the fits corresponding to a power law with an exponential cutoff.

where fitted solid lines are plotted on top of the averaged experimental data (similar fits have been obtained for the depinning regime). We find that in *both* regimes, the cluster size PDF scales with an average exponent $\gamma = 1.56 \pm 0.04$. Using this exponent, and the fitted values for the cutoff cluster size we obtain a data collapse

in both velocity regimes for the full range of available threshold values, as shown in Fig. 12. Furthermore we find a scaling relation between the cutoff cluster size S^* and the threshold level C, as shown in the inset of Fig. 12. For the depinning regime it is given by

$$S^* \propto C^{-\sigma_d} \ , \tag{15}$$

where $\sigma_d = 1.77 \pm 0.16$. Similarly, we obtain for the

FIG. 12: Collapsed $P(S)$ distributions averaged over all different experimental conditions for both depinning (upper set of data) and pinning (lower set of data). The pinning distributions have been shifted for visual clarity. Depinning and pinning thresholds are in the range $C = 2-22$ and $C = 2-12$ respectively. The dashed and the solid line both 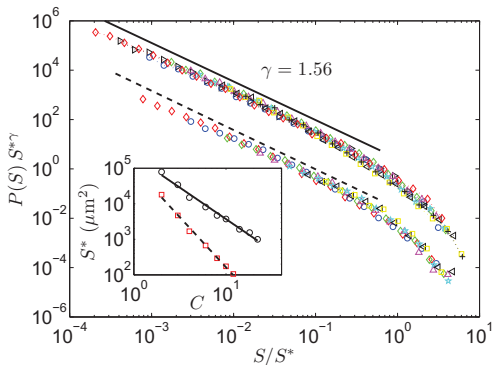have the slope $\gamma = 1.56$. Inset shows the scaling between the cutoff S^* and the threshold C for the depinning (solid line $\sigma_d = 1.77$) and pinning regime (dashed line $\sigma_p = 2.81$).

pinning regime.

$$S^* \propto C^{-\sigma_p} , \qquad (16)$$

where $\sigma_p = 2.81 \pm 0.23$.

The exponent $\gamma = 1.56$ is somewhat lower but consistent with the previously reported value in [18] ($\gamma = 1.7 \pm 0.1$), in which the distributions were rescaled by the average cluster size in lack of a pronounced cutoff size. A later check using the rescaling as explained in the above paragraph does show to lower the exponent also for the old data. We would like to mention that our experimentally obtained exponents γ and σ_d are in excellent agreement with the recent numerical study of high velocity clusters in planar crack front propagation by Laurson *et al.* [33]. They use an empirical value of $\sigma_d = 1.8$ to describe the relationship between the cutoff size and the threshold. Their value of the size exponent $\gamma = 1.5$ is explained theoretically from the decomposition of a global avalanche (collective movement of the front as a whole) into local clusters. The experimental equivalent to the suggested numerical approach is to study how the fluctuations of the spatially averaged instantaneous velocity $\langle \frac{\partial h}{\partial x}(x,t) \rangle_x$ relates to the distribution of local clusters that we observe here. We do not consider global avalanches in this study but it is certainly available in our data and is a work in progress.

3. Scaling relations

The collapse in Fig. 12 shows that the scaling in Eqs. (15) and (16) are well satisfied. If we first consider the depinning regime, it is possible to relate the exponents σ_d and γ of the cluster size distribution [Eq. (14)] to the exponent η characterising the spatio-temporal distribution of local velocities [Eq. (3)]. The latter distribution is obtained from $V_t(x,t)$, i.e the velocity map in space and time of all front lines [Eq. (A3) and Fig. 18 b)], thus the space-time fraction covered by local velocities between v and $v + dv$ is $P(v)dv$. One may also define the spatial distribution of local velocities, obtained from the spatial map of local velocities $V(x,y)$ [Eqs. (A1) and (A2)], denoted $R(v)$. The fraction of (x,y) space covered by local velocities between v and $v + dv$ is then $R(v)dv$. As shown in Appendix B, there is a relationship between these two probability density functions. Using Eq. (B5) gives

$$R(v) = \frac{P(v)}{\langle v \rangle} v \sim v^{-\eta+1} , \quad \text{for} \quad v > \langle v \rangle . \qquad (17)$$

The cumulative distribution of $R(v)$, from a given threshold C and up to the highest velocity, equals the area fraction that these velocities occupy out of the total area swept by the fracture front. In terms of threshold level we then get

$$R_c(v \geq C) = \int_C^\infty R(v)dv \sim C^{-\eta+2} . \qquad (18)$$

The same area fraction can also be expressed through the cluster size distribution, hence we obtain

$$R_c(v \geq C) = \frac{N\langle S \rangle}{A_{x,y}} \qquad (19)$$

$$\propto N \int_{S_{low}}^\infty SP(S)dS , \qquad (20)$$

where $A_{x,y}$ is the total area in the (x,y) plane where the fracture has propagated, N is the total number of clusters, $\langle S \rangle$ is the average cluster size, and S_{low} is the pixel size or some other lower cutoff. Substituting $P(S) = B S^{-\gamma} \exp(-S/S^*)$, where B is the normalization factor, in the above integral, we obtain for $\langle S \rangle$,

$$\frac{1}{B} = \int_{S_{low}}^\infty S^{-\gamma} \exp(-S/S^*)dS \qquad (21)$$

$$\langle S \rangle = B \int_{S_{low}}^\infty S^{1-\gamma} \exp(-S/S^*)dS , \qquad (22)$$

where S^* is the cutoff cluster size. Considering the normalization factor, we get by substituting $x = S/S^*$

$$\frac{1}{B} = S^{*1-\gamma} \int_{S_{low}/S^*}^\infty x^{-\gamma} \exp(-x)dx . \qquad (23)$$

Since the lower limit is very small and $\gamma = 1.56 > 1$, the power law part of the integrand will dominate and the contribution from the upper cutoff is negligible. Thus we approximate

$$\frac{1}{B} \approx S^{*1-\gamma} \int_{S_{low}/S^*}^\infty x^{-\gamma}dx \sim S^{*1-\gamma} \frac{S_{low}^{1-\gamma}}{S^{*1-\gamma}} = S_{low}^{1-\gamma} , \qquad (24)$$

which is independent of S^*. For the average cluster size we then obtain

$$\langle S \rangle \propto S^{*2-\gamma} \int_{S_{low}/S^*}^{\infty} x^{1-\gamma} \exp(-x)dx . \quad (25)$$

Since $\gamma - 1 = 0.56 < 1$, this integral will converge at the lower end, to a value independent of S_{low} as long as $S_{low}/S^* \ll 1$. Thus from Eq. (15), we obtain:

$$\langle S \rangle \propto S^{*2-\gamma} \propto C^{-\sigma_d(2-\gamma)} , \quad (26)$$

where $\sigma_d(2-\gamma) = 0.79$. Equation (26) is experimentally verified for $C > 3$, as shown in Fig. 13.
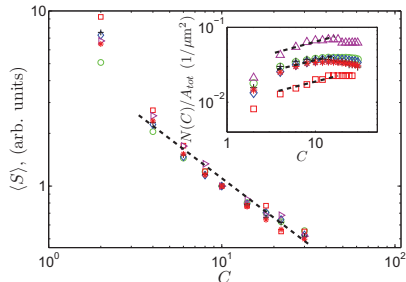

FIG. 13: Average cluster size $\langle S \rangle$ obtained from the image analysis vs. threshold level C. The dashed line shows a power law fit for $3 < C < 30$, with the exponent $-\sigma_d(2-\gamma) = -0.75$. Inset shows the number of clusters as a function of threshold level for the various experiments. The dashed lines all have the average slope $\chi = 0.28$.

The number of clusters N depends on the threshold level in a non-trivial manner. This is shown in the inset of Fig. 13. We see however that in the interval $3 < C < 16$ the number of clusters can be approximated by

$$N(C) \sim C^{\chi} , \quad (27)$$

where $\chi = 0.28$. Inserting Eqs. (18),(26) and (27) into Eq. (19) we obtain the following scaling relation

$$C^{-\eta+2} \sim C^{-\sigma_d(2-\gamma)+\chi} , \quad (28)$$

leading to a quantitative link between the exponent of local velocity distribution and the exponent of the event size distribution:

$$\eta = \sigma_d(2-\gamma) - \chi + 2 . \quad (29)$$

Inserting numbers in the above equation ($\eta = 2.55$, $\gamma = 1.56$, $\chi = 0.28$) we get that $\sigma_d = 1.88$, in good agreement with the empirically found value of $\sigma_d = 1.8$. Strictly speaking this result is only valid for $3 \leq C \leq 16$. If we now turn to the pinning regime, we note that from Eqs. (15) and (16), $\sigma_p \approx \sigma_d + 1$, allthough we can not derive it from a theoretical argument. The pinning threshold values spans a velocity interval $(v/\langle v \rangle) < 0.5$, in

which the $P(v/\langle v \rangle)$ distribution does not follow a power law (Fig. 5). Thus a similar scaling argument to the depinning regime, based on simple power law behaviours of all dependent variables, is not very likely to hold.

4. Cluster morphology

A depinning cluster of size S can be further decomposed into two extension lengths l_x - transverse to the average direction of front propagation and l_y - parallel to the average direction of front propagation, by fitting a bounding box. A bounding box is the smallest rectangle that can enclose the cluster, with sides l_x and l_y as shown in the left panel of Fig. 14 (a). As mentioned earlier, the pinning cluster geometry can be characterized as an irregularly curved line with a much larger extension in the $x-$direction compared to the $y-$direction. Due to this feature, l_y is not a good measure, and badly overestimates the $y-$direction extension. This is shown in Fig 14 (b) where bounding boxes for both pinning and depinning clusters are shown. Thus for pinning clusters we use l_x in the $x-$direction and the average cross sectional width l_{yw} as a measure of the $y-$direction extension, as shown in the right panel of Fig. 14 (a). Analysis shows
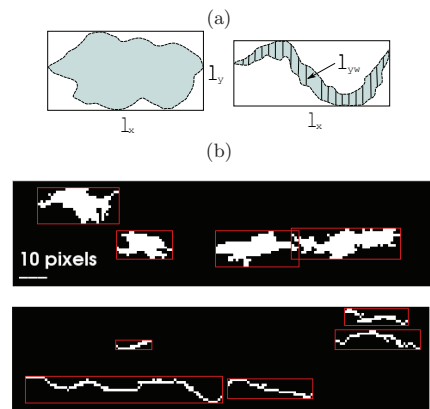
FIG. 14: (a) Left panel shows a bounding box with sides l_x and l_y embedding a depinning cluster. In this case the bounding box is a good measure of the linear extension of the cluster. Right panel shows a bounding box embedding a pinning cluster. In this case l_x gives a reasonable linear extent measure, however l_y does not, due to the irregular curvature (somewhat exaggerated in the figure) and to the narrow width in the $y-$direction. To characterize this width we use instead the average cross sectional width l_{yw}. (b) Upper and lower panel show bounding boxes for depinning and pinning clusters respectively from one experiment.

that for a cluster of size S, either depinning or pinning, the extension lengths have well defined means $\bar{l}_x$, $\bar{l}_y$, and $\bar{l}_{yw}$ increasing monotonically with S. Note here that the

bar denote the mean only over a narrow range of S and is not the overall mean. The corresponding standard deviations are small and proportional to these means. Due to the different definitions of l_y and l_{yw}, their absolute value cannot be compared directly. From analysis we find that, after an initial transient, $\bar{l}_y$ and $\bar{l}_{yw}$ do scale similarly but with different prefactors for depinning clusters. This is a consistency check between using either a bounding box or the cross sectional width to describe the $y-$direction extension. Thus l_{yw} is a reasonable measure for the $y-$direction extension of pinning clusters.

Figure 15 shows the scaling of the different extension lengths with the cluster size in the two regimes. In all cases there are differences between small (pixel resolution up to $S \sim 100 \mu m^2$) and large scale behaviour. In the case of depinning, for small S values, $\bar{l}_x$ and $\bar{l}_y$ scale more or less similarly indicating that clusters are isotropic at these scales. In the case of pinning, $\bar{l}_{yw}$ is very small and stays constant while $\bar{l}_x$ scales almost like the depinning cluster size. This is consistent with the characteristic linear geometry observed in the pinning regime. However the small scale behaviour ranges only over one decade, and might be affected both by resolution and disorder effects, so we do not have much information at these scales. The large scale behaviour spans close to three decades in S and displays robust scaling in all cases. From Fig. 15 we obtain the following relationship between extension lengths and cluster size

$$\bar{l}_x \propto S^{\alpha_x} , \quad \bar{l}_y \propto S^{\alpha_y} , \quad \bar{l}_{yw} \propto S^{\alpha_{yw}} \qquad (30)$$

for $S > 100 \mu m^2$ where $\alpha_x = 0.62 \pm 0.04$ is considered equal in both velocity regimes, $\alpha_y = 0.41 \pm 0.06$ in the depinning regime, and $\alpha_{yw} = 0.34 \pm 0.05$ in the depinning regime. The exponents in both regimes confirm the visually observed anisotropy of cluster extension. Note also the very small $y-$direction maximum extension ($\bar{l}_{yw} \sim 25 \mu m$) of pinning clusters, resulting from a small proportionality factor in the scaling relation. Furthermore we obtain approximately from the exponents in Eq. (30) that $S \sim \bar{l}_x \bar{l}_y \sim \bar{l}_x \bar{l}_{yw}$, meaning that the ratio of the approximated area from the extension lengths to the real cluster area is scale independent. From Eq. (30) we get the following $x-$ and $y-$direction aspect ratio:

$$\bar{l}_y \propto \bar{l}_x^{\alpha_y/\alpha_x} , \quad \bar{l}_{yw} \propto \bar{l}_x^{\alpha_{yw}/\alpha_x} , \qquad (31)$$

where $\alpha_y/\alpha_x = 0.66$ and $\alpha_{yw}/\alpha_x = 0.55$ for the depinning and pinning regime respectively. It was suggested in [18] and in [36] that α_y/α_x could be another measure of the roughness of the self-affine fracture front, in agreement with previous experimental measurements of the roughness exponent. However, in a very recent experimental work [7] on planar crack growth, there has been two roughness exponents observed acting at different scales; a smallscale roughness with exponent ~ 0.6 and a largescale roughness with exponent ~ 0.4, with a crossover depending on the fracture toughness fluctuations and the stress intensity factor. This trend has also
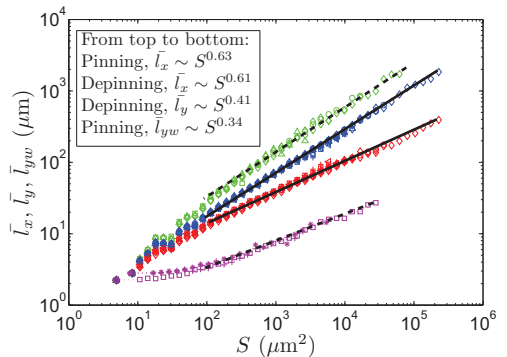

FIG. 15: Linear extent of pinning and depinning clusters as a function of cluster size for the full span of threshold levels and averaged over all experimental conditions. The slopes of the different fitted lines (dashed - pinning clusters, solid - depinning clusters) are indicated in the caption. Note that there in all cases are initial transients up to $S \approx 100 \mu m^2$.

been seen for the aspect ratio of depinning clusters in the simulation study by Laurson et al. [33]. In the experimental case on the other hand, considering that the length scale of this roughness crossover are comparable with the $\bar{l}_x$ range in our case, we find no traces of such behaviour in the aspect ratio of depinning clusters. This point thus warrants further consideration.

Finally, we discuss the marginal distributions of the extension lengths, i.e. for all cluster sizes, in the two regimes denoted $P(l_x)$, $P(l_y)$, and $P(l_{yw})$. For clarity we mention again that l_x scales similarly with S in the two regimes only separated by a small difference in the proportionality factor, whereas l_y describing the depinning regime, and l_{yw} describing the pinning regime, are treated separately. The insets in Fig. 16(a)(b) show the extension length distributions $P(l_x)$ and $P(l_y)$ respectively in the pinning regime. The corresponding pinning cluster distributions display similar behaviour, except that the $P(l_{yw})$ distribution is entirely dominated by a cutoff function. This is due to the very narrow $y-$direction span of pinning clusters. We define the following distributions for the extension lengths

$$P(l_x) \propto l_x^{-\beta_x} D(l_x/l_x^*) \qquad (32)$$

$$P(l_y) \propto l_y^{-\beta_y} D(l_y/l_y^*) \qquad (33)$$

$$P(l_{yw}) \propto l_{yw}^{-\beta_{yw}} D(l_y/l_y^*) , \qquad (34)$$

where $D(x)$ is some cutoff function decaying faster to zero than any power of l_x, l_y or l_{yw} when $x > 1$ and constant otherwise. The β exponents above can be predicted from our previous results for the cluster size distribution. From statistics we know that the relation between the PDFs of two random variables b and c, one-to-one
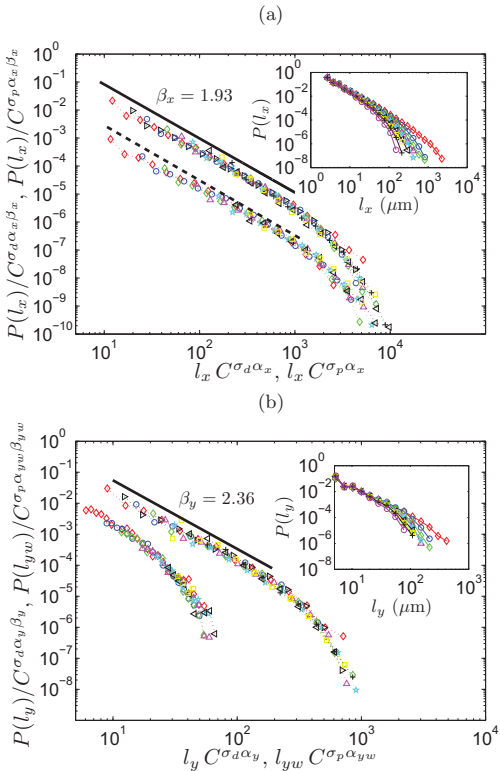
FIG. 16: **(a)** Collapsed $P(l_x)$ distributions averaged over all different experimental conditions for both depinning (upper set of data) and pinning (lower set of data). The pinning distributions have been shifted for visual clarity. Depinning and pinning thresholds are in the range $C = 2 - 30$ and $C = 2 - 12$ respectively. The solid and dashed lines both have the slope $\beta_x = 1.93$. Inset shows for the case of depinning the threshold dependence for the unscaled distributions. **(b)** Collapsed $P(l_y)$ and $P(l_{yw})$ distributions averaged over all different experimental conditions for the depinning (upper set of data) and pinning (lower set of data) regime respectively. The pinning distributions have been shifted for visual clarity. Thresholds are in the range $C = 2 - 30$ and $C = 2 - 12$ for depinning and pinning respectively. The solid line has the slope $\beta_y = 2.36$. Inset shows for the case of depinning the threshold dependence for the unscaled distributions.

related, can be expressed as

$$P(b) = P(c)\frac{dc}{db} \ . \tag{35}$$

In our case S, l_x, l_y, and l_{yw} is not one-to-one related, but since the means $\bar{l}_x$, $\bar{l}_y$ and $\bar{l}_{yw}$ have only small standard deviations, the PDFs $P(l_x)$, $P(l_y)$, $P(l_{yw})$ should at least be approximated by Eq. (35). For $P(l_x)$ we get

by inserting Eq. (14) and Eq. (30) into Eq. (35)

$$\beta_x = \frac{\gamma + \alpha_x - 1}{\alpha_x} \ , \tag{36}$$

where $\beta_x = 1.93$. Similarly we obtain $\beta_y = 2.36$ and $\beta_{yw} = 2.65$. For the depinning regime we obtain for the cutoffs in Eqs. (32) and (33) by using Eqs. (15) and (30):

$$l_x^* \propto C^{-\sigma_d \alpha_x} \ , \qquad l_y^* \propto C^{-\sigma_d \alpha_y} \ . \tag{37}$$

For the pinning regime we obtain for the cutoffs in Eqs. (32) and (34) by using Eqs. (16) and (30):

$$l_x^* \propto C^{-\sigma_p \alpha_x} \ , \qquad l_{yw}^* \propto C^{-\sigma_p \alpha_{yw}} \ . \tag{38}$$

The extension length distributions in both velocity regimes are collapsed according to Eqs. (32-34) as shown in Fig. 16(a)(b). In the $x-$direction, transverse to the direction of crack propagation, the distribution in both regimes scale with the same exponent, similarly to what was found for the cluster size distribution. The only difference between the two distributions is the proportionality factor in the cutoff length, as explained earlier. We see that along the direction of crack propagation the depinning $[P(l_y)]$ and pinning $[P(l_{yw})]$ distribution are quite different, in the sense that all power law behaviour is suppressed by the cutoff function in the latter distribution. This is understandable since the span of l_{yw} values is no more than one decade.

In Sec. III B we discussed various correlation functions of the spatio-temporal velocity field. In particular it was seen that the local velocities had correlation lengths of the order $\sim 100\,\mu m$ and $10\,\mu m$ in the $x-$ and $y-$direction respectively. One would expect the correlation lengths in some sense to control the extent of pinning and depinning clusters. This dependence is non trivial since a cluster in this context is artificially constructed by thresholding the velocity field. No clear relation is found between the cutoff size of the pinning and depinning clusters, and the correlation length extracted from the autocorrelation function of the velocity field. However, since the clusters are obtained from thresholded velocities, it is also possible to look at the autocorrelation function of thresholded velocities, rather than the one of the continuous velocity signal. In ongoing work we consider such correlation functions $G_C(\Delta x)$ [Eq. (4)], obtained from discretized signals $v_C(x,t)$ where the local velocities along each front line are now thresholded with a threshold C according to Eq. (12). Preliminary analysis indicate the existence of a correlation length roughly proportional to l_x^* [Eq. (37)], meaning that both quantities evolve similarly with the threshold C.

Furthermore, in the $x-$direction we could see clear sample differences in the correlation lengths, even though they were within the same order of magnitude (Fig. 6). Analysing carefully both size and extension length distributions of individual experiments, and not average distributions as presented above, we could not recognize such trends. In this respect it is also important to mention

that for individual experiments, the cutoff behaviour in the distributions are not well pronounced due to the lack of large scale statistics. Even when considering the above limitations, we can say that the geometry of pinning lines are qualitatively consistent with the observed correlation lengths. Thus it seems that the vanishingly small correlation length in the $y-$direction, describes the low value part of the local velocity distribution.

IV. CONCLUSION

The local dynamics of an in-plane mode-I fracture have been studied experimentally using high resolution monitoring of the front line advances. Indeed the transparency of the PMMA enable us to follow the fracture process using a high-speed camera. Fracture is induced by fixing the upper plate, while applying a force on the lower plate from a press bar controlled by a step motor. Experiments are performed using two sets of boundary conditions: 1) constant driving velocity on the pressbar, giving a linear deflection in time between the plates (CVBC) and 2) fixed deflection between the plates (CBC), resulting in a slow creep motion of the fracture front.

Disorder is introduced in the fracture plane by a sandblasting and sintering procedure, resulting in heterogeneous fluctuations of the local toughness. The competition between the toughness fluctuations and the long range damping elastic forces results in a rough fracture front with self affine scaling properties. In this study we have considered the local dynamics of the fracture front over a wide range of average propagation velocities $(0.028 < \langle v \rangle < 141)\mu$m/s. The local velocity field is obtained through the waiting time matrix and gives a spatio-temporal distribution with a large power law tail for high velocities described by an exponent $-\eta = -2.55$. The fracture front advance, displays pinning and avalanches with a broad range of velocity scales. Our results show that the local dynamics is similar in every respect for the two different boundary conditions. This is an important and non-trivial result considering the very different behaviour in the global large scale propagation. Additionally, no dependence on the average propagation velocity for different experiments is found.

The average autocorrelation of local velocities have been studied in both spatial directions, and also in time along the direction of crack propagation. We find that the velocities are correlated up to $\sim 100\,\mu$m transverse to the direction of crack propagation, and $\sim 10\,\mu$m, i.e. close to the spatial resolution, and thus uncorrelated in the direction of crack propagation. Within these general trends we have seen that there are differences in the autocorrelation function from sample to sample, but no dependence on the loading condition or average propagation velocity. Relating the autocorrelation of velocities in time to the evolution of the front width gives a growth exponent of $\alpha = 1/2$ similar to simple diffusion, a process such as Brownian motion.

The local dynamics have been studied through a statistical analysis of local avalanche events. We have observed that the cluster properties are independent of both loading conditions and average velocity of the crack front. The depinning cluster size distribution show scale invariance, described by an exponent $-\gamma = -1.56$, in agreement with previous experimental [18] and numerical results [32, 33]. Surprisingly the same result is found also for the pinning regime. Furthermore, we have in this study seen that the cluster size distribution scaling is truncated by an upper cutoff, depending on the threshold value. We have shown that the cutoff essentially is controlled by the total distribution of local velocities. Particularly for the depinning regime we have obtained a scaling law relating the cluster size exponent γ to the exponent η describing the local velocity distribution.

Clusters have in both velocity regimes been further decomposed into extension lengths in the $x-$ and $y-$direction. We have demonstrated that the distributions of these extension lengths are consistent with their size distribution. The aspect ratio of depinning clusters follows a power law with the exponent $\alpha_y/\alpha_x = 0.66$ indicating that the clusters are anisotropic and extending longer transverse to the direction of propagation than in the direction of crack propagation. We have yet to obtain experimentally a relationship between the extension of depinning clusters and the roughness of the fracture front. This is a topic that warrants further work.

The pinning clusters were found to display a very strong anisotropy, extending far in the $x-$direction as opposed to the very short $y-$direction extension. This is qualitatively in agreement with the found velocity correlation lengths in the two directions, thus indicating that these lengths describe the spatial correlations of low velocities.

APPENDIX A: THE WAITING TIME MATRIX

The waiting time matrix (WTM) is a robust procedure that enables a comparison of both different experiments at different time and space resolution, and also with numerical simulations of similar systems. It can be applied to any propagating interface [30–32], and is particularly suited for estimating the local velocity of pinned interfaces which are dominated by low speeds. Below, we will explain the procedure in detail.

The coordinates of the extracted front lines $h(x, t)$, introduced in Fig. 3, can be represented in matrix form as: $H(x, h(x, t)) = 1$ and 0 elsewhere, with a matrix size equal to the captured image size. We define the WTM W as the sum of all front matrices H,

$$W(x, y) = \sum_t H(x, h(x, t)) \, , \qquad (A1)$$

where the sum runs over all discrete times t. Note that W is an integer matrix, so to get the true waiting time, the time step δt must be multiplied to each matrix element

w. An example of front line addition is shown in Fig. 17.

$$
t_1 \begin{bmatrix}
0 & 0 & 0 & 0 & 0 & 0 & 0 & 0 & 0 & 0 & 0 & 0 & 0 \\
1 & 0 & 0 & 0 & 0 & 0 & 0 & 1 & 0 & 0 & 0 & 0 & 1 \\
0 & 1 & 0 & 0 & 1 & 0 & 1 & 0 & 1 & 0 & 0 & 1 & 0 \\
0 & 0 & 1 & 1 & 0 & 1 & 0 & 0 & 0 & 1 & 1 & 0 & 0 \\
0 & 0 & 0 & 0 & 0 & 0 & 0 & 0 & 0 & 0 & 0 & 0 & 0 \\
0 & 0 & 0 & 0 & 0 & 0 & 0 & 0 & 0 & 0 & 0 & 0 & 0
\end{bmatrix}
$$

$$
t_2 \begin{bmatrix}
0 & 0 & 0 & 0 & 0 & 0 & 0 & 0 & 0 & 0 & 0 & 0 & 0 \\
2 & 0 & 0 & 0 & 0 & 0 & 0 & 1 & 0 & 0 & 0 & 0 & 1 \\
0 & 2 & 0 & 0 & 1 & 0 & 1 & 1 & 2 & 0 & 0 & 2 & 1 \\
0 & 0 & 2 & 2 & 1 & 1 & 1 & 0 & 0 & 2 & 2 & 0 & 0 \\
0 & 0 & 0 & 0 & 0 & 1 & 0 & 0 & 0 & 0 & 0 & 0 & 0 \\
0 & 0 & 0 & 0 & 0 & 0 & 0 & 0 & 0 & 0 & 0 & 0 & 0
\end{bmatrix}
$$

$$
t_3 \begin{bmatrix}
0 & 0 & 0 & 0 & 0 & 0 & 0 & 0 & 0 & 0 & 0 & 0 & 0 \\
2 & 0 & 0 & 0 & 0 & 0 & 0 & 1 & 0 & 0 & 0 & 0 & 1 \\
1 & 2 & 0 & 0 & 1 & 0 & 1 & 1 & 2 & 0 & 0 & 3 & 2 \\
0 & 1 & 3 & 3 & 1 & 1 & 2 & 1 & 1 & 2 & 3 & 0 & 0 \\
0 & 0 & 0 & 0 & 1 & 2 & 0 & 0 & 0 & 1 & 0 & 0 & 0 \\
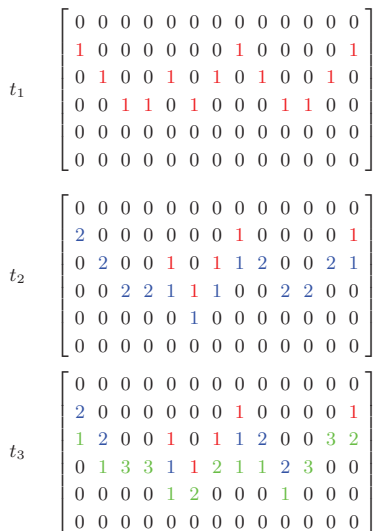0 & 0 & 0 & 0 & 0 & 0 & 0 & 0 & 0 & 0 & 0 & 0 & 0
\end{bmatrix}
$$

FIG. 17: Example of the computation of the waiting time matrix $W(x,y)$ [Eq. (A1)]. All fronts are added to an originally empty matrix in time step unit. Indicated above is the addition of front lines in three timesteps t_1 (red), t_2 (blue), and t_3 (green).

From above it is clear that the WTM procedure gives a *spatial* map that accounts for the amount of time spent by the front at a given pixel, thus reflecting the local dynamics of the interface. However, avoiding holes in the WTM, implies a high enough sampling rate, so that the movement of the front position is at maximum one pixel between two subsequent images. Second, it also requires a small noise from the imaging device. Finally, care must be taken in preparing the sample. Indeed, impurities and surface scratches are not transparent but rather reflect light and may thus artificially alter the extracted front shape. In our case, experiments are devised so that the front is propagating in a steady manner both before and after the short interval of image capture. To avoid transient effects at the beginning and at the end of the image recording, we typically clip between 200-500 front lines in the start and end of the generated WTM.

From the WTM we can construct the local velocity matrix in *space* $V(x,y)$. Matrix elements represent the normal speed of the fracture front at the time it went through a particular position

$$
v = \frac{1}{w}\frac{a}{\delta t} . \tag{A2}
$$

From the local velocity matrix $V(x,y)$, we can also obtain the local velocity along each front $h(x,t)$

$$
v(x,t) = V(x, h(x,t)) . \tag{A3}
$$

By computing $v(x,t)$ for every time step, we build the *spatio-temporal* velocity map $V_t(x,t)$. We then define the average propagation velocity of the front $\langle v \rangle$ as the average taken over all elements in the matrix $V_t(x,t)$. The development of the front in time for a given $x-$position is shown in Fig. 18 (a), also indicating how the velocity is approximated from the WTM. One realization of the local velocity fluctuations along a front line is shown in Fig. 18 (b).
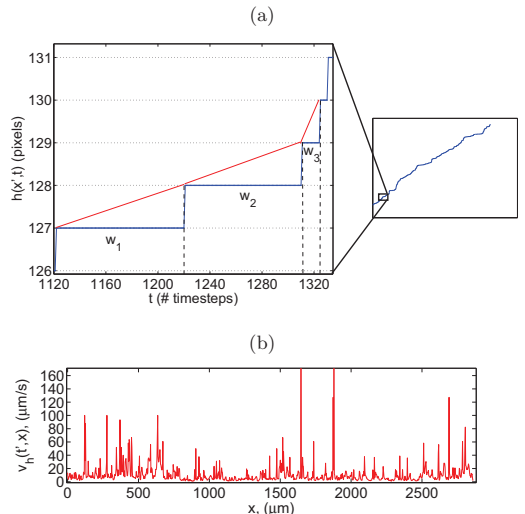

FIG. 18: **(a)** Pixel level zoom in of a frontline $h(x',t)$ at a given position x' as function of time. Indicated are three waiting times w_1, w_2 and w_3 separated by a one-pixel jump. As an example, note that all captured fronts from $h(x',t_0)$ to $h(x',t_0+w_1)$ is given the same constant velocity $v_1 \propto 1/w_1$ in making the jump from pixel 127 to pixel 128 along the $y-$axis. This approximation means that the front position increases linearly during this time interval (indicated in red). **(b)** Local velocity fluctuations $v(x,t')$ along the frontline $h(x,t')$.

APPENDIX B: VELOCITY PDF TRANSFORMATION

In transforming from the spatio-temporal map $V_t(x,t)$ [Eq. (A3) and Fig. 18 b)] to the spatial map $V(x,y)$ [Eqs. (A1) and (A2)] with the PDFs $P(v)$ and $R(v)$ respectively, we can express the space travelled through at speed v over a time dt as $dy = v\, dt$. The area in (x,y) space where the front travels at speed u between v and $v+dv$ corresponds to the total area of fracture propagation, $A_{x,y}$, multiplied by the fraction of the area

corresponding to this speed:

$$\int_{v<u(x,y)<v+dv} dxdy = A_{x,y}R(v)dv \ . \qquad (B1)$$

This area is related to the area covered by the fronts traveling at that speed in the spatio-temporal map, expressed using the variable change between y and t:

$$\int_{v<u(x,y)<v+dv} dxdy = \int_{v<u(x,t)<v+dv} dxvdt \qquad (B2)$$

Eventually, this last area is directly related to the distribution $P(v)$, with the same argument as for the spatial map: denoting $A_{x,t}$ the total area of the spatio temporal map, we can write

$$\int_{v<u(x,t)<v+dv} dxdt = A_{x,t}P(v)dv \qquad (B3)$$

Inserting Eqs. (B1) and (B3) into Eq. (B2) leads to

$$A_{x,y}R(v)dv = A_{x,t}P(v)vdv \ . \qquad (B4)$$

Furthermore it can be shown that $A_{x,y}/A_{x,t} = \langle v \rangle$, thus eventually

$$v\, P(v)\, dv = \langle v \rangle R(v)\, dv \ . \qquad (B5)$$

ACKNOWLEDGMENTS

[1] B. Lawn, *Fracture of Brittle Solids* (Cambridge University Press, Cambridge, England, 1993).
[2] M. J. Alava, P. K. V. V. Nukala, and S. Zapperi, Adv. Phys. **55**, 349 (2006).
[3] D. Bonamy, J. Phys. D: Appl. Phys. **42**, 214014 (2009).
[4] E. Bouchaud, J. Phys. Condens. Matter **9**, 4319 (1997).
[5] J. Schmittbuhl, and K. J. Måløy, Phys. Rev. Lett **78**, 3888 (1996).
[6] A. Delaplace, J. Schmittbuhl, and K. J. Måløy, Phys. Rev. E **60**, 1337 (1999).
[7] S. Santucci, M. Grob, A. Hansen, R. Toussaint, J. Schmittbuhl, and K. J.Måløy, cond-mat, arXiv:1007.1188 (2010).
[8] L. Ponson, D. Bonamy, and E. Bouchaud, Phys. Rev. Lett. **96**, 035506 (2006).
[9] D. Bonamy, L. Ponson, S. Prades, E. Bouchaud, and C. Guillot, Phys. Rev. Lett. **97**, 135504 (2006).
[10] S. Santucci, K. J. Måløy, A. Delaplace, J. Mathiesen, A. Hansen, J. O. Haavig Bakke, J. Schmittbuhl, L. Vanel, and P. Ray, Phys. Rev. E **75**, 016104 (2007).
[11] J. Schmittbuhl, A. Hansen, and G. G. Batrouni, Phys. Rev. Lett. **90**, 045505 (2003).
[12] J. P. Bouchaud, E. Bouchaud, G. Lapasset, and J. Planes, Phys. Rev. Lett **71**, 2240 (1993).
[13] J. Schmittbuhl, S. Roux, J. P. Vilotte, and K. J. Måløy, Phys. Rev. Lett **74**, 1787 (1995).
[14] A. Hansen and J. Schmittbuhl, Phys. Rev. Lett. **90**, 045504 (2003).
[15] A. L. Barabasi, and H. E. Stanley, *Fractal Concepts in Surface Growth* (Cambridge University Press, New York, 1995).
[16] J. Sethna, K. Dahmen, and C. Myers, Nature (London) **410**, 242 (2001).
[17] K. J. Måløy, and J. Schmittbuhl, Phys. Rev. Lett **87**, 105502 (2001).
[18] K. J. Måløy, S. Santucci, J. Schmittbuhl, and R. Toussaint, Phys. Rev. Lett. **96**, 045501 (2006).
[19] S. Santucci, L. Vanel, and S. Ciliberto, Phys. Rev. Lett. **93**, 095505 (2004).
[20] A. Marchenko, D. Fichou, D. Bonamy, and E. Bouchaud, Appl. Phys. Lett. **89**, 093124 (2006).
[21] B. Gutenberg and C. F. Richter, *Seismicity of Earth and Associated Phenomena* (Princeton University Press, Princeton, NJ, 1954).
[22] A. Corral, Phys. Rev. Lett. **92**, 108501 (2004).
[23] A. P. Mehta, K. A. Dahmen, and Y. Ben-Zion, Phys. Rev. E **73**, 056104 (2006).
[24] A. Garcimartín, A. Guarino, L. Bellon, and S. Ciliberto, Phys. Rev. Lett. **79**, 3202 (1997).
[25] J. Davidsen, S. Stanchits, and G. Dresen, Phys. Rev. Lett. **98**, 125502 (2007).
[26] J. Koivisto, J. Rosti, and M. J. Alava, Phys. Rev. Lett. **99**, 145504 (2007).
[27] D. Spasojevi, S. Bukvić, S. Milošević, and H. E. Stanley, Phys. Rev. E **54**, 2531 (1996).
[28] A. Prevost, E. Rolley, and C. Guthmann, Phys. Rev. B **65**, 064517 (2002).
[29] S. Moulinet, A. Rosso, W. Krauth, and E. Rolley, Phys. Rev. E **69**, 035103 (2004).
[30] R. Planet, S. Santucci, and J. Ortín, Phys. Rev. Lett. **102**, 094502 (2009).
[31] M. Grob, J. Schmittbuhl, R. Toussaint, L. Rivera, S. Santucci, and K. J. Måløy, Pure Appl. Geophys. **166**, 777 (2009).
[32] D. Bonamy, S. Santucci, and L. Ponson, Phys. Rev. Lett **101**, 045501 (2008).
[33] L. Laurson, S. Santucci, and S. Zapperi, Phys. Rev. E **81**, 046116 (2010).
[34] J. W. Obreimoff, Proc. Roy. Soc. London A **127**, 290 (1930).
[35] S. Santucci, K. J. Måløy, R. Toussaint, and J. Schmittbuhl, *Interconnected Biosensor Systems: Networks and Bioprocesses* (Kluwer, Amsterdam, 2006).
[36] K. J. Måløy, R. Toussaint, and J. Schmittbuhl, *Dynamics and Structure of Interfacial Crack Fronts* (Proc. of the ICF11, 11th International Conference on Fracture, Torino, 2005).